

Tuning Hybrid Optomechanics for Remote Entanglement

Thesis by
Utku Hatipoğlu

In Partial Fulfillment of the Requirements for the
Degree of
Doctor of Philosophy

The logo for the California Institute of Technology (Caltech), featuring the word "Caltech" in a bold, orange, sans-serif font.

CALIFORNIA INSTITUTE OF TECHNOLOGY
Pasadena, California

2025
Defended May 28, 2025

© 2025

Utku Hatipođlu
ORCID: 0000-0002-0511-9196

All rights reserved

*Hayat kısa,
kuşlar uçuyor.*
Cemal Süreya

ACKNOWLEDGEMENTS

This thesis wouldn't be possible without the guidance, collaboration, technical and moral support, love and friendship of certain people.

I would like to thank Oskar, for giving me the opportunity to work in this incredible environment, introducing me to the field of quantum optomechanics and his support throughout. A special thank you goes to Sameer, with whom I have been working side by side since day one. I am happy that we were in the long lived states (*Rick ± Morty*)/ $\sqrt{2}$. Piero, David and Srujan, it was great working and hanging with you during the last years. Bastien, Ricky and John, you cool cats! In the lab and out on the football field (also with the captain, Olivia), it was so much fun. Andreas and Gihwan, I wish I had more lunches with you guys. Other lab members and friends, Matt Matheny, Matt Davidson, Jamison, Jared, Vinicius, Steven, Jash, Mo, Sherry, Eunjong, Mohammad, Mahmoud and all earlier members who contributed to the lab, thank you. I want to especially thank Alp Sipahigil, whose support helped me to be a part of the Painter Lab. I want to extend my gratitude to my master's PI, Selim Hanay and Michael Roukes, with whom I worked for a brief period during my master's, for their guidance and support which was essential in my PhD journey. I am grateful to Kerry Vahala, Alireza Marandi and Austin Minnich for serving on my PhD candidacy and defense committees.

QPG staff, Barry, McCoy, Chris, Trevor, Brandon, thank you for your hard work which makes it all possible. KNI staff, thanks for keeping the cleanroom up and running, which was crucial for my work. Bert, wish you were here. Our admins, Angie, Christy, Jennifer and Tiffany, thank you all. Also, very special thanks to Laura from ISP!

Old friends back in Turkey and all over the world. Esteemed members of The Bro Club; Efe, Cem, Egehan, Alper. Motorheads; Yiğit, Cem, Ilmo, Mert, Dundar. Kanki, Berkin, Onur and many more...

I made many new friends and became very close with some old ones here in California, from all over the world, and they made this a real journey. Mert, Hirsh, Scotty, Taylan, Atakan, Sahangi, Alessio, Connor, Dulce, Nicole, Sari, Arda, Cenk, Batu, Pink Alex, Ewa, Alkim, Su, Bilge, Yannis, Isa, Alex (the poet), Pantelis, Haroula, Andrea, Lucía, Elina, Olmo, Edo, Attilio, Tanner, Firat, Aki, Samson, Tristan, Chloé, Vincent, Fedé, Alexis, Elodie, Mattia, Elvira, Arielle, Rishav, Théo,

Solène, Niyati, Saif, Prachi, Shruti, Yanky, Alessandro, Komron, Volkan, Tommaso, AJ, Brandon, Ethan, Emile, Marek, Chris and many more... Finally, Solène, your existence in my life meant a lot, thank you for everything.

I have a big family and being away from them was a challenge all together. However, even though they were 11000 km away, I always felt their support and love in my hearth. I am deeply grateful to my mom, dad and sister the most, for their unconditional love and support since '95. Her şey için teşekkür ederim. Siz olmasaydınız, ben ben olamazdım.

ABSTRACT

Superconducting microwave circuits are a leading platform for quantum computing, offering high coherence and controllability. However, their reliance on microwave photons, which are highly susceptible to thermal noise at room temperature due to their relatively low frequencies, necessitates operation at millikelvin temperatures. This requirement presents a major scalability challenge, particularly for connecting distant processors within a distributed quantum network. Microwave-optical transducers offer a promising solution by enabling coherent links between the microwave and optical domains, allowing quantum information to be shared via telecom-wavelength photons that propagate efficiently through low-loss optical fibers at room temperature. Among the various transduction platforms, hybrid piezo-optomechanical crystals (OMCs) are particularly promising due to their strong optomechanical and piezoelectric coupling and the potential for high-efficiency, low-noise transduction mediated by microwave frequency phonons. Proposed architectures for remote entanglement distribution rely on the interference of indistinguishable photons emitted from individual transducers. Although state-of-the-art fabrication techniques provide nanometer-level precision, achieving identical OMCs remains challenging, leading to device-to-device variations in optical and mechanical resonance frequencies. To enable scalable quantum networks based on optically mediated remote entanglement, a robust, selective, and precise post-fabrication tuning method is essential.

Here, we present an in situ, selective technique for tuning the optical and acoustic resonances of hybrid silicon optomechanical crystals through electric field-induced nano-oxidation using an atomic force microscope (AFM). The localized growth of a few-nanometer-thick silicon dioxide layer modifies the local permittivity, stiffness, and mass of the OMC at the oxidation region, consequently altering the optical and mechanical modes supported by the structure. Using this method, we demonstrate precise and targeted spectral alignment of both optical and mechanical modes across multiple devices within their respective mode linewidths. In addition, we extend this technique to achieve selective room-temperature pre-alignment of the optical mode of OMCs for precise wavelength alignment at millikelvin temperatures. This capability is essential for realizing indistinguishable photon emission from independently fabricated transducers toward entanglement of distant quantum processors in optically linked quantum networks.

In the second part of this thesis, we present a side-coupled two-dimensional optomechanical cavity designed for high-efficiency, low-noise phonon–photon transduction. This architecture enables near-unity conversion efficiency between optical photons and microwave frequency phonons while maintaining thermal occupancy of the phonon mode well below unity, an essential requirement for quantum-enabled operations. Finally, we describe the design, fabrication, and preliminary characterization of a microwave-to-optical transducer based on this new side-coupled 2D OMC platform.

PUBLISHED CONTENT

[1] Utku Hatipoglu*, Sameer Sonar*, David P. Lake, Srujan Meesala, and Oskar Painter. In situ tuning of optomechanical crystals with nano-oxidation. *Optica*, 11(3): 371–375, 2024.

DOI:<https://doi.org/10.1364/OPTICA.516479>

U.H. participated in the conception of the project, designed and fabricated the devices, developed methods, and performed the measurements.

[2] Sameer Sonar*, Utku Hatipoglu*, Srujan Meesala, David P. Lake, Hengjiang Ren, and Oskar Painter. High-efficiency low-noise optomechanical crystal phonon transducers. *Optica*, 12(1): 99–104, 2025.

DOI:<https://doi.org/10.1364/OPTICA.538557>

U.H. participated in the conception of the project, designed and fabricated the devices, developed methods, and performed the measurements.

TABLE OF CONTENTS

Acknowledgements	iv
Abstract	vi
Table of Contents	viii
List of Illustrations	xi
List of Tables	xiii
Chapter I: Cavity optomechanics and optomechanical crystals	1
1.1 Cavity optomechanics	1
1.2 Sideband resolved optomechanics	5
1.3 Hybrid optomechanics	7
1.4 Optomechanical crystals	9
1D Optomechanical crystals	11
Phononic shielding	14
I Tuning Hybrid Optomechanical Crystals	17
Chapter II: In situ tuning of OMCs with AFM nano-oxidation	21
2.1 Nanofabrication induced imperfections	21
2.2 AFM nano-oxidation fundamentals	25
Atomic Force Microscopy	25
2.3 Conductive AFM (cAFM) and AFM nano-oxidation	28
2.4 Nano-oxidation of silicon	29
2.5 Nano-oxidation on OMCs	32
Proposed OMC tuning method with nano-oxidation	32
Pixel-by-pixel oxidation simulations	34
2.6 In situ nano-oxidation setup	38
2.7 Experimental characterization of nano-oxidation induced mode shifts	39
2.8 Effect of nano-oxidation on the intrinsic optical scattering rate	44
2.9 Pattern generation algorithm based on empirical shift data	45
2.10 Fine tuning methods	49
2.11 Simultaneous optical and acoustic mode tuning of OMCs	51
Coarse tuning of OMCs using pattern generation algorithm	52
Real-time fine-tuning of OMCs with pixel-by-pixel oxidation	54
2.12 Conclusion	56
Chapter III: Tuning OMCs for cryogenic operations	58
3.1 Modified AFM nano-oxidation setup	58
3.2 Contact mode AFM nano-oxidation for optical mode tuning	59
3.3 Wavelength change due to native oxidation in room temperature	62
3.4 Temperature dependent wavelength shifts of OMCs at 10mK	63
3.5 Tuning protocol for cryogenic wavelength alignment	68

3.6	Tuning multiple OMCs for wavelength alignment at 10mK	70
3.7	Discussion	72
Chapter IV: Other avenues using biased tip AFM		74
4.1	Post-fabrication band tuning with nano-oxidation	74
4.2	Quality enhancement with selective oxidation	75
4.3	AFM poling of lithium niobate	75
 II Next-Generation Hybrid Optomechanical Crystal Microwave-Optical Transducers		79
Chapter V: High efficiency low noise phonon-photon transducers		81
5.1	Side coupled 2D optomechanical crystal	81
5.2	Measurement setup	83
5.3	Optical absorption-induced hot bath	85
5.4	Continuous wave phonon-photon transduction	89
5.5	Pulsed phonon-photon transduction	92
5.6	Discussion	94
Chapter VI: Hybrid 2D OMCs for microwave-optical transduction		99
6.1	Design of the hybrid 2D OMC transducer	99
6.2	Fabrication of the hybrid 2D OMC transducer	106
6.3	Measurement setup	111
6.4	Room temperature characterization	112
6.5	Preliminary cryogenic characterizations	114
6.6	Outlook	115
Bibliography		118
Appendix A: Nanofabrication		127
A.1	Nanofabrication tools	127
A.2	Hybrid 2D transducer fabrication	127
	Marker deposition	127
	AlN piezo box	128
	Silicon protection	129
	NbN resonators and electrodes	129
	Silicon layer	130
	Deep etching	131
A.3	1D and 2D OMC fabrication	132
Appendix B: Measurement techniques for hybrid OMCs		133
B.1	Mode occupancy calibration	133
B.2	Filter correction	134

LIST OF ILLUSTRATIONS

<i>Number</i>	<i>Page</i>
1.1 Fabry-Pérot cavity with a moving mirror	1
1.2 Sideband resolved optomechanics	6
1.3 Hybrid optomechanical systems	8
1.4 Light confinement within a nanobeam	12
1.5 1D OMC	13
1.6 Remote entanglement with hybrid optomechanical systems	19
2.1 Wavelength dispersion analysis with 200 imperfect OMCs	22
2.2 Typical optical and acoustic modes	23
2.3 Mode deviations from the unperturbed case for 200 imperfect OMC	24
2.4 Optical and acoustic modes for 20 fabricated OMC	24
2.5 Atomic Force Microscopy	26
2.6 Nano-oxidation mechanism	29
2.7 Contact mode oxidation characterization	30
2.8 Oxidation with tapping mode	31
2.9 Normalized optical and acoustic mode shapes of OMC	34
2.10 Pixel by pixel optical and acoustic mode shifts	36
2.11 Optical and acoustic selectivity map	37
2.12 AFM with integrated optical testing setup	39
2.13 Optics and acoustic focused patterns	40
2.14 In situ-nano-oxidation schematic	41
2.15 Optical and acoustic mode shifts with changing pattern dimensions	43
2.16 Change in intrinsic optical scattering rate	44
2.17 Shift matrices with mild optics targeting oxidation	46
2.18 Shift matrices with aggressive optics targeting oxidation	47
2.19 Optimal tuning pattern finding algorithm	48
2.20 Real-time, in situ monitoring of the oxidation process	50
2.21 3 Steps of coarse tuning	53
2.22 4 Steps of fine tuning	55
3.1 Contact mode oxidation isolated optics tuning pattern	60
3.2 Optical wavelength shift with respect to the tip bias voltage	61
3.3 Change in optical intrinsic quality factor	61

3.4	Wavelength drift due to native oxidation	63
3.5	Temperature versus coefficient of thermal expansion of silicon	64
3.6	Optical wavelength shift due to changing permittivity	66
3.7	Thermally induced optical wavelength shift	67
3.8	Tuning of 5 OMCs for alignment at 10mK	71
4.1	SEM image of the lithium niobate features patterned with AFM	76
5.1	Side-coupled 2D optomechanical crystal (OMC) cavity	81
5.2	Optical band diagram and modes of the side coupled 2D OMC	82
5.3	Experimental setup	84
5.4	Model and measurement scheme for optical absorption-induced hot bath	87
5.5	Characterization of optical absorption-induced hot bath	88
5.6	Phonon-to-photon transduction under continuous-wave excitation	90
5.7	n_c vs n_{th}	92
5.8	Phonon-to-photon transduction under pulsed laser excitation	93
5.9	Thermal occupation for various device parameters	94
6.1	Side-coupled 2D OMC with phonon waveguide	101
6.2	Piezoacoustic cavity with phononic shield	102
6.3	2D optical-microwave transducer	104
6.4	Tunable kinetic inductance resonator	105
6.5	AlN and marker deposition	107
6.6	AlN piezo-box fabrication	108
6.7	SEM of the AlN piezo-box	109
6.8	NbN layer fabrication	109
6.9	Silicon layer fabrication	110
6.10	SEM image of the 2D transducer	111
6.11	Experimental setup	112
6.12	Mechanical mode spectrum with a coherent microwave drive at 300K	113
6.13	Transduction under cryogenic conditions	115
A.1	Standard nanofabrication flow of 1D and 2D OMCs	132
B.1	Sideband filter chain transmission	134

LIST OF TABLES

<i>Number</i>	<i>Page</i>
5.1 Device parameters	83
5.2 Comparison of figures of merit for pulsed transduction	95
5.3 Comparison of figures of merit for continuous-wave transduction	95
A.1 Etch steps used in deep etching	131

Chapter 1

CAVITY OPTOMECHANICS AND OPTOMECHANICAL CRYSTALS

In this chapter, theoretical fundamentals of cavity optomechanics will be presented with a specific focus on light-matter interaction in the optomechanical crystals (OMC) and their basic design considerations. Higher level discussions on resonance tuning with specific material and geometric relations in Part I as well as the new design approaches explored for more complex systems in Part II will be constructed based on the fundamentals presented here. A more comprehensive analysis on the topic and details related to specific device design processes can be found in many pioneering work done in Painter Lab [1–6] and other papers [7, 8].

1.1 Cavity optomechanics

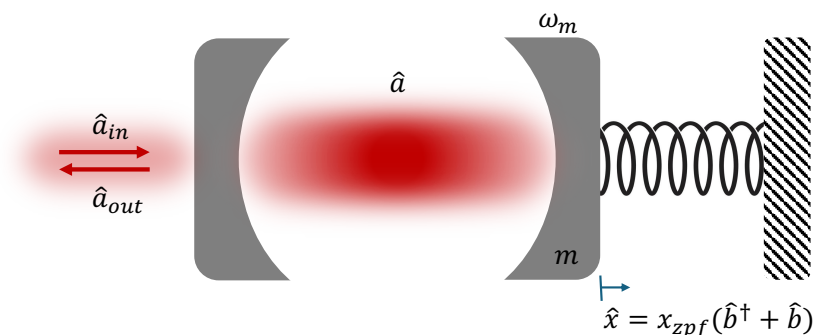


Figure 1.1: **Fabry-Pérot cavity with a moving mirror.** A canonical model for an optomechanical system where moving mirror modulates the light field in the cavity giving rise to optomechanical coupling.

Cavity optomechanics, in simple terms, is the study of engineered systems for enhanced light-matter interaction. A simple cavity optomechanical system can be modeled as a Fabry-Pérot cavity consisting of two mirrors, one of which is attached to a spring, forming a simple harmonic oscillator (see Figure 1.1). In such a setup, any movement of the ‘free’ mirror changes the cavity length hence modifies the light path. This is a rather generic model that applies to a wide range of systems from The Laser Interferometer Gravitational-Wave Observatory (LIGO) [9], with kg scale mirrors, to atomic scale trapped atom systems [10] and other systems [6, 11–15]

where electromagnetic field is modulated through mechanical perturbations. The optical resonance frequency of the generic Fabry-Pérot cavity is given by

$$\omega_c = \frac{n\pi c}{L_0}, \quad (1.1)$$

where c is the speed of light and L is the cavity length. If we incorporate the fact that any change in the free mirror position can slightly shorten or elongate the cavity length, we can replace the expression for cavity length with $L_0 + \hat{x}$ where \hat{x} is the free mirror position. Assuming $\hat{x} \ll L_0$, we can rewrite the free mirror position dependent optical resonance frequency using Taylor expansion.

$$\omega_c(\hat{x}) = \omega_c + \frac{\omega_c}{L_0} \hat{x}. \quad (1.2)$$

Using the derived optical resonance frequency, we can write the Hamiltonian that describes the entire optomechanical system with the photon annihilation (creation) operator $a(a^\dagger)$ and the phonon annihilation (creation) operator $b(b^\dagger)$.

$$\hat{H} = \hbar(\omega_{c,0} + \frac{\omega_{c,0}}{L_0} \hat{x}) \hat{a}^\dagger \hat{a} + \hbar\omega_m \hat{b}^\dagger \hat{b} \quad (1.3)$$

After writing \hat{x} in terms of phonon annihilation and creation operators and x_{zpf} , the zero-point fluctuation amplitude of the free mirror, and rearranging the equation, we get the following.

$$\hat{H} = \hbar\omega_c \hat{a}^\dagger \hat{a} + \hbar\omega_m \hat{b}^\dagger \hat{b} + \hbar(\frac{x_{zpf}\omega_{c,0}}{L_0}) \hat{a}^\dagger \hat{a} (\hat{b} + \hat{b}^\dagger) \quad (1.4)$$

Here, first and second terms are independent optical and mechanical resonator Hamiltonians, while the third term is the interaction Hamiltonian \hat{H}_{int} with the vacuum optomechanical coupling rate $g_0 = \frac{x_{zpf}\omega_{c,0}}{L_0}$. A final, cleaner form of the full optomechanical Hamiltonian with first-order optomechanical interaction term is given in Equation 1.5.

$$\hat{H} = \hbar\omega_c \hat{a}^\dagger \hat{a} + \hbar\omega_m \hat{b}^\dagger \hat{b} + \hbar g_0 \hat{a}^\dagger \hat{a} (\hat{b} + \hat{b}^\dagger) \quad (1.5)$$

So far, we assumed a ‘perfect’ model where the energy is preserved within the closed system however, various loss channels present in a real optomechanical

system. Intrinsic optical scattering rate κ_i and decay rate to the input optical field κ_e make up κ , the total optical loss rate, while γ_i represents the intrinsic mechanical damping rate. Including the loss parameters following the input-output formalism [16], our Hamiltonian becomes

$$\begin{aligned} \hat{H} = & \hbar\omega_c \hat{a}^\dagger \hat{a} + \hbar\omega_m \hat{b}^\dagger \hat{b} + \hbar g_0 \hat{a}^\dagger \hat{a} (\hat{b} + \hat{b}^\dagger) \\ & - \hbar \frac{\kappa}{2} i \hat{a}^\dagger \hat{a} - \hbar \frac{\gamma_i}{2} i \hat{b}^\dagger \hat{b} - \hbar \sqrt{\kappa_e} i (\hat{a}_{in} \hat{a}^\dagger + \hat{a}_{in}^\dagger \hat{a}) - \hbar \sqrt{\kappa_i} i (\hat{a}_i \hat{a}^\dagger + \hat{a}_i^\dagger \hat{a}) \\ & - \hbar \sqrt{\gamma_i} i (\hat{b}_{in} \hat{b}^\dagger + \hat{b}_{in}^\dagger \hat{b}). \end{aligned} \quad (1.6)$$

Operator \hat{b}_{in} is the acoustic mode noise operator which represents the coupling of the mechanical mode to its surrounding with the rate γ_i . While in thermal equilibrium with the mechanical bath, acoustic noise operator correlation relations can be written as follows.

$$\langle \hat{b}_{in}^\dagger(t) \hat{b}_{in}(t') \rangle = \frac{1}{e^{\hbar\omega_m/k_B T} - 1} \delta(t - t') \quad (1.7)$$

$$\langle \hat{b}_{in}(t) \hat{b}_{in}^\dagger(t') \rangle = \left(\frac{1}{e^{\hbar\omega_m/k_B T} - 1} + 1 \right) \delta(t - t') \quad (1.8)$$

Here the expression in front of the delta function represents the average thermal occupancy n_{th} (and $n_{th} + 1$) at a given bath temperature T .

Operators \hat{a}_{in} and \hat{a}_i represent the coupling of the optical mode to its surrounding where \hat{a}_{in} is the extrinsic noise operator and \hat{a}_i is the intrinsic noise operator. Extrinsic channel represents the coupling to the input optical light field with the rate κ_e while intrinsic channel is the coupling to all other environmental loss channels with the rate κ_i . At room temperature and below ($< 300K$), where the entirety of the work presented in this thesis is operated at, the bath can be approximated as vacuum, since $\hbar\omega_l \gg k_B T$.

Using the time evaluation of an operator in the Heisenberg picture that is given by $\dot{\hat{A}} = \frac{i}{\hbar} [\hat{H}, \hat{A}] + \frac{\partial \hat{A}}{\partial t}$, Heisenberg-Langevin equations of motion for our model can be derived from the full Hamiltonian with noise operators.

$$\dot{\hat{a}} = - \left(i\omega_c + \frac{\kappa}{2} \right) \hat{a} - ig_0 \hat{a} (\hat{b} + \hat{b}^\dagger) + \sqrt{\kappa_e} \hat{a}_{in} + \sqrt{\kappa_i} \hat{a}_i, \quad (1.9)$$

$$\dot{\hat{b}} = - \left(i\omega_m + \frac{\gamma_i}{2} \right) \hat{b} - ig_0 \hat{a}^\dagger \hat{a} + \sqrt{\gamma_i} \hat{b}_{in} \quad (1.10)$$

While intrinsic optical noise operator \hat{a}_i and the acoustic mode noise operator \hat{b}_{in} have only pure stochastic noise contributions, the extrinsic optical noise operator \hat{a}_{in} is composed of a stochastic part as well as a coherent tone at a specific frequency ω_l hence can be expanded as follows $(\alpha_{in} + \hat{a}_{in})e^{-i\omega_l t}$. If we reconstruct the equations of motion in a rotating frame with the laser frequency ω_l , the slower dynamics, namely mechanical mode, optomechanical coupling and losses can be captured more easily. This is a powerful technique since the optical frequency is multiple orders of magnitude higher than other rates contributing to the system dynamics. Here we also introduce the laser detuning $\Delta = \omega_c - \omega_l$ which is comparable to mechanical mode frequency ω_m in most cases.¹

$$\dot{\hat{a}} = -\left(i\Delta + \frac{\kappa}{2}\right)\hat{a} - ig_0\hat{a}(\hat{b} + \hat{b}^\dagger) + \sqrt{\kappa_e}(\alpha_{in} + \hat{a}_{in}) + \sqrt{\kappa_i}\hat{a}_i, \quad (1.11)$$

$$\dot{\hat{b}} = -\left(i\omega_m + \frac{\gamma_i}{2}\right)\hat{b} - ig_0\hat{a}^\dagger\hat{a} + \sqrt{\gamma_i}\hat{b}_{in} \quad (1.12)$$

An important metric that classifies the optomechanical system arises from the comparison of the optical loss rates and the optomechanical coupling rate. When $g_0 \gg \kappa_i$, where the optomechanical coupling is smaller than the optical loss rate, the optomechanical interactions can be linearized by neglecting the vacuum noise. Systems that satisfy these conditions are considered to be operating in the vacuum weak coupling regime, which is also where we operate for the devices presented in this work. Systems where the optomechanical coupling is comparable to or greater than the optical loss rate are considered to be operated in the vacuum strong coupling regime and they necessitate a nonlinear approach. Although, these systems are beyond the scope of this work.

To linearize the system with this assumption, we transform \hat{a} and \hat{b} similarly to what we performed on input noise \hat{a}_{in} earlier. Specifically, \hat{a} becomes $\hat{a} + \alpha$, whereas \hat{b} is denoted as $\hat{b} + \beta$. This transformation allows us to isolate the coherent steady state by solving the equations of motion for $\dot{\alpha} = 0$ and $\dot{\beta} = 0$.

Substituting the resulting steady-state amplitudes α and β into the Equations (1.11) and (1.12), and taking the Fourier transform of the resulting time-domain relations for \hat{a} and \hat{b} , we obtain expressions describing the cavity fluctuations of the system in the frequency domain. Here, $G = g_0\sqrt{n_c}$ represents the parametrically enhanced optomechanical coupling rate.

¹Detuning is chosen according to the desired optomechanical interaction. This will be discussed further in the coming sections.

$$\hat{a}(\omega) = \frac{-\sqrt{\kappa_e}\hat{a}_{\text{in}}(\omega) + \sqrt{\kappa_i}\hat{a}_i(\omega) - iG(\hat{b}(\omega) + \hat{b}^\dagger(\omega))}{i(\Delta - \omega) + \kappa/2} \quad (1.13)$$

$$\hat{b}(\omega) = \frac{\sqrt{\gamma_i}\hat{b}_{\text{in}}(\omega) - iG(\hat{a}(\omega) + \hat{a}^\dagger(\omega))}{i(\omega_m - \omega) + \kappa/2} \quad (1.14)$$

To obtain the relation for the mechanical fluctuations, explicitly in terms of the noise operators, we substitute the optical cavity fluctuation term $\hat{a}(\omega)$ into the Equation (1.14).

$$\hat{b}(\omega) = \frac{1}{i(\omega_m - \omega) + \gamma_i/2} \left(\sqrt{\gamma_i}\hat{b}_{\text{in}}(\omega) - iG \left[\frac{-iG(\hat{b}^\dagger(\omega) + \hat{b}(\omega)) + \sqrt{\kappa_e}\hat{a}_{\text{in}}(\omega) + \sqrt{\kappa_i}\hat{a}_i(\omega)}{i(\Delta - \omega) + \kappa/2} + \frac{iG(\hat{b}^\dagger(\omega) + \hat{b}(\omega)) + \sqrt{\kappa_e}\hat{a}_{\text{in}}^\dagger(-\omega) + \sqrt{\kappa_i}\hat{a}_i^\dagger(-\omega)}{-i(\Delta - \omega) + \kappa/2} \right] \right).$$

The new mechanical frequency can be expressed as $\omega_m + \delta\omega_m$ where $\delta\omega_m$ represents the mechanical fluctuations over the steady state. Mechanical loss rate can be denoted in two parts as $\gamma = \gamma_i + \gamma_{OM}$ where γ_{OM} represents the contribution of the optomechanical coupling that results in the optical damping of the mechanical resonator. Here are the expressions for the optical springing and damping terms.

$$\delta\omega_m = G^2 \text{Im} \left[\frac{1}{i(\Delta - \omega_m) + \kappa/2} - \frac{1}{-i(\Delta + \omega_m) + \kappa/2} \right] \quad (1.15)$$

$$\gamma_{OM} = 2G^2 \text{Re} \left[\frac{1}{i(\Delta - \omega_m) + \kappa/2} - \frac{1}{-i(\Delta + \omega_m) + \kappa/2} \right] \quad (1.16)$$

At $\Delta = \omega_m$, where the laser is detuned by a mechanical frequency from the cavity, optomechanical damping reaches its maximum value. This particular case will be discussed in detail in the next section.

1.2 Sideband resolved optomechanics

When an optomechanical system exhibits very high optical quality factors ($\sim 10^6$) and operates at high mechanical frequencies in the gigahertz range, such that $\omega_m \gg \kappa$, it enters the sideband resolved regime. The work presented in this thesis falls

within this regime, as our typical optical scattering rates are $\kappa < 1\text{GHz}$, while the mechanical resonance frequencies range from 5 to 10GHz depending on the device architecture. For the case where the laser detuning satisfies $\omega_c - \omega_l = \Delta = \omega_m$, optomechanical damping, which represents the scattering rate due to the optomechanical interaction becomes

$$\gamma_{OM} \approx \frac{4g_0^2 n_c}{\kappa}. \quad (1.17)$$

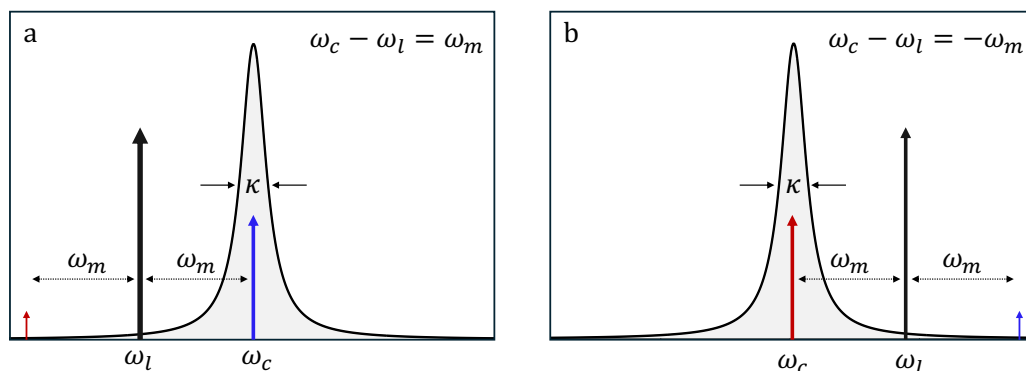


Figure 1.2: **Sideband resolved optomechanics.** A coherent drive tone (showed as black arrows) is scattered by the optomechanical interaction which creates Stokes and Anti-Stokes bands (red and blue arrows). In sideband resolved optomechanical systems ($\kappa \ll \omega_m$), **a**) Anti-Stokes sideband is amplified while the Stokes sideband is suppressed for a drive tone that is red detuned by a mechanical frequency ω_m . **b**) Stokes sideband is amplified while the Anti-Stokes sideband is suppressed for a drive tone that is blue detuned by a mechanical frequency ω_m .

When the cavity is driven with a laser tone parked on either red ($\Delta = \omega_m$) or blue ($\Delta = -\omega_m$) side, incident photons get scattered due to the optomechanical interaction. As a result of this scattering process, Stokes and Anti-Stokes side bands are generated. Although this is a symmetric process with respect to the laser tone, one sideband gets amplified whereas the other is suppressed based on the relative positioning with respect to the cavity. For the red detuned case, Stokes sideband lies far away from the cavity hence gets suppressed due to lower cavity susceptibility. Red detuned pump photons scatter into the optical cavity frequency, which is higher than the pump photon frequency, while absorbing a phonon from the mechanical mode. It is the Anti-Stokes sideband that suppressed in the blue detuned case and this time pump photons are more energetic compared to the cavity frequency photons. That leads to the emission of a phonon into the mechanical mode and the

down conversion of the pump photon. Two cases are demonstrated in Figure 1.2. Based on the pump detuning, the interaction hamiltonian H_{int} takes the following forms.

$$\hat{H}_{int} = \begin{cases} \hbar G(\hat{a}^\dagger \hat{b} + \hat{a} \hat{b}^\dagger) & \text{where } \Delta = \omega_m(\text{red}) \\ \hbar G(\hat{a}^\dagger \hat{b}^\dagger + \hat{a} \hat{b}) & \text{where } \Delta = -\omega_m(\text{blue}) \end{cases} \quad (1.18)$$

In the red detuned case, the interaction suggests a beam splitter-like Hamiltonian. The phonon absorption essentially damps and cools down the mechanical mode. This type of interaction can be used for state transfer between optical modes mediated by the mechanical mode. Phonon emission into the cavity in the case of the blue detuned pump tone, for which H_{int} takes the form of the two-mode squeezing Hamiltonian, leads to mode amplification hence heating. Heralded generation of quantum mechanical states can be achieved through this type of optomechanical interaction.

1.3 Hybrid optomechanics

So far, we have focused on phonon–photon interactions in optomechanical systems. Two distinct optomechanical systems operating at different optical frequencies can be designed to share a common mechanical mode, where the mechanical frequency remains the same and interacts with electromagnetic fields at different optical frequencies. If such two systems physically share their mechanical mode, as shown in Figure 1.3a, the hybrid system can be used as a photon-photon frequency converter mediated by the mechanical resonator mutually interacting with the two cavities [17].

A more challenging direction involves applying the same principle to achieve single photon level frequency conversion between photons in two different frequency regimes. One immediate application of such a single photon level coherent frequency converter is to interface quantum processors operating at microwave frequencies via low loss optical fibers using telecom wavelength photons over long distances. This is a crucial component for the quantum processor toolbox since current physical limitations hinder the scalability of the superconductive qubit based quantum processors. Moreover, such a quantum transducer can make it possible to connect individual quantum processors which is crucial to realize quantum networks connecting distant quantum computing nodes [18].

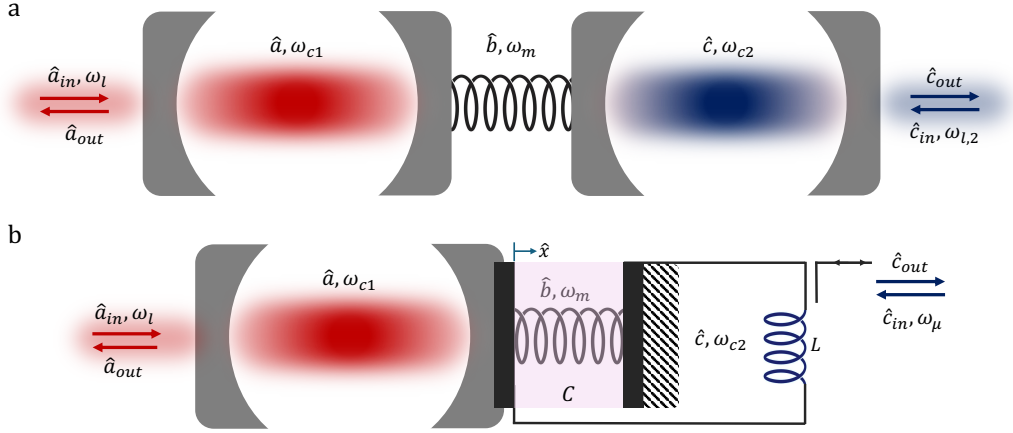


Figure 1.3: **Hybrid optomechanical systems.** **a)** A canonical hybrid optomechanical system composed of two Fabry-Pérot cavities with different optical frequencies that share a common moving mirror mechanical element. **b)** A hybrid optomechanical system composed of an optical cavity and a microwave resonator that share a common mechanical mode. Coupling is provided by the moving mirror on the optical cavity side and a piezo element on the microwave resonator.

Total interaction Hamiltonian of the hybrid optomechanical system can be written as follows:

$$\hat{H}_{int}/\hbar = g_{0,1}\sqrt{n_{c,1}}\hat{a}^\dagger\hat{a}(\hat{b} + \hat{b}^\dagger) + g_{0,2}\sqrt{n_{c,2}}\hat{c}^\dagger\hat{c}(\hat{b} + \hat{b}^\dagger), \quad (1.19)$$

where \hat{a} (\hat{a}^\dagger) and \hat{c} (\hat{c}^\dagger) are creation (annihilation) operators of the two optical modes whereas \hat{b} (\hat{b}^\dagger) is the mechanical mode creation (annihilation) operator. $g_{0,i}$ and $n_{c,i}$ denotes the single photon optomechanical coupling rates and intracavity photon numbers for the two sides of the hybrid system.

For a generic sideband resolved system that is driven with red detuned input fields, we can derive an expression for the conversion efficiency between photons with frequency $\omega_{c,1}$ and $\omega_{c,2}$. Here, the total mechanical mode linewidth in the presence of the red detuned laser is given by $\gamma_{tot} = \gamma_i + \gamma_{OM,1} + \gamma_{OM,2}$ where $\gamma_{OM,i} = 4g_{0,i}^2 n_c / \kappa_{tot,i}$. Maximum achievable conversion efficiency with input fields red detuned by ω_m is as follows:

$$\eta_{max} = \frac{\kappa_{e,1}}{\kappa_{tot,1}} \frac{\kappa_{e,2}}{\kappa_{tot,2}} \frac{4C_1 C_2}{(1 + C_1 + C_2)^2}. \quad (1.20)$$

Here, cooperativity is defined as $C = \gamma_{OM}/\gamma_i$. This expression implies that cavities with high extrinsic coupling rates κ_e and narrow intrinsic mechanical linewidths γ_i , relative to the optomechanically induced damping rate γ_{OM} , can achieve near-unity conversion efficiency—provided that $C_1 \approx C_2$, which requires similar optomechanical coupling rates in both cavities.

In the coming chapters, we will be interested in the schemes where we achieve heralded generation of microwave-optical photon pairs using such a hybrid optomechanical system, so in our hybrid model, we focus on this specific interaction scheme. We use a two-mode squeezing interaction on the first cavity to create an entangled phonon-photon pair. In the second cavity, we use a beam splitter-like interaction where we transfer the created phonon state into a microwave photon.

$$H_{int,1}/\hbar = G_{0,1}(\hat{a}^\dagger \hat{b}^\dagger + \hat{a}\hat{b}) \quad (1.21)$$

$$H_{int,2}/\hbar = g_{0,2}(\hat{c}^\dagger \hat{b} + \hat{c}\hat{b}^\dagger) \quad (1.22)$$

Using this scheme, the hybrid optomechanical system emits an entangled optical-microwave photon pair with the probability p . For an ideal case where we assume no added noise and a weak pump field which eliminates the higher order excitation terms, following expression for the joint state of the modes \hat{a} and \hat{c} can be written as

$$|\psi\rangle = |00\rangle + \sqrt{p} |11\rangle + p |22\rangle + O(p^{3/2}). \quad (1.23)$$

For a more in depth analysis of the topic, see Refs [17, 19].

1.4 Optomechanical crystals

Optomechanical interactions are shown in different platforms with different scales and materials. Although all platforms have strengths and weaknesses, nanoscale silicon optomechanical crystals are proven to be particularly interesting due to the high optomechanical coupling they provide with a very small footprint. They are compatible with well studied silicon fabrication techniques as well as integration with other material platforms including superconducting and opto/piezoelectric materials. Moreover, due to their small volume, nanoscale optomechanical crystals can support high frequency ($\sim GHz$), low loss mechanical modes and low loss optical

modes at telecom wavelengths within the same volume. This comes with the benefit of operating at the sideband resolved regime.

As discussed earlier in this chapter, optomechanical systems can be modeled as a Fabry-Pérot cavity formed between two mirrors with specific physical constraints to allow a mechanical degree of freedom. In the case of silicon optomechanical crystal cavities, a photonic cavity is formed by using mirrors that leverage the periodic refractive index difference between silicon and vacuum. We start by defining position dependent permittivity.

$$\epsilon(\mathbf{x}) = \epsilon_0 \epsilon_r(\mathbf{x} + \mathbf{R}) \quad \text{where} \quad \mathbf{R} = \sum_i m_i \mathbf{a}_i \quad (1.24)$$

Here, ϵ_0 is the vacuum permittivity and $\epsilon_r(\mathbf{x} + \mathbf{R})$ is the periodic, position vector dependent relative permittivity. Periodicity is defined with the lattice vectors \mathbf{a}_i . The eigenvalue equation for the magnetic field in a medium with a spatially varying relative permittivity is giving by

$$\nabla \times \left(\frac{1}{\epsilon_r(\mathbf{x})} \nabla \times \mathbf{H}_m(\mathbf{x}) \right) = \left(\frac{\omega_m}{c} \right)^2 \mathbf{H}_m(\mathbf{x}) \quad (1.25)$$

We defined the lattice with a discrete translational symmetry therefore we can denote the solution in the following form per Bloch's theorem.

$$\mathbf{H}_k(\mathbf{x}) = e^{i\mathbf{k} \cdot \mathbf{x}} \mathbf{h}_k(\mathbf{x}) \quad \text{where} \quad \mathbf{h}_k(\mathbf{x}) = \mathbf{h}_k(\mathbf{x} + \mathbf{R}) \quad (1.26)$$

where \mathbf{k} is the wave vector, and the periodic nature of the function $\mathbf{h}_k(\mathbf{x} + \mathbf{R})$ allows us to define the problem boundaries within a unit cell. For each \mathbf{k} in the unit cell, one can determine the corresponding modes supported by the periodic structure and use this formulation to extract the resulting band diagram. The band diagram reveals frequency ranges that are forbidden for any wave vector, forming the bandgaps.

Just like the electromagnetic fields in a periodic structure, acoustic waves experience similar interference effects in media that exhibit periodically changing elastic properties. Speed of light in silicon is orders of magnitude higher than the propagation speed of mechanical waves. This leads to a difference in the frequency range of the formed bandgaps for optical and mechanical modes by the same physical structure,

therefor it is possible to design a mirror structure with a periodicity that can create a bandgap for telecom wavelength optics and microwave frequency mechanics simultaneously.

1D Optomechanical crystals

Let us start with a simple silicon waveguide supporting a TE like optical mode at $\sim 1550\text{nm}$ (or $\sim 195\text{THz}$) as shown in Figure 1.4a. If we punch several periodically separated holes on our silicon slab to create *vacuum pockets*, as shown in Figure 1.4b, we can induce a periodic change in the effective refractive index on the slab along the longitudinal axis. Based on the hole dimensions, this periodicity in the refractive index creates a band gap that prohibits certain modes to propagate due to the destructive interference that takes place in the transmitted part of the electromagnetic wave, while reflected light undergoes constructive interference dictated by the Bragg condition as discussed earlier. This way, we can make photonic crystal mirrors for the photons of interest. At the same time, periodically patterned silicon slab acts like a mechanical mirror for the breathing mode, since on the hole regions, only two thin pieces of silicon attach the structure together as opposed to the portions in between holes where full slab width is filled with silicon. This gives rise to an elastic periodicity in the media which forms a partial bandgap. For the work presented here, the optomechanical crystal cavities are designed to support optical bandgaps near 194 THz (1550 nm). Depending on the OMC type, mechanical bandgaps are targeted between 5–10 GHz.

To form a cavity using the designed simultaneous optomechanical mirrors, the central holes of the slab are shrunk to create a *defect* region, where the bandgap closes and localized modes can exist. In the defect region, optical and mechanical modes encapsulating the bandgaps are pushed into the bandgap region by the shape modifications introduced. In the case of a one-dimensional optomechanical crystal (1D OMC), this is typically achieved by reducing both the lattice constant and the vacuum pocket size compared to those of the mirror cells. The resulting mirror–defect–mirror configuration can effectively act as a photonic crystal, capable of confining photons within the defect region bounded by optomechanical mirrors. In the 1D OMC, the holes are designed with an elliptical shape, providing two independent radii as tunable parameters. This added geometric flexibility enables simultaneous confinement of both optical and mechanical modes.

However, this design suffers from a critical flaw: out-of-plane scattering at the

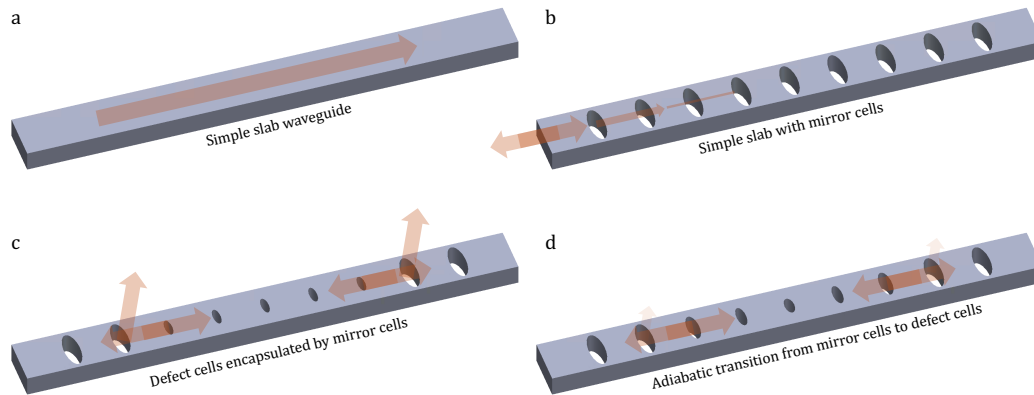


Figure 1.4: **Light confinement within a nanobeam.** **a)** A simple slab waveguide that confines light within its cross section. **b)** A slab with periodically placed mirror cells. Structure acts like a mirror for the light propagates in the longitudinal axis. **c)** An imperfect cavity composed of mirror and defect cells. Light is confined in the defect region, however abrupt transition leads to out of plane scattering. **d)** A refined cavity composed of mirror cells that adiabatically shrink towards the center of the beam to create a more confined defect region. Slowly varying unit cell dimensions minimize the out of plane scattering.

defect–mirror interface. The abrupt transition from the smaller vacuum pocket of the defect to the larger mirror cells disrupts both the structural periodicity and the total internal reflection condition of the underlying waveguide. This disruption introduces an undesired loss channel through out-of-plane scattering (see Figure 1.4c). To mitigate this effect, the transition between the mirror and defect regions is made adiabatic by gradually varying the unit cell geometry typically following a parabolic profile rather than implementing a sharp, step-like change. This approach preserves local periodicity between each neighboring cells, thereby minimizing out-of-plane scattering and improving the confinement quality of the optical mode (see Figure 1.4d).

Another important improvement is optimization of the cavity region to spatially overlap the optical and mechanical modes. This spatial co-localization is essential for enhancing the interaction between the modes, thereby increasing the optomechanical coupling strength, g_0 , which plays a central role in determining the performance of OMCs [7].

An example of a one-dimensional optomechanical crystal cavity is shown in Figure 1.5a, with the mirror and defect cell regions indicated. As discussed previously, the mirror cells, which contain elliptical vacuum pockets, provide an optical bandgap around

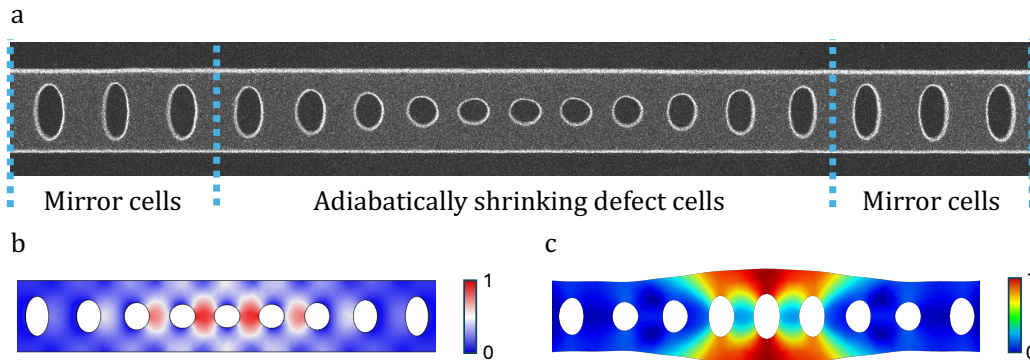


Figure 1.5: **1D OMC.** **a)** SEM image of a 1D OMC showing mirror cells on the left and right ends. Defect cells are located in the middle section and they are formed by adiabatic shrinkage of the mirror cells. Defect region supports a 194THz (1550nm) TE-like optical mode along with a 5GHz mechanical breathing mode. Normalized field distribution of the **b)** optical and **c)** mechanical showing electric field intensity and displacement respectively.

194THz and a partial mechanical bandgap around 5GHz. By gradually shrinking the mirror cells toward the center of the nanobeam, defect cells are formed. Defect cells are engineered to support a confined TE-like optical mode (see Figure 1.5b) at 194THz (approximately 1550nm) and a mechanical breathing mode (see Figure 1.5c) at 5GHz. The tight spatial confinement of these two spectrally distant modes enables strong optomechanical coupling.

Unlike the Fabry–Pérot example, where optomechanical coupling is achieved through physical displacement of mirrors, our photonic crystal design leverages localized mechanical motion within the cavity. This motion modulates both the geometry boundaries and the effective permittivity $\varepsilon(\mathbf{x})$ of the silicon slab, facilitating phonon-photon interactions. Specifically, in 1D OMCs, a breathing-like mechanical mode concentrated at the central defect cell efficiently overlaps with the optical field and drives the interaction.

Optomechanical coupling rate g_{OM} can be calculated as the change of the optical cavity frequency with respect to mechanical displacement.

$$g_{OM} = \frac{\partial \omega_c}{\partial u} \quad (1.27)$$

ω_c is the optical resonance frequency, u is the displacement amplitude and \mathbf{E} is the electric field. Using perturbation theory and the unperturbed electric field of the

optical mode of interest, we can calculate g_{OM} as follows:

$$\frac{\partial \omega_c}{\partial u} = -\frac{\omega_c}{2} \frac{\int d^3 \mathbf{x} \mathbf{E}^*(\mathbf{x}) \cdot \frac{\partial \varepsilon(\mathbf{x})}{\partial u} \mathbf{E}(\mathbf{x})}{\int d^3 \mathbf{x} \mathbf{E}^*(\mathbf{x}) \cdot \varepsilon(\mathbf{x}) \mathbf{E}(\mathbf{x})}. \quad (1.28)$$

The general expression can be isolated to address the two effects that give rise to the optomechanical coupling. To isolate the moving boundary effect ($g_{OM,mb}$), we can ignore $\partial \varepsilon(\mathbf{x})/\partial u$ which assumes no change in refractive index due to the strain. In this scenario, strain only moves the boundaries of our dielectric slab. On the other case where we are interested in the photoelastic effect ($g_{OM,pe}$), change in refractive index due to the mechanical motion, we assume no change in the dimensions.

$$g_{OM,mb} = -\frac{\omega_c}{2} \frac{\int dA \mathbf{q}(\mathbf{x}) \cdot \hat{\mathbf{n}}(\mathbf{x}) (\Delta \varepsilon \langle \mathbf{E}_{\parallel}(\mathbf{x}) \rangle^2 - \Delta \varepsilon^{-1} \langle \mathbf{D}_{\perp}(\mathbf{x}) \rangle^2)}{\int d^3 \mathbf{x} \varepsilon(\mathbf{x}) \langle \mathbf{E}(\mathbf{x}) \rangle^2} \quad (1.29)$$

$$g_{OM,pe} = \frac{\epsilon_0 \epsilon_x^2 \omega_c}{2} \frac{\int dV E_i^*(\mathbf{x}) E_j(\mathbf{x}) p_{ijkl} S_{kl}(\mathbf{x})}{\int d^3 \mathbf{x} \varepsilon(\mathbf{x}) |\mathbf{E}(\mathbf{x})|^2} \quad (1.30)$$

where $\mathbf{q}(\mathbf{x})$ is the normalized mechanical displacement, $\hat{\mathbf{n}}$ is the surface normal vector, \mathbf{D} is the electric displacement field, $\Delta \varepsilon = \varepsilon_0(\varepsilon_{Si} - 1)$, S is the displacement field and p is the photoelastic tensor. The combination of the two components gives the total optomechanical coupling g_{OM} .

Phononic shielding

Although the 1D OMC slab exhibits a quasi-phononic bandgap, mechanical energy leakage can still occur due to coupling between the targeted breathing mode and modes with unprotected symmetries. Even for z-symmetric modes, nominally confined by the elliptical holes through the bandgap, imperfect verticality in the etching process can break symmetry and introduce additional loss channels. This leakage of mechanical energy into the bulk can be mitigated by incorporating phononic shielding structures engineered to support a full mechanical bandgap. Such shields have been developed and successfully employed in the Painter Lab to demonstrate ultrahigh mechanical quality factors [20].

A quasi-2D phononic shield array is composed of a 2D grid of rectangular blocks and tethers that interconnect the blocks. Structure can be modeled as small and large masses connected with springs. Large masses are excited with low frequency phonon modes while the small masses have higher frequency resonances which

gives rise to a mechanical bandgap. In the planar realization of this structure, thin tethers make the shield array more 'wobbly' (hence support lower frequency modes) while the blocks individually support higher frequency modes. Here as the size contrast between the tether pieces and the blocks increases, the band gap realized becomes larger. A very detailed analysis on the topic and different structures can be found in Ref. [21].

Part I

**Tuning Hybrid Optomechanical
Crystals**

Fueled by significant efforts in both research and industry [22–25], superconducting quantum processors operating at microwave frequencies are a promising platform for building quantum computers. Despite their remarkable capabilities, these systems face a fundamental limitation: their reliance on microwave photons, which are poorly suited for long-distance transmission due to thermal noise at the room temperature and significant attenuation in standard communication channels. This limitation enforces the quantum processor to be kept in well controlled ultra-cold environments to maintain their quantum nature. Efforts to extend the ultra-cold environment between two dilution refrigeration units to entangle distant quantum nodes were shown [26], however this is still far from being a scalable approach towards building larger quantum networks connecting many quantum processors.

On the other hand, as discussed in the previous chapter, optomechanical crystals emerged as a promising platform for single quantum level phonon-photon transduction and pair generation. Later emergence of various hybrid optomechanical systems which integrate optical and microwave cavities on the same device architecture with a mechanical intermediary showed the potential of such hybrid systems for generation of entangled pairs of photons with drastically different frequencies [27]. This is a key achievement towards building quantum networks [18] that interconnect distant superconductive quantum processors with optical links since terahertz frequency optical photons are suitable for lossless transmission due to their resilience to the thermal noise at room temperature, moreover, optical fibers that are readily available promise very low transmission losses as low as $\sim 0.15\text{dB/km}$.

Suggested entanglement scheme uses DLCZ protocol [28] in a system that consists of two piezo optomechanical microwave-optical transducers located in separate dilution refrigerators, connected to two different qubit modules via low-loss microwave interconnects. On the optical side, transducers are connected via optical fibers at a 50/50 beam splitter that is probed on each output port with single photon detectors (SPDs). The simplified schematic is shown in Figure 1.6. Transducers pumped with a blue detuned ($\Delta = -\omega_m$) laser pulse to induce creation of an entangled photon-phonon pairs at each transducer. Down converted photons at cavity frequencies $\omega_{c1,1}$ and $\omega_{c1,2}$ are emitted while the state of the created microwave phonons is mapped into a microwave photon on each piezoacoustic cavity by a beam splitter interaction. Created microwave photons are sent to the qubit modules in each system while the emitted optical photons interact in a beam splitter. Output ports are probed with a pair of single photon detectors (SPD1 and SPD2).

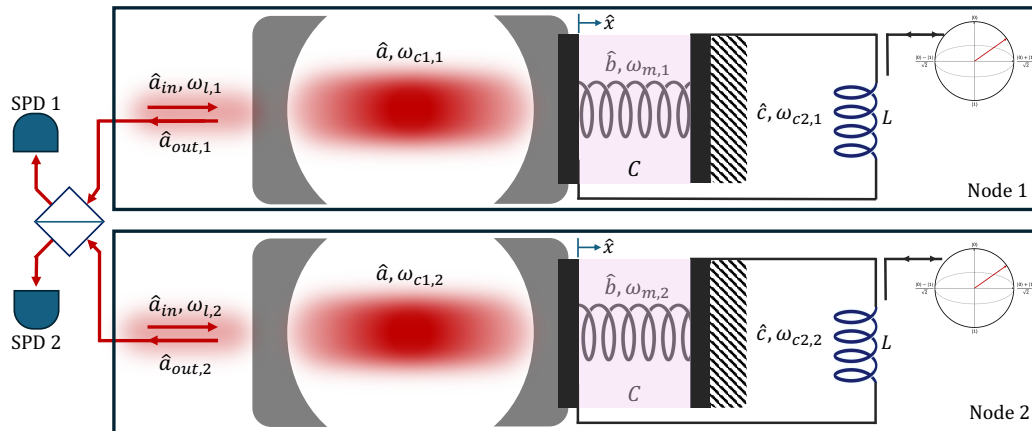


Figure 1.6: **Remote entanglement with hybrid optomechanical systems.** Two hybrid piezo optomechanical cavities are driven to create pairs of optical and microwave photons. Emitted optical photons are combined in a 50/50 beam splitter to achieve heralded entanglement distribution between individual distant nodes.

To achieve entanglement in this scheme, the emitted photons from the individual nodes of the network must be indistinguishable. This indistinguishability condition erases the which-path information on the beam splitter and a single click is observed on either SPD1 or SPD2 that heralds the distribution of entanglement between two nodes. This requirement forces the optical modes of the individual hybrid optomechanical crystals to be at the same wavelength within their linewidths. State of the art fabrication techniques promise nanometer level control over the dimensions of the fabricated nanostructures, nonetheless this is still not enough to repeatedly fabricate identical optomechanical crystals. Several approaches were proposed for post-fabrication mode tuning of the optical and mechanical nanostructures such as gas condensation [29–31], strain tuning [32–34], thermo optic tuning [35–37], laser assisted thermal oxidation [38, 39], using electro-optic, acousto-optic modulators and nonlinear optical wave mixers [40]. Nonetheless, proposed and demonstrated techniques either severely degrade the optical and mechanical quality factors, fail to selectively tune the individual modes, introduce unacceptable transmission losses on the system or they are not suitable with the cryogenic operation conditions.

We propose using Atomic Force Microscopy (AFM) nano-oxidation technique to selectively tune optical and acoustic modes of an optomechanical crystal to achieve a nondestructive, repeatable, high range and high precision tuning. The atomic force microscope (AFM) nano-oxidation technique has been used to realize polarization degenerate microcavities [41] and to create low-loss microcavities from line defects

in a photonic crystal [42]. However, since OMCs co-localize optical and acoustic resonances in a wavelength-scale volume, selective tuning of both optical and acoustic resonances without adding significant scattering losses is a complex endeavor and an outstanding technical challenge. In Part I, we will provide an in depth analysis of the problem with the proposed and demonstrated methods of tuning using AFM nano-oxidation technique. We conclude Part I with a discussion on the broader potential of the conductive AFM technique, exploring the diverse functionalities it can enable beyond resonance tuning on silicon optomechanical device platforms.

*Chapter 2***IN SITU TUNING OF OMCS WITH AFM NANO-OXIDATION****2.1 Nanofabrication induced imperfections**

In 1959, when Richard Feynman gave his lecture on the possibilities of having a whole new world in nanoscale and suggested that machines consisting of nanoscale components can be built someday, our ability to create such small-scale devices was next to nonexistent. Over the years, micro and nano fabrication techniques came a long way. During the next few decades following Feynman's foresight, several very important achievements were made including the invention of Scanning Electron Microscopy and Atomic Force Microscopy. Invention of Electron Beam Lithography was the point we start making the first engineered nanoscale devices. Today in 2025, more than a half century later, capabilities of nanoscale fabrication techniques are at a remarkable stage. Now, with conventional state of the art techniques, we can make nanostructures on the order of few nanometers repeatably. However, along with the evolving new technologies, our applications are getting more demanding and the level of precision required to achieve desired outcomes is getting harder to attain. In this section, we study the limits of the state-of-the-art techniques that we utilize to fabricate the optomechanical crystals used in this work.

Optomechanical crystals being studied in this work were fabricated on Silicon on Insulator (SOI) wafers that consist of 220nm doped silicon device layer, a 3 μ m thick buried silicon dioxide insulator layer (BOX) and a 625 μ m Si handling layer. A 250nm thick positive electron beam resist, ZEP 520A, is used to pattern the OMC features on the device layer. For the electron beam lithography process, a Raith Electron Beam Pattern Generator (EBPG) 5200 with a 100keV, 150pA beam is utilized. After the patterning, samples undergo a dry etch process with a SF₆/C₄F₈ plasma to define the OMC features on the underneath device layer. A more detailed discussion on fabrication steps can be found in Appendix A.

As a baseline for our analysis, we only consider the errors introduced during the electron beam lithography stage for the sake of simplicity. Real world imperfections are expected to be worse due to other sources of error introduced by other steps in the process. We discuss additional sources of imperfections later in this section.

According to Raith EBPG 5200 technical data sheet, best achievable resolution is

less than 5nm along with a stitching accuracy of less than 8nm [43]. These metrics are used as we numerically test the effect of the imperfections on designed optical wavelengths and mechanical frequencies.

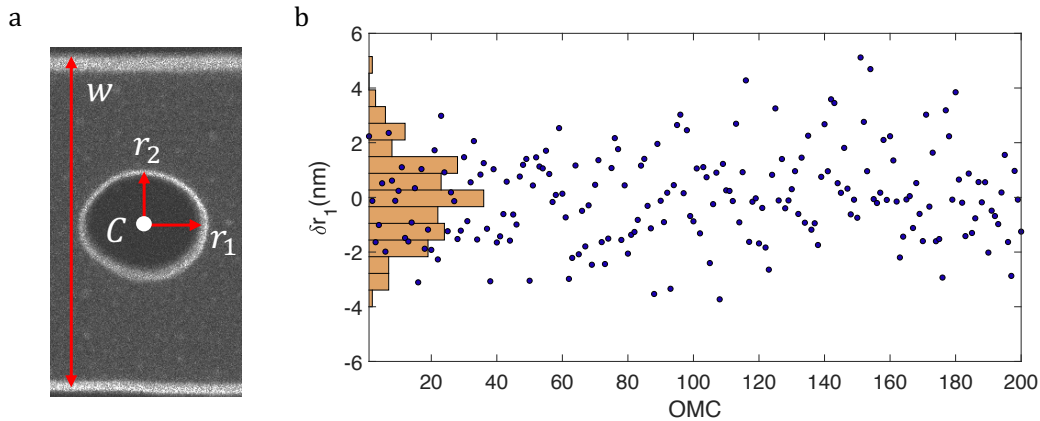


Figure 2.1: **Wavelength dispersion analysis with 200 imperfect OMCs.** **a)** A sample OMC hole and the respective dimensions that are manipulated. w denotes the beam width, radii r_1 and r_2 define the ellipse size while C denotes the ellipse center coordinates. Each hole's dimensions and center point coordinates were altered with a randomly generated imperfection while beam width is altered with a single perturbation per OMC (following a normal distribution). **b)** Example distribution of the perturbation applied on the center hole r_1 for each simulated OMC. The standard deviation of the normally distributed perturbations is $\sim 1.6nm$. A histogram of the distribution is given on the vertical axis.

Using COMSOL Finite Element Method (FEM) numerical analysis tool, we simulate the optical and mechanical resonance frequencies of optomechanical crystals while introducing random position and size defects. Position defects are only applied to ellipse center locations while size defects are applied on both ellipse radii and slab thickness as shown in Figure 2.1a. Each type of defect introduced in the simulations is randomly assigned with a random normal distribution limited by the best achievable accuracy based on the Raith EBPG 5200 technical data sheet, $3\sigma=5nm$. An example set of 200 randomly generated perturbations on the dimension r_1 is presented in Figure 2.1b along with the distribution histogram on y-axis. Each simulation corresponds to a single device patterned individually and assumed to be exposed to identical pre and post processes.

A typical 1D OMC can have an intrinsic optical quality factors on the order of few 10^5 and mechanical quality factors on the order of 10^3 at room temperature¹

¹At cryogenic temperatures and under vacuum, many dominant room temperature loss channels

based on the surface quality and imperfections of the features. For the comparison, let us assume that we have a critically coupled OMC with a Q_i of 3×10^5 , and a mechanical resonance Q_m of 2×10^3 . For a typical OMC designed at $\lambda_0 = 1537nm$, $\omega_0 = 5GHz$, this quality factor corresponds to an optical resonance linewidth of $\sim 10pm$ and a mechanical resonance linewidth of $\sim 3MHz$. A measured spectrum for each mode that represents the assumed case is shown in Figure 2.2.

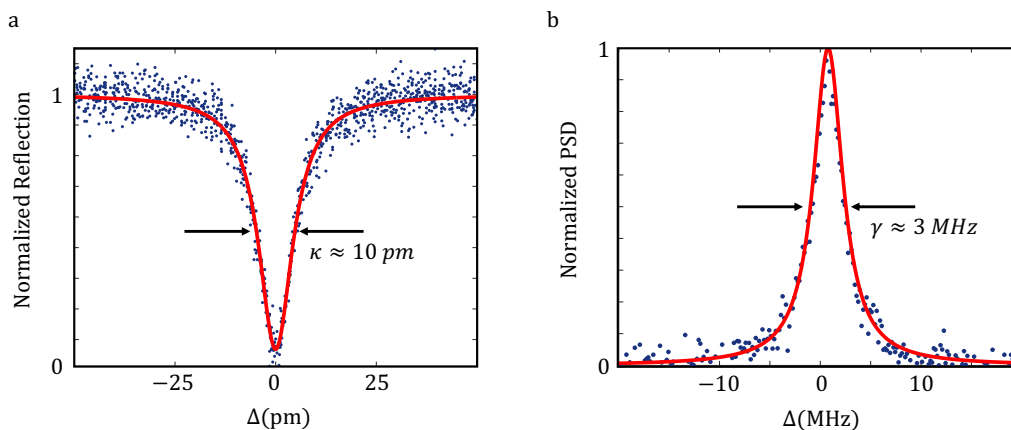


Figure 2.2: **Typical optical and acoustic modes.** Typical resonance peaks for **a)** optical and **b)** acoustic modes with their respective linewidths.

Our FEM simulations of imperfect OMCs suggest that the standard deviation of the resulting wavelength distribution is $\sigma_\lambda = 1.2nm$ which is roughly 100 times of a typical optical resonance linewidth whereas the standard deviation of the mechanical frequency distribution over 200 OMCs, $\sigma_m = 12.3MHz$, is four times the typical mechanical linewidth. Absolute value of the resulting mode variation for both optical ($|\delta\lambda|$) and acoustic mode ($|\delta\Omega_m|/2\pi$) are shown in Figure 2.3. Orange and blue shaded regions indicate the corresponding typical mode linewidths.

Note that simulated variations in device resonances are only due to the expected errors induced by the electron beam lithography. For other fabrication steps, individually quantifying every single source of imperfection is not possible or feasible, hence we compare measured resonance frequencies of 20 identically designed OMCs. These 20 individual OMCs were patterned on the same SOI die, positioned next to each other and etched at the same time, under same conditions.

get suppressed which leads to a much narrower acoustic mode linewidth on the order of $\ll 1kHz$ for pure OMCs [20] and $\sim 100kHz$ for typical hybrid OMC transducers [27]. However in this chapter, we only present the findings of room temperature tests hence we use the room temperature, atmospheric pressure reference values.

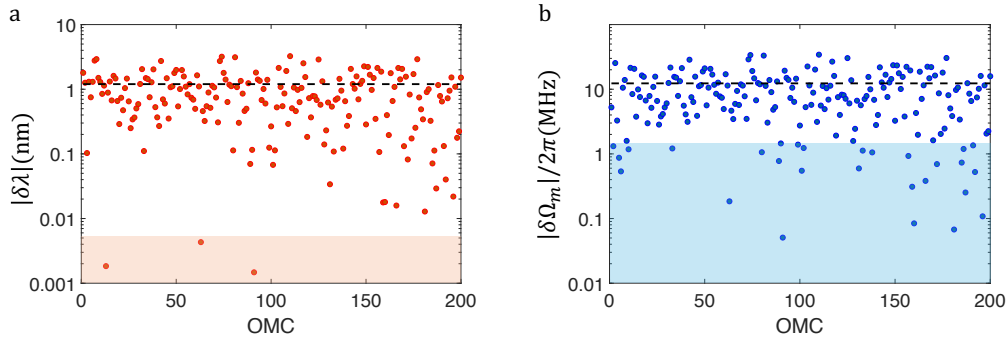


Figure 2.3: **Mode deviations from the unperturbed case for 200 'imperfect' OMC.** Absolute value of the **a)** optical mode wavelength and **b)** acoustic frequency variations from the reference case for 200 simulated OMCs. Dashed lines indicate the standard deviation for both modes while the shaded areas (orange for optics and blue for acoustic mode) represent the respective reference linewidth.

The measured optical wavelengths (see Figure 2.4) exhibit a standard deviation of 2.58 nm, more than 2 orders of magnitude higher than the typical optical linewidth κ_i while the mechanical frequency distribution shows a standard deviation of 19.8 MHz, nearly 7 times of the mechanical linewidth γ of a typical mechanical resonance at room temperature. A noticeable discrepancy exists between the simulated and measured resonance distributions. This gap shows the significance of device-to-device variations, even when all fabrication steps are carried out nearly identically.

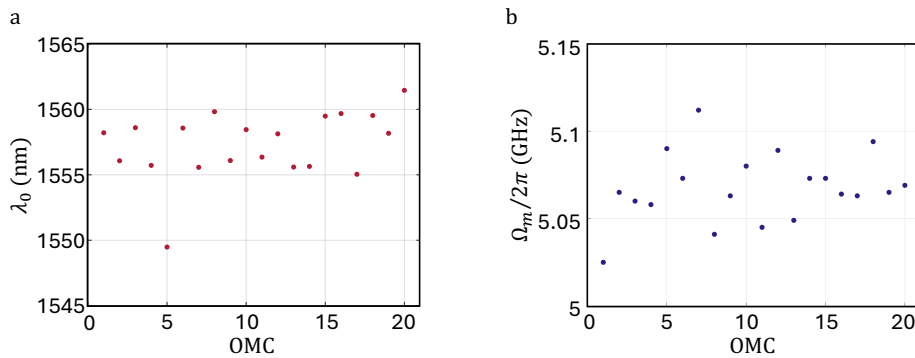


Figure 2.4: **Optical and acoustic modes for 20 fabricated OMC.** **a)** Optical mode wavelengths and **b)** acoustic mode frequencies for 20 identically designed and fabricated OMCs.

Potential sources of imperfection include variations in the thickness of the silicon device layer, inconsistent electron beam resist thickness, local differences in resist development, and variations in plasma properties during the etching process. In

this test, to minimize these local effects, we pattern all the OMCs on the same SOI die. However, more significant device-to-device variations are expected in OMCs fabricated on different dies.

In this section, we explored the nanofabrication-induced imperfections that pose significant challenges in fabricating OMCs with identical resonant properties. In the next section, we will discuss methods for tuning imperfectly fabricated OMCs using the AFM nano-oxidation technique.

2.2 AFM nano-oxidation fundamentals

This section provides an overview of Atomic Force Microscopy (AFM), beginning with fundamental operating principles followed by an in-depth introduction of a specific mode of operation related to this work, nano-oxidation. The chapter concludes with preliminary characterization of AFM-induced nano-oxidation on a silicon surface.

Atomic Force Microscopy

Atomic Force Microscopy (AFM) is an atomically high-resolution imaging technique that is used for topology measurements at nanoscale as well as mechanical properties using mechanical or long-range interactions between the sample and a microscale cantilever [44, 45]. AFM takes advantage of a sharp tip, typically tens of nanometers to a few nanometers wide at the sharpest point, mounted on a microscale cantilever, typically made from a silicon compound. The cantilever deflection, hence indirectly the oscillation amplitude and phase for some modes of operation, is measured with a photodetector using a laser beam reflected off its back surface, and the cantilever position and/or frequency are actively controlled with a feedback loop. AFM tip deflects in response to forces between the tip and the surface, and the deflection detected by the photodetector is converted into surface data based on the operation mode being used. A schematic visualizing the basic working principle of AFM is given in Figure 2.5a.

AFM measurements usually do not require any specific environmental conditions such as vacuum, moreover in some specific applications, especially in biological applications [46–48], sample can even be submerged into a liquid environment [49] which makes AFM a versatile tool for various samples and conditions.

There are three main modes of operation that AFM cantilever can be operated; contact mode non-contact mode and tapping mode. These three modes correspond

to two different tip surface interaction regime given by the Lennard-Jones potential [50], shown in Figure 2.5b. Contact mode operates at the regime where the tip experiences repulsive forces due to very small ($d \rightarrow 0$) tip-surface separation. Non-contact mode operates at the negative potential regime where the tip experiences attractive forces due to increased tip-surface separation. Tapping mode operates in both regimes since the oscillating tip is operated very close to the surface.

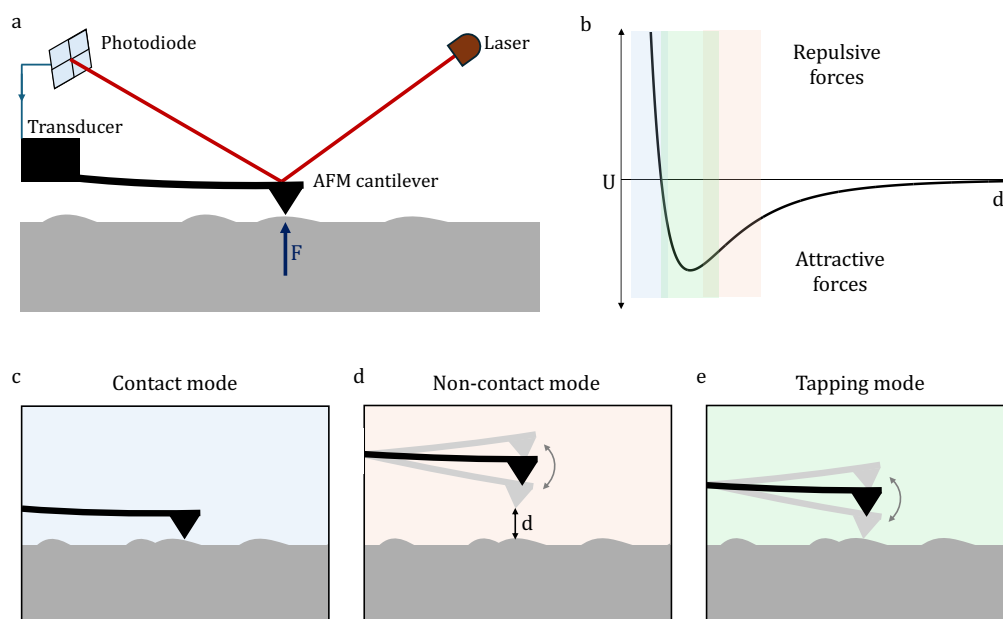


Figure 2.5: **Atomic Force Microscopy.** **a)** A schematic for the basic working principle of the Atomic Force Microscope (AFM). Interaction between the surface and the AFM tip attached on a microscale cantilever is probed using a laser and a photo detector. Cantilever is controlled in real-time based on the data fed back by the photo detector. **b)** Lennard Jones potential between the tip and the sample surface with respect to the tip-sample distance. **c)** Contact, **d)** non-contact and **e)** tapping modes of operation of the AFM. The sub-figures are color-coded according to the corresponding Lennard-Jones potential regime (**b)** in which different modes operate.

Contact mode

In contact mode, AFM tip comes into continuous contact with the sample surface during the measurement (see Figure 2.5c). AFM tip experiences various forces while being scanned on the sample surface. Exerted forces on the tip based on the local material properties and surface topology cause cantilever to deflect and the detected deflection by the PSD is then converted into force based on the known mechanical properties of the cantilever such as the first moment of inertia and the

Young's modulus, or simply the effective spring constant. AFM feedback control loop adjusts cantilever height to keep the cantilever deflection, hence the exerted force, constant. This mode can be successfully performed on hard surfaces however soft or suspended samples are less suitable for contact mode due to the possible measurement induced deformations on the sample.

Non-contact mode

In the non-contact mode, AFM cantilever oscillates above the sample surface such that the tip comes very close to the sample surface, but no physical contact is made (see Figure 2.5d). Cantilever resonance frequency gets affected by the long-range interactions and resulting forces between the surface and the tip. Two of the main forces that perturb the cantilever oscillation frequency are Van der Waals forces and electrostatic forces. Similarly to the contact mode, laser beam reflected off the cantilever is used to probe the oscillation frequency and the resulting shifts due to the sample-tip interactions. The feedback loop adjusts the cantilever height to account for the change in oscillation frequency. Cantilever is driven slightly below its fundamental resonance frequency, which can be tens or hundreds of kHz, where any change in resonance frequency of the cantilever can be detected thanks to the high slope in the Lorentzian resonance response. This mode of operation is especially useful when imaging delicate samples since there is no physical contact between the sample and the AFM tip.

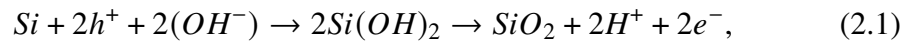
Tapping mode

Tapping mode can be seen as a hybrid mode where AFM cantilever oscillates over the sample surface while intermittently makes contact with the sample at the peak of its oscillation (see Figure 2.5e). When AFM tip briefly contacts the sample, dissipated energy alters the oscillation amplitude and phase of the unperturbed resonance frequency. This change is a function of the height where the tip makes contact with the sample, sample hardness and other long-range interactions between the sample and the tip. Similarly to previously discussed methods, changes in the oscillation amplitude are detected by the photodetector, then cantilever height is adjusted to maintain a constant oscillation amplitude. This is a relatively more precise technique than non-contact mode for surface topology analysis without being as destructive as contact mode, hence seen as a superior method to apply on delicate samples.

2.3 Conductive AFM (cAFM) and AFM nano-oxidation

As AFM continues to evolve, one operation mode has gained significant attention: conductive AFM (cAFM) [51]. cAFM offers new possibilities for studying the electrical properties of materials at the nanoscale [52], bridging the gap between traditional AFM imaging and advanced electronic characterization. Technique leverages a conductive AFM tip to apply a small voltage to the sample while scanning, enabling the detection of local currents and electrical conductivity which makes it a useful way for studying materials like semiconductors, piezoelectric materials and thin films [53, 54]. Moreover, cAFM can induce localized chemical reactions allowing for the manipulation of local material properties [55].

Next sections of this chapter focus on AFM nano-oxidation, a particular application of the cAFM where biased conductive AFM tip is used to induce local oxidation on samples [56]. When a biased conductive AFM tip comes to close vicinity of the grounded sample surface, a highly focused electric field forms between the tip and the sample. In the meanwhile, a water meniscus forms within the nanometer scale gap between the tip and the sample surface. Formation of the water meniscus can be explained with the attraction of the polarized water molecules towards the interface due to the applied tip voltage and the capillary forces created in the small gap in a sufficiently humid environment. Electrolysis of the water molecules produces OH⁻ and H⁺ ions in the water meniscus. OH⁻ ions attracted towards the silicon sample surface by the created electric field eventually induce the oxidation reaction of the silicon within the base of the nanoscale water meniscus. Half-cell reaction taking place at the anode (sample surface) is as follows [57]:



while the hydrogen ions and excess electrons form hydrogen gas at the cathode (AFM tip) to complete the reaction.



Carefully controlling the tip-surface interactions and the electric field created in the interface, one can form few-atoms thick oxide layers confined in tens of nanometers [57]. A simplified schematic showing the nano-oxidation process is given in Figure 2.6.

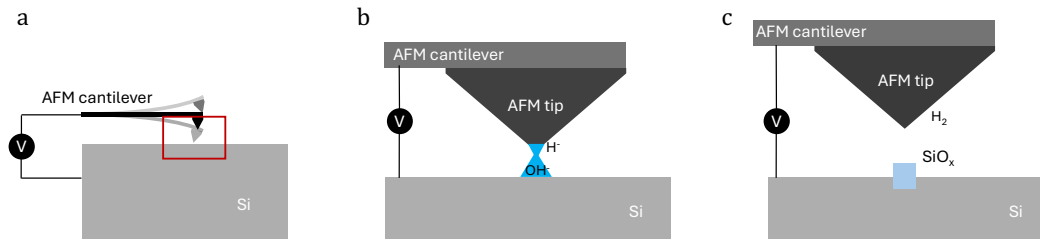


Figure 2.6: **Nano-oxidation mechanism.** **a)** Voltage applied on an AFM cantilever with a Cr/Pt coated tip while the sample is grounded. **b)** When the tip approaches the sample, a water meniscus forms between the tip and the surface. Applied voltage difference separates OH^- and H^+ ions. **c)** OH^- ions are drawn towards the sample and oxidize the silicon sample layer.

The next section will present the experimental characterization of the nano-oxidation process on a silicon sample under different operating conditions.

2.4 Nano-oxidation of silicon

Oxide formation on silicon using AFM nano-oxidation is demonstrated with several AFM operation modes including contact, tapping and non-contact modes [58]. Although there are earlier studies that present results with non contact mode nano-oxidation [59], we focus on contact and tapping modes in this section given their potential to grow thicker (and deeper) oxide layers without needing a high tip bias voltage due to the increased tip-sample interaction. The results of this characterization guide the selection of parameters for subsequent mode tuning experiments.

In the contact mode operation, one can manipulate the oxidation process by changing the contact force, dwell time or tip bias voltage. Contact force refers to the force exerted by the AFM tip on the sample surface, dwell time is the time spent on a single pixel during the oxidation process; and tip bias voltage is the voltage difference applied between the AFM tip and the grounded sample surface. Among these variables, contact force must be kept at the minimum possible value that can be reliably used to oxidize suspended structures without causing structural damage. Contact force is maintained at $F_c = 0.3nN$ throughout the contact mode study, a level deemed safe for operation on suspended optomechanical crystals. Dwell time is fixed at 200ms where scan speed is $\sim 200nm/s$ for scanning based oxidation. Surface oxidation is tested with varying tip bias voltages and resulting oxide is probed using AFM in tapping mode.

Oxide lines are created with scanning oxidation using a tip bias voltage ranging

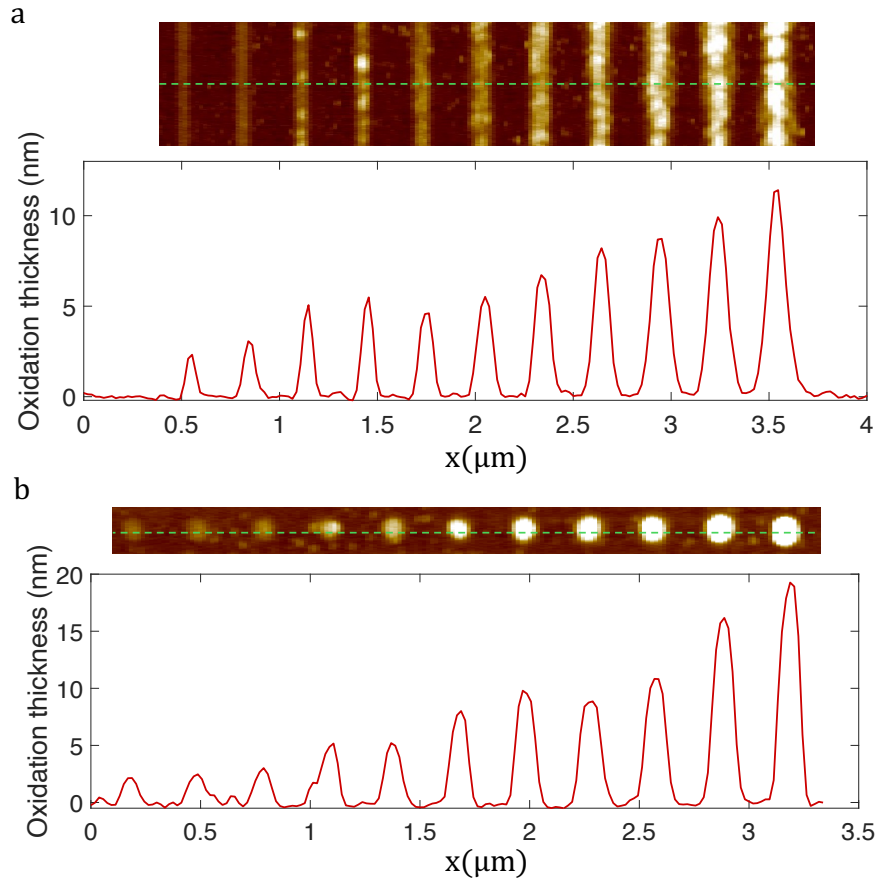


Figure 2.7: **Contact mode oxidation characterization.** **a)** Oxide lines created using scan speed of 250nm/s and tip bias voltages ranging from 5V to 10V with 0.5V increments and corresponding thickness profile taken along the green dashed line. **b)** Oxide pixels created using dwell time $t_{dw} = 200\text{ms}$ and tip bias voltages ranging from 5V to 10V with 0.5V increments and corresponding thickness profile taken along the green dashed line.

from 5 V to 10 V in 0.5 V increments. The tip voltage was applied as a 25 Hz square wave. Resulting surface profile is measured using AFM in tapping mode and plotted in Figure 2.7a. Oxidation thickness is 2.5nm at $V_{tip} = 5\text{V}$ and goes up to 11.5nm at $V_{tip} = 10\text{V}$. Full width half maximum of the oxide lines are measured to be $\sim 72\text{nm}$ and $\sim 110\text{nm}$ for $V_{tip} = 5\text{V}$ and $V_{tip} = 10\text{V}$, respectively.

Single-pixel oxides were created using a tip bias voltage ranging from 5 V to 10 V in 0.5 V increments. The tip voltage was applied as a 25 Hz square wave. The resulting oxide pixel profiles are measured using AFM in tapping mode (see Figure 2.7a). Measurements suggest that oxidation thickness of $\sim 2\text{nm}$ can be achieved at 5 V and higher tip bias voltages result in thicker oxide layers, as thick as $\sim 19\text{ nm}$ at

$V_{tip} = 10V$ and $t_{dwell} = 200ms$. Although thicker oxide layers can be obtained using longer t_{dwell} , we already are able to create thick enough oxide layer using higher voltages, hence t_{dwell} is fixed at 200ms which provides a fast enough oxidation process. Full width half maximum of the created pixels are ranging from $90nm$ at $V_{tip} = 5V$ to $110nm$ at $V_{tip} = 10V$.

Tapping mode oxidation features can be controlled by changing the tip separation set point and dwell time. Here, set point refers to the distance between the AFM tip and the sample surface at the highest oscillation position of the AFM tip, whereas the dwell time is the duration over which oxidation reaction takes place, similarly to the contact mode. Here we use tip bias voltage of $V_{tip} = 10V$ which is the maximum voltage that can be applied internally, using our AFM setup. Surface oxidation is tested and resulting oxide is probed using AFM at tapping mode.

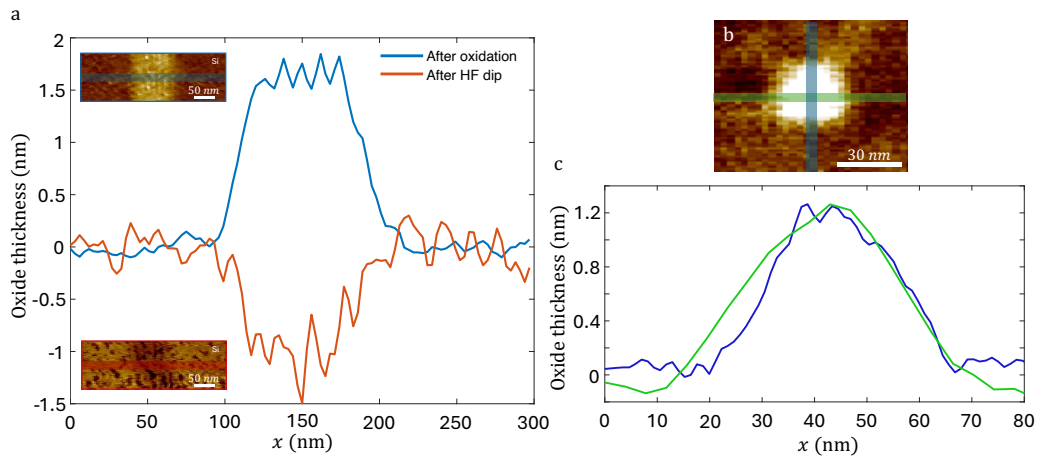


Figure 2.8: **Oxidation with tapping mode.** **a)** Height/depth profile of an oxide line created with tapping mode using a set point value of 15nm and scan speed of 100nm/s and etched using hydrofluoric acid. **b)** An oxide pixel created using tapping mode with with the same settings. **c)** Height profile of the oxide pixel shown in the panel **b**.

The nano-oxidation process generates oxide beneath and above the surface of silicon. To test the oxidation amount over and under the silicon air boundary, an oxide line is created using a set point value of 15nm and scan speed of 100nm/s. Height profile of the created oxide is measured using AFM. Next, oxidized sample is dipped into hydrofluoric acid to get rid of the oxide created on the silicon sample and depth profile of the resulting trench is measured. Results shown in Figure 2.8a suggest that the oxide thickness above the surface is approximately 60% of the total oxidation whereas 40% of the oxide forms under the surface. Figure 2.8b,c shows

the characterization of a single oxide pixel generated with the same settings. The size of the pixel is approximately 25nm along both x and y axes.

2.5 Nano-oxidation on OMCs

This section revolves around the application of the nano-oxidation technique to tune the resonances of OMCs. We begin by introducing the proposed tuning method, followed by a description of the experimental setup. Preliminary results from the tuning characterization experiments are then presented along with the introduction of a tuning algorithm. The chapter concludes with the fine-tuning methods for OMCs in the real-time feedback operation mode.

Proposed OMC tuning method with nano-oxidation

Optomechanical crystals confine optical and mechanical resonances in the nanometer scale mode volume. The mode volume is formed by the adiabatic shrinkage of the defining ellipse patterns and the periodicity of the unitcell from the ends of the OMC towards the middle of the nanobeam which follows a parabolic relation. Shrinking ellipse pattern with changing lattice constant effectively increase the refractive index within the unit cell and change the band structure to allow modes to form rather than prohibiting their propagation. At the same time, shrinking ellipses form a mechanical resonator that supports a breathing mode centered in the middle of the parabola, confined within a few unitcells.

One can tune the optical and mechanical frequencies of an OMC by changing the parameters of the parabola that governs the change in unitcell dimensions. By scaling the whole geometry while keeping the parabolic relations the same, the periodicity of the structure, which changes the optical and mechanical resonances, can be altered. On the other hand, changing the hole radii of the center unitcells, employing a shallower or deeper parabola, alters the effective volume of the silicon within unit cells, hence the localized mode red (blue) shifts based on decreasing (increasing) silicon volume contributing to the mode. This results in a decreased optical frequency and increased wavelength. At the same time, effective mass decrease in the unitcell with the increasing hole size results in an increase of the mechanical frequency of the breathing mode.

Once the OMC is fabricated and released, the hole dimensions and lattice constants that dictate the resonance frequencies are virtually fixed². So, we can assume that the

²Native oxidation of the OMCs cause a drift in the resonance frequencies by changing the material properties on the OMC surface. This will be discussed in Chapter 3.

effective refractive index and the effective mass for the unitcells that form the mode volume are constant. nano-oxidation, by altering the surface of the silicon, presents a big potential to ‘trim’ the local mass and the refractive index after fixing the features. Silicon oxide compounds that can be generated with AFM nano-oxidation have lower refractive index compared to that of silicon at the near infrared regime where $n_{oxide} \approx 1.45$ compared to $n_{si} \approx 3.45$. When the surface is oxidized, a thin film of silicon is transformed into silicon oxide and effective refractive index decreases within the silicon boundary. The change in the local refractive index can lead to an increase in the optical resonance frequency of the OMC, if the oxide patches align with the high electric field intensity regions of the supported TE-like mode. On the other hand, effective mass and Young’s Modulus of the oxidized silicon surface change due to addition of the extra material and alteration of the chemistry. Mass increases locally in the oxidized portions whereas the Young’s Modulus decreases as the Young’s modulus of the silicon oxide compounds are roughly one third as of silicon. Oxide patches that align with the volumes of the OMC where high displacement is observed decreases the mechanical frequency simply because the increased mass participating the mode. The change in the Young’s Modulus has a minimal effect on the resonance frequency since the decrease of the Young’s modulus is balanced out by the increase in the cross section of the local patch which keeps the strain constant.

AFM nano-oxidation method is shown to be capable of creating fine features as thin as less than a nanometer with lateral dimensions on the order of tens of nanometers. This makes AFM a great tool to target fine volumes where optical and mechanical modes are confined. The resolution attainable is well within the wavelength of the resonant modes and individual nodes and antinodes of standing electromagnetic waves where the field intensity is maximum can be addressed individually to tune optical mode.

Figure 2.9 shows the normalized electric field distribution and the normalized amplitude of the displacement field associated with the localized optical and acoustic modes. The regions highlighted with green boxes indicate areas of maximum mode amplitude within the mode volume, making them good candidates for surface oxidation to selectively tune the optical and acoustic modes. A numerical analysis of the sensitivity and selectivity of the OMCs is presented in the following section.

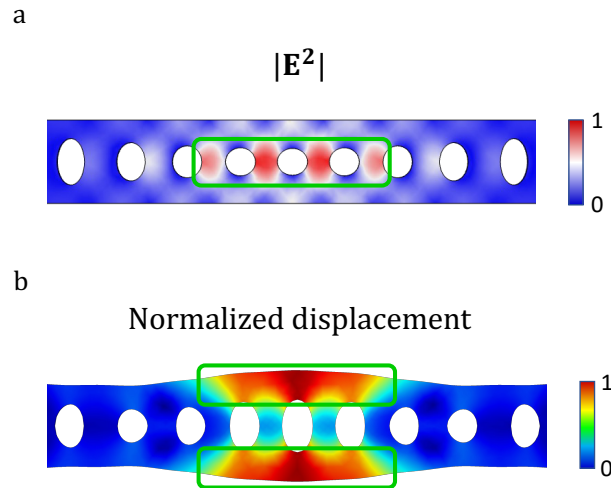


Figure 2.9: **Normalized optical and acoustic mode shapes of OMC.** **a)** Normalized electric field intensity profile of the optical mode. Candidate region for the optics focused oxidation is outlined in green. **b)** Normalized displacement magnitude profile of the acoustic breathing mode. Candidate acoustics-focused oxidation regions are outlined in green.

Pixel-by-pixel oxidation simulations

To test the optimal oxidation locations on OMCs, a Finite Element Method simulation is setup using COMSOL Multiphysics. The simulation aims to identify areas on the OMC surface that are sensitive to perturbation due to the local field concentrations. A simple 1D OMC geometry similar to what was used for imperfection analysis in Chapter 2 is selected as the starting point of the analysis. As opposed to the imperfection analysis where every hole on the OMC nanobeam is unique in position and size, for this particular test, symmetric boundary conditions are used on x and y axes to cut down the computational cost. Z axis symmetry is not applicable since we study the effect of the oxide patches only on the top surface of the structure. The simulation pipeline is as follows:

1. Create a grid on the quarter OMC surface with an x-y pitch of d_{px} . Define center coordinates of the pixels.
2. Define 2 stacked regions (oxide pixel) separated by the OMC top surface at the designated center pixel location. This is a very crucial step because the optical and mechanical frequency shifts we are expecting are comparable to that of the perturbation introduced by the different meshing conditions.

Created regions are meshed identically for both reference (where there is no oxide patch) and perturbed (with oxide patch) cases.

3. Assign materials as silicon and air for lower and upper regions for the reference run.
4. Run optical and mechanical eigenfrequency analysis for the reference case.
5. Store the optical and mechanical mode data for the reference case. Optomechanical coupling calculated using optical mode field and the mechanical modes obtained from the analysis is used for identifying the mechanical eigenmode of interest. The mode of interest is defined as the mechanical mode with the maximum optomechanical coupling rate g_{OM} .
6. Assign materials as silicon oxide for both lower and upper regions for the perturbed case.
7. Run optical and mechanical eigenfrequency analysis for the perturbed case.
8. Compare the optical and mechanical mode data with the reference case to extract the frequency shifts.
9. Repeat 2-8 for every defined pixel coordinate to create a shift map for optical and mechanical frequencies. Based on the oxidation characterization made on silicon substrate (presented in Chapter 2), an oxide pixel in this test is defined as a 25nm by 25nm square with a thickness of 3.2nm over the surface. An oxide layer with a thickness of 2.25nm ($\sim 70\%$ of 3.2nm) is created under the surface.

Simulation results, shown in Figure 2.10, suggest that the maximum optical wavelength shift is observed for the oxide patches located along the longitudinal axis of the OMC. The shift amount decays from the longitudinal line towards the edges of the nanobeam. It is also possible to see that the shift is maximal around the center hole, and it decays going farther away from the center towards the ends of the nanobeam. Maximum acoustic mode frequency shift is observed on the edges of the nanobeam around the center region. Frequency shift decays going from the center towards the ends of the beam.

Simulated optical resonance shifts are in good spatial agreement with electromagnetic field amplitude of the mode while mechanical frequency shift follows the

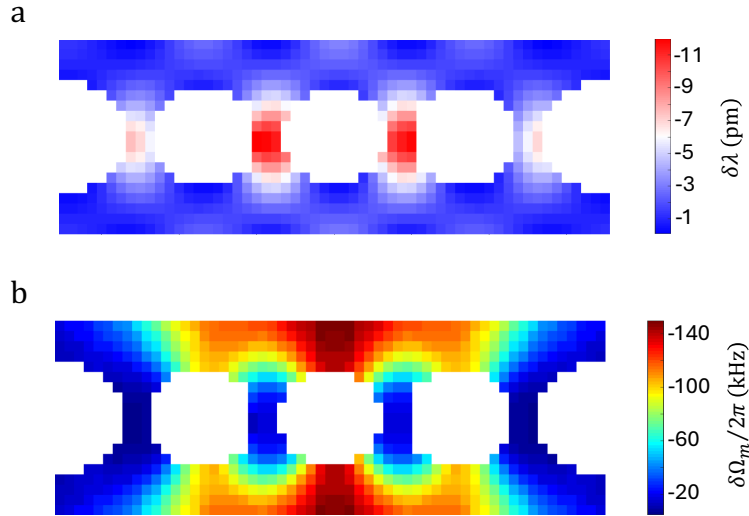


Figure 2.10: **Pixel by pixel optical and acoustic mode shifts.** **a)** Optical mode wavelength shift $\delta\lambda$ and **b)** acoustic mode frequency shift $\delta\Omega_m/2\pi$ simulated as a function of the location of the oxide pixel. Oxide pixels used in this analysis are $25nm$ by $25nm$ square pixels with a thickness of $3.2nm$.

displacement amplitude of the breathing mode. Results suggest that the optical and acoustic modes are most sensitive to local alterations on the OMC surface when the respective local field amplitude is higher since the mode participation of the altered volume is higher at those locations.

The goal of this method is to tune both optical and acoustic resonances independently which are very densely confined in the same nanometer scale mode volume. This means a perturbation introduced at a given location shifts both the resonances although with different weights. We define a metric, selectivity, based on the normalized proportional contributions of the perturbations to a given mode. For example, optical selectivity is the normalized optical frequency shift for a given oxide pixel divided by the normalized acoustic frequency shift induced by the same oxide pixel at the same location. This metric quantifies the spatial isolation of a given mode shift in response to the local perturbation introduced by the nano-oxidation and it gains importance when we want to fine tune optical (acoustic) mode without perturbing the acoustic (optical) mode.

Based on the results of the pixel-by-pixel oxidation simulations presented in Figure 2.10, optical (S_o) and acoustic (S_m) selectivity values are plotted in Figure 2.11, using following relations.

$$S_{o,ij} = \frac{\delta\lambda_{ij}}{\delta\Omega_{m,ij}} \frac{\max(\delta\Omega_m)}{\max(\delta\lambda)} \quad (2.3)$$

$$S_{m,ij} = \frac{\delta\Omega_{m,ij}}{\delta\lambda_{ij}} \frac{\max(\delta\lambda)}{\max(\delta\Omega_m)} \quad (2.4)$$

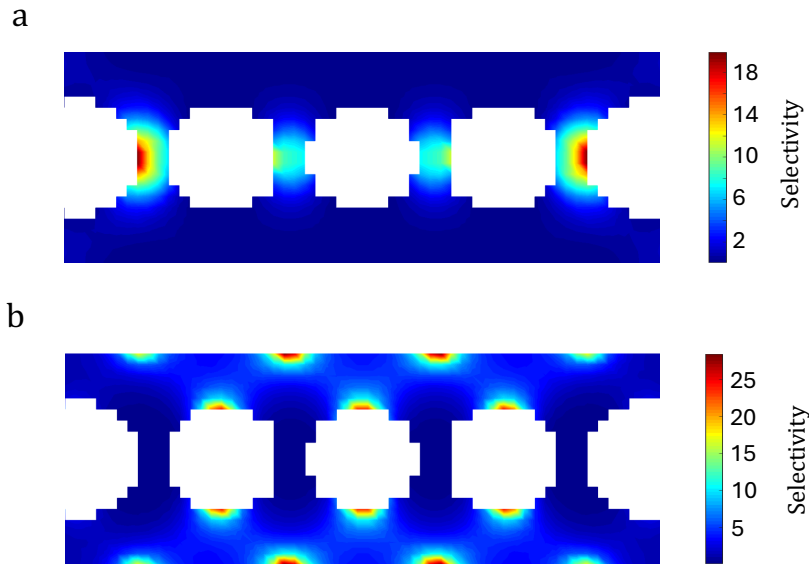


Figure 2.11: **Optical and acoustic selectivity map.** **a)** Interpolated normalized optical selectivity, S_o and **b)** interpolated normalized acoustic selectivity, S_m . The normalization is performed with respect to the maximum shifts obtained in the pixel-by-pixel oxidation profiles in Figure 2.10

In the light of the simulations presented in this section, one should target the areas in between elliptical holes and confine the oxide patterns around the longitudinal center line. On the other hand, acoustic frequency must be targeted at the edges of the nanobeam, closer to the center hole to obtain the maximum mode tuning. Optical tuning can be achieved with a relatively high selectivity as long as the pattern is confined around the center longitudinal line. Adversely, patterns targeting high acoustic frequency shift have very little overlap with the high acoustic selectivity regions which poses a risk of interfering with the optical mode which makes the isolated tuning harder for the acoustic mode.

2.6 In situ nano-oxidation setup

To enable realtime in situ nano-oxidation, a Park Systems N10 Atomic Force Microscope with an integrated dimpled fiber optical probing setup is built. System comprises two sub-parts that are independently controlled during operation.

Optical probing setup

Optical probing setup consists of a tunable laser (TLB 6700), a wavemeter for the precise control of the laser wavelength, an attenuator to control the incident laser power that reaches the device, a circulator to enable the reflection measurements, a dimple fiber and positioner stages (Suruga Seiki) to facilitate the fiber-device coupling, and finally a set of photodetectors for the detection of the reflection signal. Details on the dimpled fiber taper coupling technique can be found in Refs [60, 61]. The dimpled fiber is controlled by a three-axes motorized positioning stage and two manual rotational stages. Two different photodetectors are used to measure the reflection signal, one 'slow' detector for optical mode probing which is directly connected to a DAQ card and a 'fast' detector for GHz level mechanical mode probing that is readout using a Spectrum Analyzer (RS FSV).

AFM setup

AFM setup, shown in Figure 2.12, comprises of a Park Systems N10 AFM and an enclosure to isolate the system from external conditions. Electrically grounded AFM sample stage is equipped with motorized 2 axes positioners to manipulate the sample position, and a high precision z-axis positioner for the cantilever which is driven with a feedback loop. AFM is also equipped with a microscope to optically monitor the sample while the manipulations and measurements are being performed. AFM enclosure is equipped with custom temperature and humidity sensors to keep track of the environmental conditions. The entire system sits on an optical table stabilized with active vibration isolation.

The AFM setup is controlled with a coding-based control software provided by Park Systems. A custom designed code generation software is used to make the conversion between the desired oxidation patterns and the machine-readable script. Oxidation patterns are created with the MATLAB based custom GUI and converted into .js files to be read by the Park System software which then controls the sample stage, cantilever z-motor and the voltage source to apply voltage on the AFM cantilever tip.

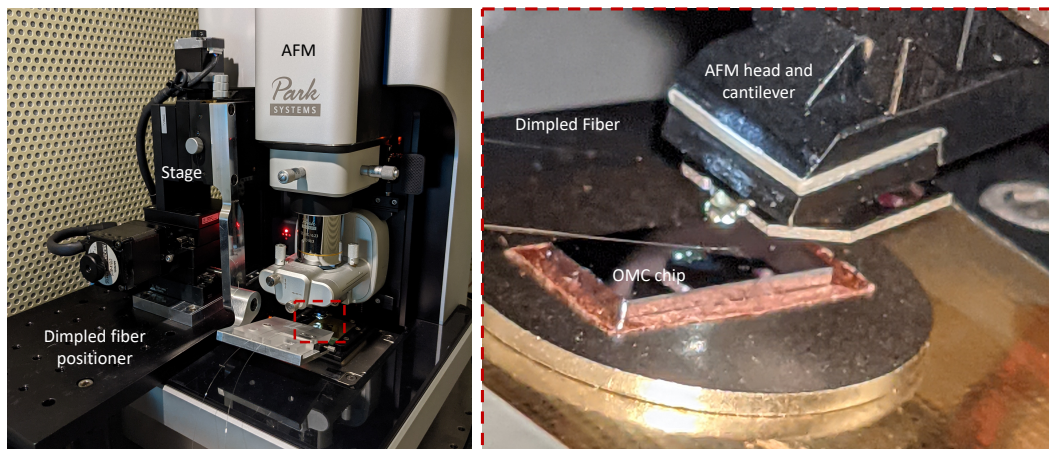


Figure 2.12: **AFM with integrated optical testing setup.** An AFM equipped with a dimple fiber attached at a 3-axis positioner stage. On the right, a close up of the sample stage where AFM cantilever, optical dimple coupler and the sample is shown.

2.7 Experimental characterization of nano-oxidation induced mode shifts

Among the two AFM operation modes presented and characterized in this chapter, contact mode and tapping mode, tapping mode is selected for the simultaneous mode tuning experiments. There are two main reasons to motivate this decision, gentleness and the higher precision of the tapping mode. During the bare silicon oxidation tests, we always worked on the silicon device layer of the SOI sample where the top silicon layer was always attached to the bulk supported by the buried oxide layer underneath. This allowed us to use arbitrarily high forces. However, as a post fabrication tuning technique, nano-oxidation must be applied on the suspended structures which are not structurally supported by the bulk. Our OMCs are doubly clamped beams that are approximately $11\mu\text{m}$ long, 220nm thick and 510nm wide. This poses a big constraint on the maximum applicable force by the AFM tip since any excess force can damage the delicate OMC structure. Typical forces exerted on the sample during a contact mode AFM scan can range from 100pN to 100nN . Although on the order of 100pN force exerted on the OMC does not create a large enough stress on OMCs to cause plastic deformation, it is safer to utilize tapping mode where the AFM tip-OMC contact is minimal. Secondly, tapping mode can create smaller oxide features compared to the contact mode thanks to the thinner water meniscus created between the tip and the surface. Spatial accuracy of the oxidation plays a big role when we aim to target mode shapes precisely, hence the tapping mode suits better for this application.

Nano-oxidation parameters are selected based on the characterization done on the bare silicon using tapping mode. As discussed earlier in Section 2.3, properties and dimensions of the oxide features can be tuned using multiple parameters such as AFM set point³, scan speed, tip voltage, ambient humidity and temperature. For the simplification of the parameter space, 2 distinct oxidation modes⁴ are selected: mild and aggressive oxidation. In each mode, ambient conditions and the voltage applied kept constant. For mild oxidation mode, scan speed of 100nm/s and set point of 15nm is used with an expected oxide thickness of 1.2nm whereas in aggressive tuning mode, scan speed and set point of 50nm/s and 5nm is used, which results in 2.5nm thick oxide lines. In either mode, line width is approximately 25nm. In order to obtain uniform patches with oxide lines, we used a raster scan pattern with a pitch of 13nm which results in final oxide thickness of approximately 1.6nm and 3.2nm, respectively, for the mild and aggressive oxidation.

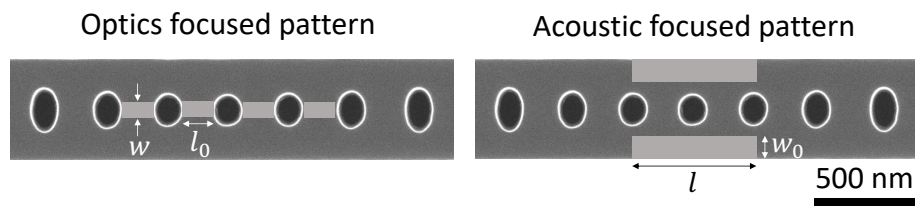


Figure 2.13: **Optics and acoustic focused patterns** Patterns designed to target optical and acoustic modes. For the optics focused pattern, the length and the positions of the rectangular patterns are fixed while the width is varied. For the acoustic mode focused pattern, the width and the pattern positions are kept fixed while the length is varied. Patterns are designed to target high sensitivity and high selectivity regions for each mode.

From the simulated pixel-by-pixel oxidation maps, we identified 2 simplified oxidation patterns to target the optical and acoustic resonances. For the optical resonance tuning we chose to utilize four rectangular patterns located between holes L2 to R2 with fixed length $l_0 = 170nm$ and a variable width w . The optics targeting patterns coincide with the longitudinal axis of the OMC nanobeam (see Figure 2.14). For the acoustic resonance tuning, we chose to use rectangular slabs with a constant width $w_0 = 120nm$ and a variable length l . Acoustic targeting patterns are located on the edges of the OMC, centered at the transverse symmetry axis of the OMC (see Figure

³This can mean a number of things based on the AFM mode being used. It refers to the contact force for the contact mode and the oscillation amplitude for the tapping mode.

⁴One should not confuse the oxidation modes with the AFM operation modes. Modes that are mentioned in this section only refer to the intensity of the tapping mode oxidation which emerges as the oxidation thickness.

2.13). The free parameter is swept for optics and acoustic targeting patterns for mild and aggressive oxidation modes while optical and acoustic modes are probed in real time. A simple schematic showing the setup and techniques used for the patterning and probing the OMCs is given in Figure 2.14.

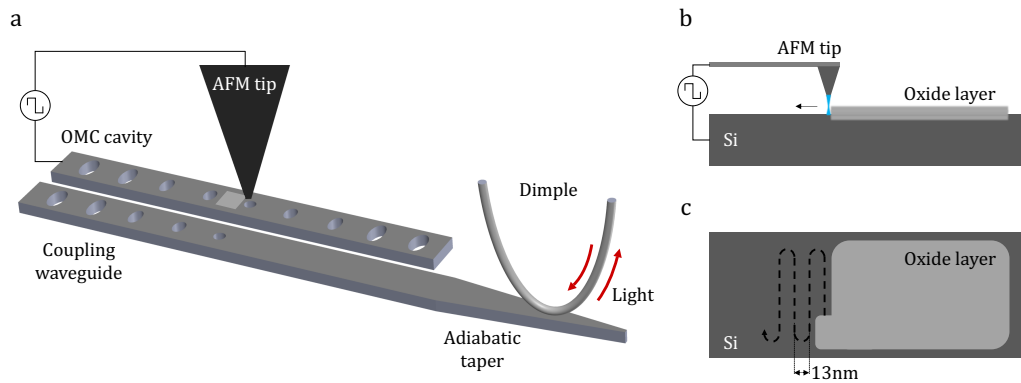


Figure 2.14: **In situ-nano-oxidation schematic.** **a)** Symbolic demonstration of the integrated in situ nano-oxidation setup. AFM tip is biased with an alternating square voltage signal while the sample is grounded. Dimple fiber is used to couple light into the OMC through the adiabatic taper coupler. **b)** The schematic of the oxidation process. AFM tip is moved over the surface while the bias voltage induces local oxidation of the surface. **c)** Raster scan with a pitch of 13nm used during the tuning experiments to create smooth oxide patches.

Designated patterns are applied on the OMCs and both optical and acoustic resonances are measured for each increment. Experimental procedure for the tuning characterization is as follows:

1. Locate the OMC of interest using the built-in AFM camera and sample stage and touch down the dimpled fiber on the adiabatically tapered coupler.
2. Measure the reference optical and acoustic spectrum to set the baseline.
3. Locate the center hole of the OMC of interest and fix the software origin at the center hole coordinates. All the precise localization of the OMC are done using non-contact mode AFM scans. OMCs used in this experiment have an indicator/marker placed at a known distance from the center ellipse of the OMC to facilitate finding the OMC center coordinates with minimal perturbation given to the OMC by the AFM scans prior to the oxidation tuning.
4. Apply the first set of patterns. Defined patterns are applied with the previously described techniques and the respective oxidation parameters

5. Measure the post-tuning optical and acoustic resonances. Optical resonance is measured by sweeping the laser wavelength within a 200pm range using a piezo element embedded in the laser, controlled by the DAC card outputs. Laser output wavelength is monitored with the wavemeter on the path. Obtained resonance dip is fitted with a Lorentzian to precisely find the resonance wavelength and loss rates. Acoustic frequency is measured with a blue detuned laser parked ω_m away from the resonance center wavelength. Reflection is detected by a nanosecond detector on the path and the power spectral density (PSD) is measured from the electrical output of the detector by a spectrum analyzer. Obtained resonance peak is fitted to a Lorentzian to measure the corresponding resonance frequency and linewidth.
6. Enlarge the pattern by oxidizing the incremental strips. Patterns are applied starting from the smallest free parameter dimension and oxide lines are added to increase the free parameter dimension incrementally after every measurement.
7. Measure the post-tuning optical and acoustic resonances.
8. Repeat steps 6 and 7.
9. Repeat steps 1-8 for optics targeting pattern and acoustic targeting pattern, on five OMCs each.
10. Repeat steps 1-9 for mild and aggressive oxidation modes on five OMCs each.

Measured tuned resonance properties are subtracted from the reference data taken at the initial state of the OMCs to obtain the change due to the incremental oxidation. Results are plotted for each type of pattern and both optical (blue) and acoustic (red) resonances in the Figure 2.15.

Dashed lines represent the simulated wavelength and frequency shifts for the same patterns applied in the experiment. Simulation steps are identical to the Section 2.5 where pixel-by-pixel oxidation simulations were presented previously. The exact material properties of the created oxide are process specific and differ from the literature values of bulk Silicon Oxide compounds. By matching the experimental data to the simulated resonance frequency shift trends, we found that the density, Young's modulus and relative permittivity of oxide grown with our process are $3500\text{kg}/\text{m}^3$, 70 GPa and 2, respectively. Material properties of the oxide layers

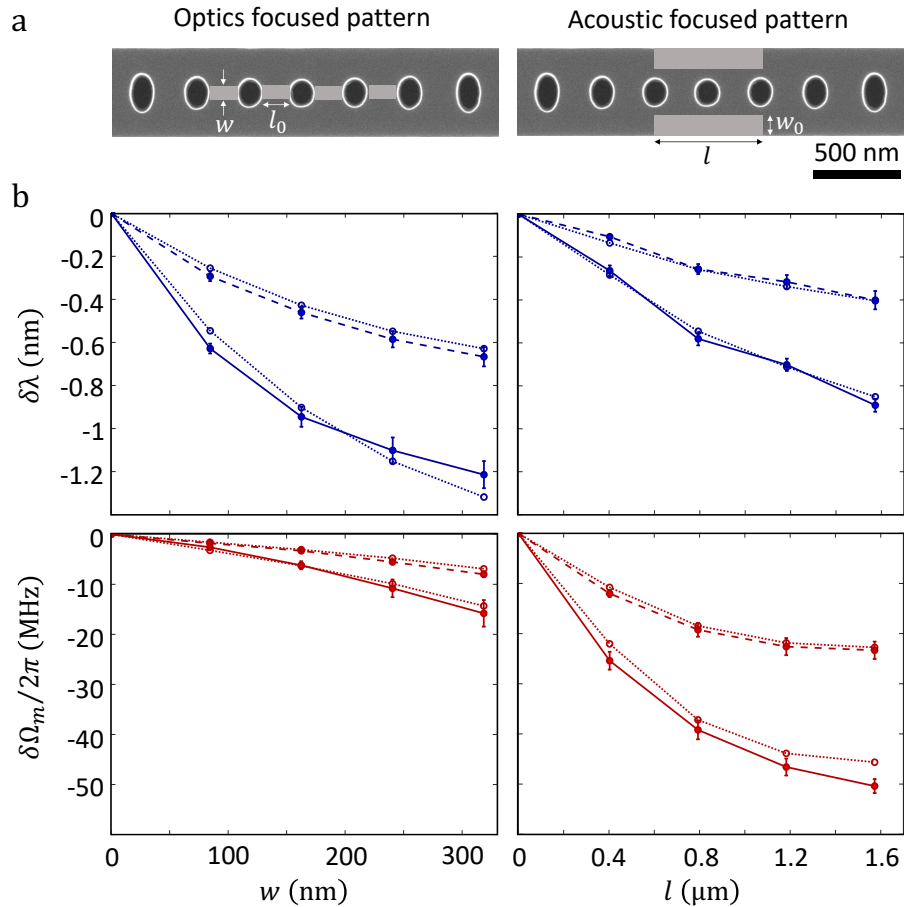


Figure 2.15: Optical and acoustic mode shifts with changing pattern dimensions. **a)** Optics and acoustic focused patterns. **b)** Tuning of optical and acoustic resonances as a function of the size of the respective oxidation patterns. Optical wavelength shift $\delta\lambda$ with respect to width w of the optics focused pattern (top left) and length l of the acoustic focused pattern (top right). Acoustic frequency shift $\delta\Omega_m$ with respect to width w of the optics focused pattern (bottom left) and length l of the acoustic focused pattern (bottom right). Solid (dashed) lines represent data taken for aggressive (mild) oxidation. Dotted lines show simulated values from finite element method simulations. Error bars represent the standard deviation across five OMC cavities measured for each dataset.

grown with AFM nano-oxidation technique are specific to the oxidation process and differ from the literature values for the bulk SiO_2 . In the acoustic simulations, we use the anisotropic elasticity tensor of silicon with $(C_{11}, C_{12}, C_{44}) = (166, 64, 80)$ GPa and assume a $[110]$ crystallographic orientation for the x-axis (longitudinal axis of the beam).

For the optics-focused pattern, increasing w significantly reduces the optical wave-

length while causing a smaller reduction in acoustic frequency. In contrast, for the acoustics-focused pattern, increasing l decreases the acoustic frequency due to the increase in motional mass ($\Omega_m \propto \sqrt{1/m}$) and reduces the optical wavelength by lowering the effective refractive index. Aggressive oxidation at $w = 320\text{nm}$ results in a blue shift of more than 1.2nm in the optical wavelength, whereas aggressive oxidation at $l = 1.6\mu\text{m}$ leads to a reduction of over 50 MHz in acoustic frequency. Each data point represents the average and standard deviation obtained from five devices. For each device, the patterns were applied cumulatively, starting from the center and progressively adding more oxide to increase either w or l at each step.

2.8 Effect of nano-oxidation on the intrinsic optical scattering rate

Nano-oxidation process alters the OMC surface and converts a thin layer of silicon on the OMC surface into amorphous silicon oxide besides increasing the roughness of the surface. The oxide compounds created with the nano-oxidation process are not very pure and as orderly as single crystalline silicon. Especially on the regions where high electric field is localized, created impurities and higher surface roughness lead to emergence of additional scattering sites which impacts the intrinsic optical scattering rate. Figure 2.16 shows the change in intrinsic loss rate $\kappa_i/2\pi$ of the optical mode with respect to the oxide patterns created in the tuning characterization measurements. Data suggests that thicker and larger oxide patches lead higher added optical scattering losses.

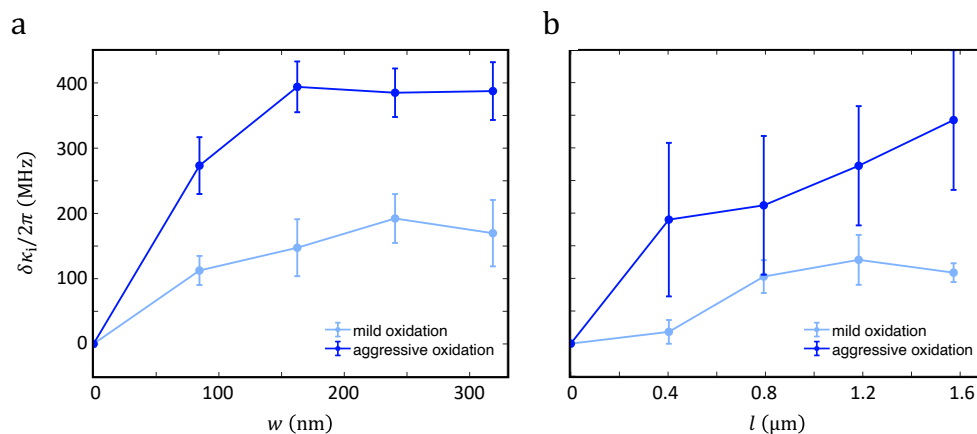


Figure 2.16: **Change in intrinsic optical scattering rate.** Change in intrinsic optical scattering rate $\kappa_i/2\pi$ with respect to the **a)** width w of the optics focused oxidation pattern, and **b)** length l of the acoustic focused pattern. Data is obtained in both mild and aggressive oxidation modes. Error bars represent the standard deviation measured across five OMCs.

To minimize oxidation-induced degradation of optical quality factors, it is preferable to use smaller and thinner patterns, provided they still allow the required mode shift. Additionally, if higher scattering losses are unacceptable, the oxide patches can be removed using a Hydrofluoric Acid etch. This approach not only eliminates the oxide but also has the potential to enhance resonance shifts further, as the vacuum refractive index is lower than that of the SiO_x formed on the surface.

2.9 Pattern generation algorithm based on empirical shift data

Optical wavelength and acoustic frequency shifts presented in Chapter 2.7 shows that selected simplified patterns can be consistently used to tune OMC resonances. However, the data also shows that there is unwanted cross coupling between optics (acoustic) targeting patterns and the acoustic (optical) resonances. Even in the case we oxidize highly optically selective areas, it is possible to observe acoustic frequency shifts along with high optical wavelength shifts. One should take both resonance shifts into account while identifying the oxidation patterns required in order to achieve predictable simultaneous tuning.

To enable simultaneous tuning with the simplified patterns, we developed a pattern generation algorithm that is based on the previously studied wavelength/frequency shift data. Four independent pair of shift matrices are formed using four independent oxidation mode combinations as follows.

1. Optics targeting patterns with mild oxidation + acoustic targeting patterns with mild oxidation (First row of Figure 2.17).
2. Optics targeting patterns with mild oxidation + acoustic targeting patterns with aggressive oxidation (Second row of Figure 2.17).
3. Optics targeting patterns with aggressive oxidation + acoustic targeting patterns with mild oxidation (First row of Figure 2.18).
4. Optics targeting patterns with aggressive oxidation + acoustic targeting patterns with aggressive oxidation (Second row of Figure 2.18).

Each shift matrix is created by interpolating the respective wavelength/frequency shift data. Matrices contain a wavelength or an acoustic frequency shift data for a given point that corresponds to a width parameter and a length parameter for optics and acoustic targeting patterns, respectively. One can find a suitable pattern

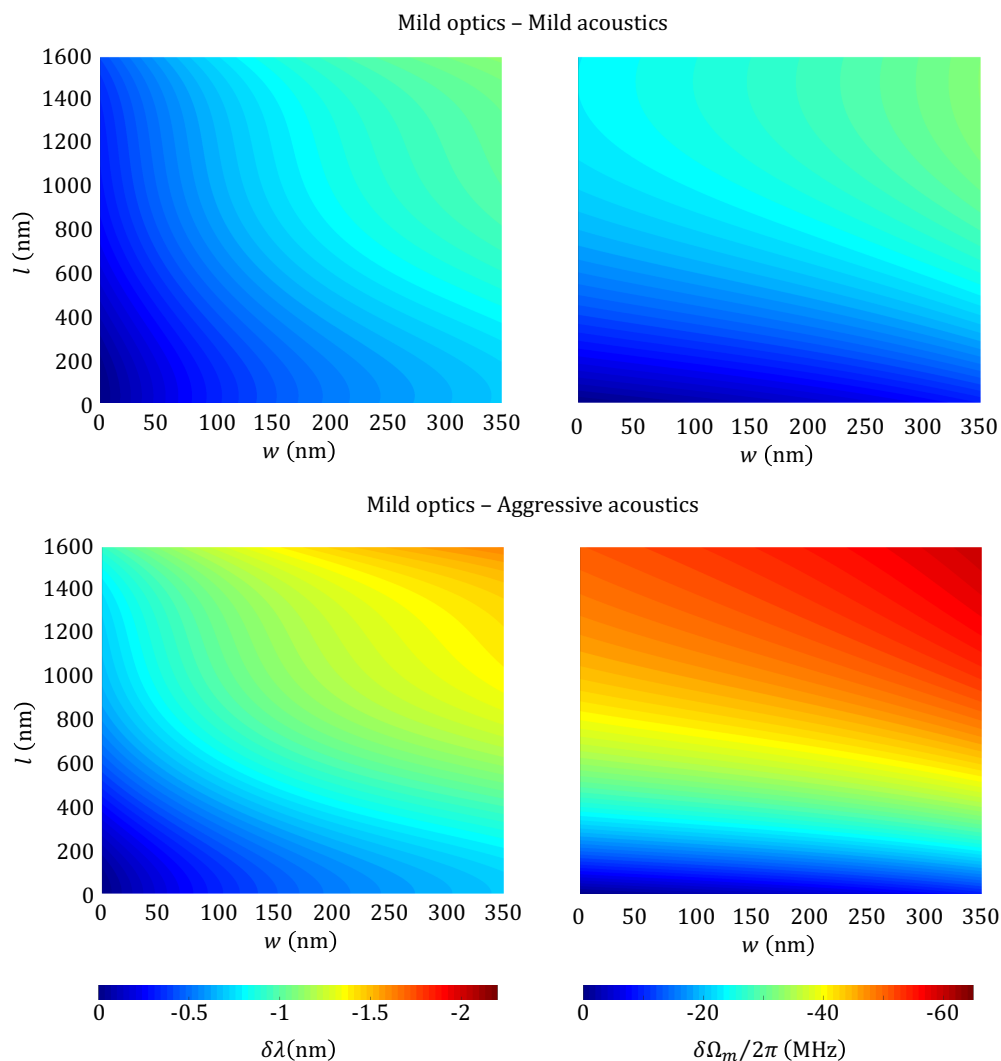


Figure 2.17: **Shift matrices with mild optics targeting oxidation.** 2 pairs of shift matrices made for mild optics-mild acoustic and mild optics-aggressive acoustic targeting oxidation. Presented data is derived from the coarse tuning characterization experiments by spline interpolation. Left (right) column shows the optical wavelength (acoustic frequency) shift with respect to the combined pattern dimensions.

for any given scenario within the tuning range in at least one of the shift matrices. The pattern generation algorithm accepts two inputs, desired optical and acoustic resonance shifts. The curves that correspond to the desired optical and acoustic resonance shifts are identified in each matrix. The required oxide pattern dimensions and corresponding oxidation mode can be found at the intersection point of these curves coming from mutual shift matrices. An example case is demonstrated in

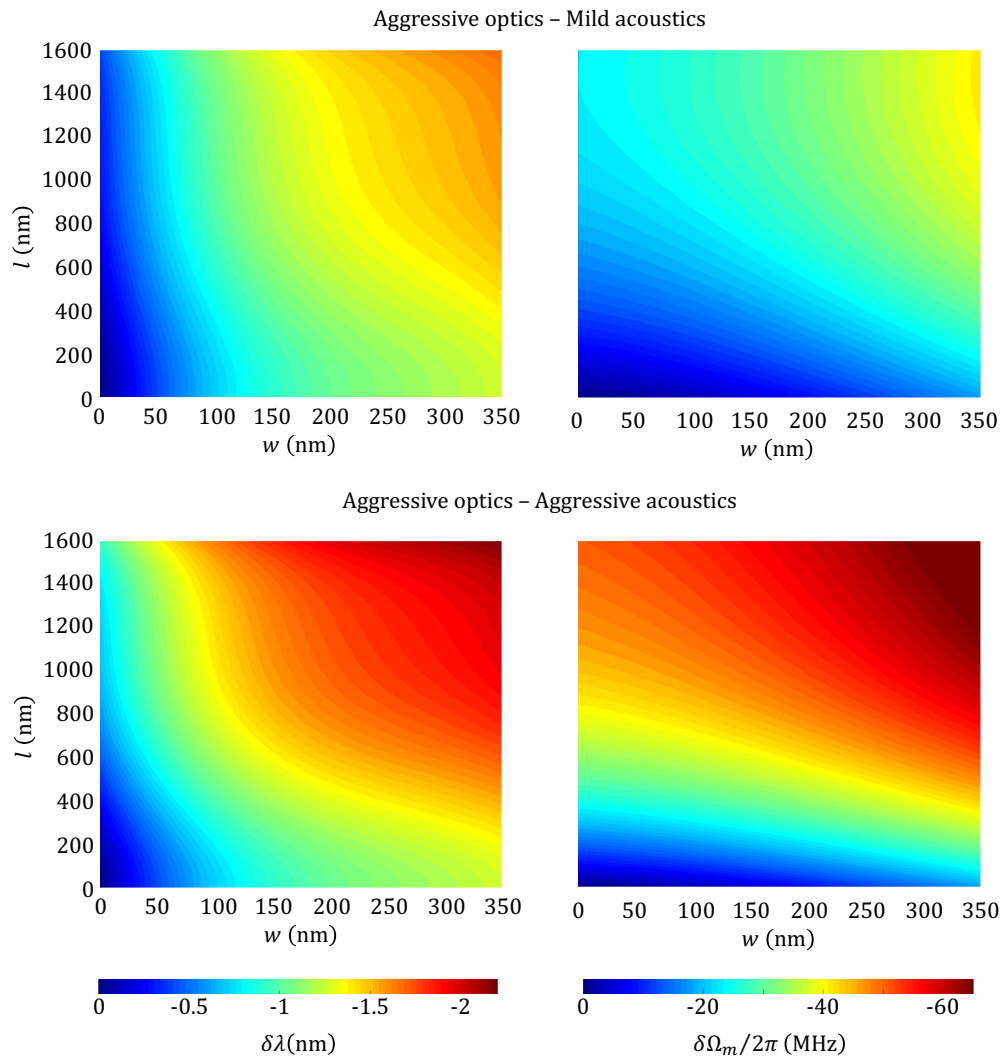


Figure 2.18: **Shift matrices with aggressive optics targeting oxidation.** 2 pairs of shift matrices made for aggressive optics-mild acoustic and aggressive optics-aggressive acoustic targeting oxidation. Presented data is derived from the coarse tuning characterization experiments by spline interpolation. Left (right) column shows the optical wavelength (acoustic frequency) shift with respect to the combined pattern dimensions.

Figure 2.19, where the input optical and acoustic resonance shifts are selected as 1.4nm and 45MHz, respectively. In the shift matrix pair for aggressive optics-aggressive acoustic case, curves that correspond to the desired resonance shifts are shown with dashed line. Finally, the joint pattern dimensions are found at the intersection of these two curves, as shown in Figure 2.19c.

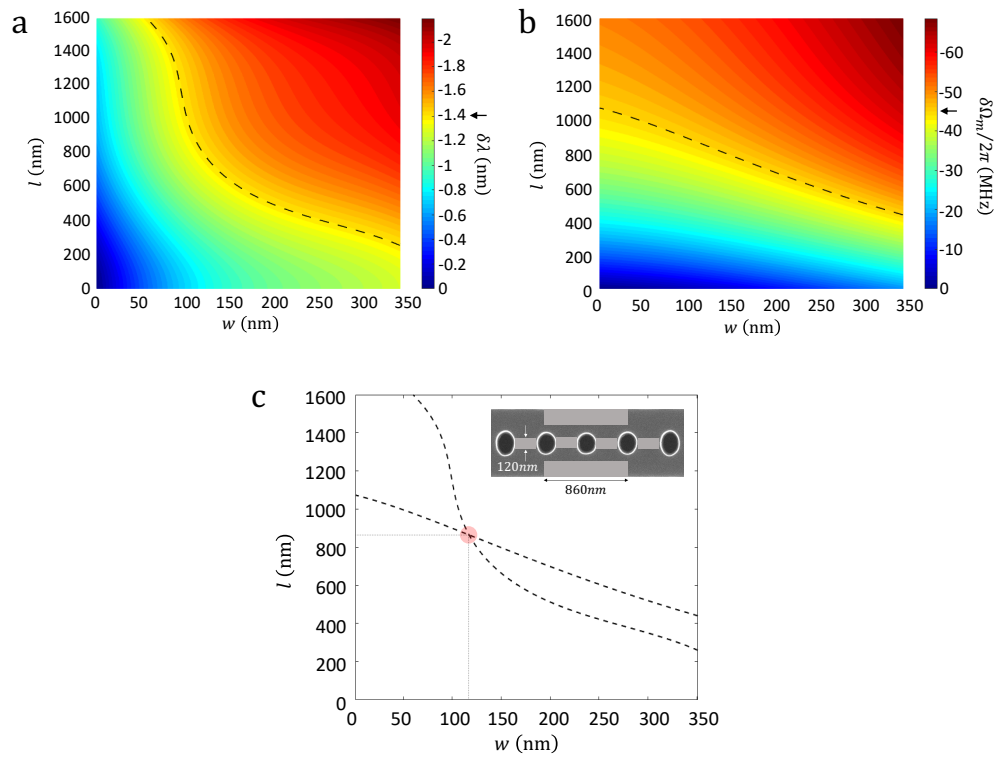


Figure 2.19: **Optimal tuning pattern finding algorithm.** An example case where a combined pattern is sought for an optical shift of $\delta\lambda = 1.4$ nm and an acoustic shift of $\delta\Omega_m = 45$ MHz. Panels **a** and **b** show the mode shifts with respect to pattern dimensions for the aggressive optics–aggressive acoustic case. Dashed lines indicate the target optical wavelength shift of $\delta\lambda = 1.4$ nm and acoustic frequency shift of $\delta\Omega_m = 45$ MHz. **c**) Intersection of the optical and acoustic mode shifts in the pattern dimension parameter space. The pattern dimensions at the intersection, $w \approx 120$ nm and $l \approx 860$ nm, yield the required optical and acoustic mode tuning.

A combination of optical and acoustic shift request can be met by multiple combinations of different oxidation patterns. Algorithm picks the best pattern by trying to minimize estimated increase in the intrinsic optical scattering rate and trying to minimize the oxidation duration where the first criteria is prioritized. This usually means that milder oxidation scenarios are preferred over the aggressive scenarios as long as required shift is not high.

This algorithm is meant to be used for rough tuning of the modes as the shifts obtained with simplified patterns cannot provide the high-level accuracy needed to tune resonances within respective resonance linewidths. We need fine tuning of the modes with greater granularity to achieve required tuning accuracy.

2.10 Fine tuning methods

So far, we focused on the tuning ranges needed to achieve to obtain the desired mode matching between different OMCs for both optical and mechanical resonances. Even though this is a big step towards rough alignment of the modes, a finer tuning method with high isolation that can provide more controllable shifts less than respective linewidths of the tuned resonant modes. There are two approaches that can potentially be capable of achieving desired precision: (i) use of pixel-by-pixel oxidation near the mode volume, guided by the selectivity and shift maps and (ii) using multiple pixel oxidation away from the mode volume.

First approach is advantageous for fast adjustments with real-time feedback. Since we use single pixels at a time, significant increase in the scattering rate is not expected. Fine tuning is expected to be performed following the rough alignment, which means the mode volume will be pre-oxidized during the fine tuning. This can be considered as a handicap of this method since the existing oxide layer can distort the oxidation process or alter the expected oxidation parameters due to the increased penetration depth for the oxyanions introduced by applied tip voltage. Second approach does not suffer from the existing oxide layer thereby it is easier to predictably oxidize the surface. However, the modes are very localized in the center of the cavity region and the electric field energy density and the mechanical displacement of the resonant modes decay very fast farther from the center hence one needs a bigger perturbation to achieve desired shifts. A big perturbation closer to the mirror or waveguide ellipses can have serious side effects such as shift or shrinkage of the optical and mechanical band gaps or the change in acoustic mode hybridization in the case of 1D OMC transducers where the OMC acoustic mode is hybridized with another acoustic mode outside the nanobeam. For the given reasons, first approach will be adopted for the rest of the chapter for fine tuning purposes.

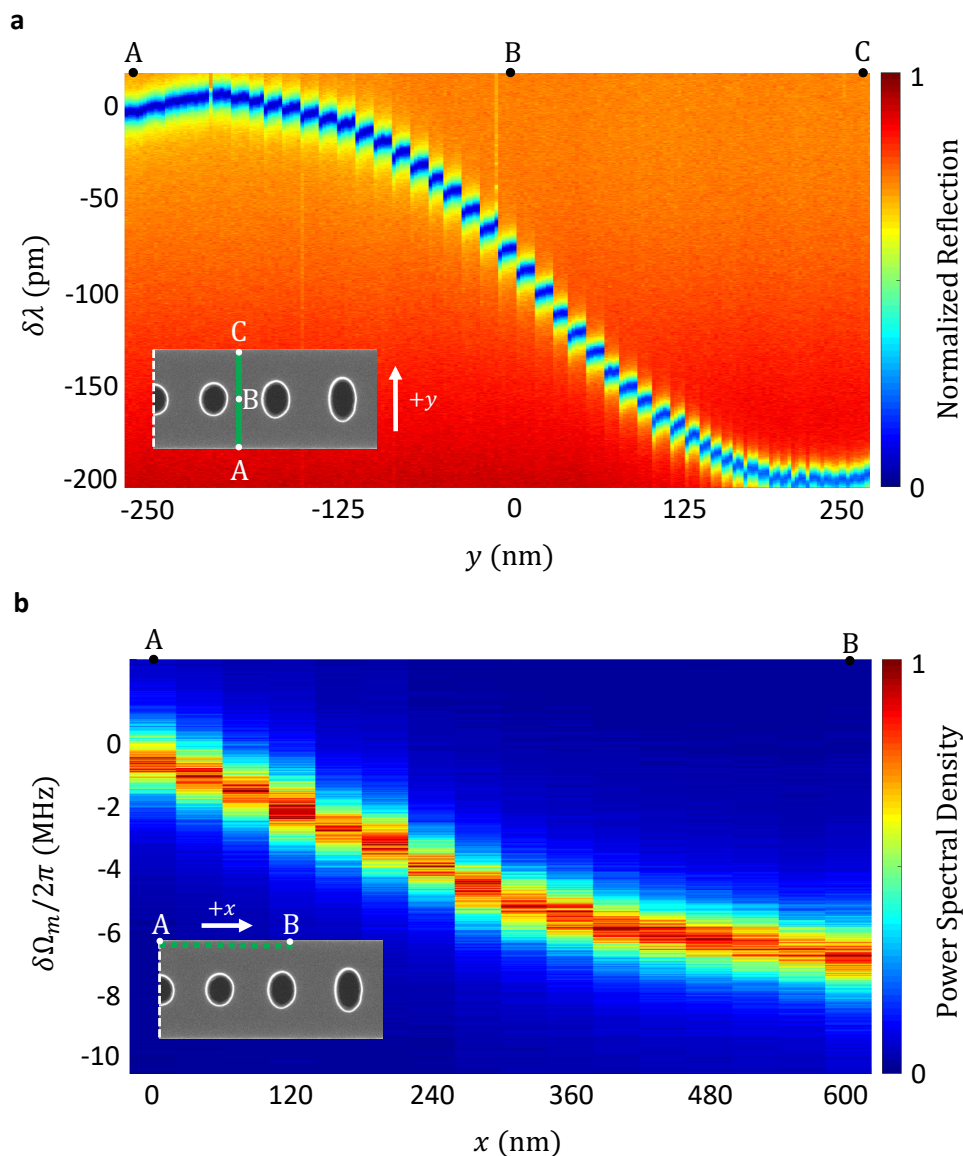


Figure 2.20: **Real-time, in situ monitoring of the oxidation process.** **a)** Real-time spectra showing optical resonance tuning during sequential application of the oxidation pattern. As illustrated in the inset, the pattern is applied sequentially from point A to point C, one pixel at a time. AFM tip locations during the experiment are indicated at the top of the plot with letters A, B, and C, corresponding to the points labeled in the inset image. Discontinuities along the horizontal axis arise from proximity effects between the AFM tip and the OMC cavity during the oxidation sequence. **b)** Real-time data showing the acoustic frequency shift during pixel-wise oxidation. Oxide pixels are applied on the surface starting from point A to point B, as indicated in the inset.

To characterize the mode shifts due to pixelwise oxidation, two measurements were made targeting optical and acoustic modes. In the first measurement, pixel-by-pixel oxidation is applied along the transverse axis of the nano beam from point A to point C with a pitch of 13nm, as seen in Figure 2.20a. Optical spectrum is measured after oxidation of every pixel. For the acoustic targeting measurement, pixel-by-pixel oxidation performed along a line located on the edge of the nano-beam with a pitch of 40nm, starting from the center point (shown as point A) until the point B. Acoustic spectra is measured after every pixel that is oxidized. The data shows that 1pm/px optical fine tuning precision and 150kHz/px acoustic mode tuning is possible within the mode volume, at the points away from the most sensitive regions. Resonance shift data is in good agreement with the electric field distribution and the displacement amplitude of the modes along the chosen lines (see Figure 2.20b).

2.11 Simultaneous optical and acoustic mode tuning of OMCs

AFM nano-oxidation technique and its potential to alter OMC resonance frequencies were studied in the previous sections. Here, a proof of concept demonstration of tuning of multiple OMCs using our technique is presented.

To achieve simultaneous optical and acoustic tuning we used a two-step algorithm that consists of a rough alignment step followed by real-time fine-tuning steps. The rough alignment step employs the previously introduced pattern generation algorithm to generate optimal joint patterns. Once the wavelength and frequency dispersion of the OMCs are acceptably low, pixel-by-pixel oxidation is used to simultaneously fine-tune the modes into the same target wavelength and frequency. Tuning is finalized when detuning requirements are met.

$$\max(\Delta_\lambda) < \min(\kappa) \quad \& \quad \max(\Delta_f) < \min(\gamma) \quad (2.5)$$

Three OMCs with an initial optical wavelength spread of <1nm and acoustic frequency spread of <30MHz are preselected imposed by the limitations of our tuning technique. In principle it is possible to achieve optical wavelength and acoustic frequency shifts greater than 2nm and 60MHz, respectively. However, simultaneously tuning both resonances limits the tuning range of individual modes due to the use of larger patterns which coincide with poor selectivity regions on the OMC hence isolating the modes cannot be trivial when large resonance shifts are needed. A possible solution is targeting an offset acoustic frequency value to tune into, that is much lower than all the initial acoustic frequencies. This way one can tune distant

optical resonances while still being able to tune the acoustic mode, although the matching frequency would be far from the initial frequencies.

Coarse tuning of OMCs using pattern generation algorithm

First step to coarsely align OMCs is selecting a feasible target optical wavelength and acoustic frequency. There is a constraint when choosing targets, target optical wavelength (acoustic frequency) cannot be larger or equal to any of the initial wavelengths (frequencies) as long as required acoustic frequency shift (wavelength shift) is larger than or on the order of an acoustic (optical) resonance linewidth. OMCs that are manipulated by the nano-oxidation method blue-shift in optical wavelength due to the non-zero local optical selectivity parameter thereby there is no solution for a pattern that only tunes the acoustic frequency in our parameter space. Only exception to this rule is the case where required acoustic tuning is much less than the respective linewidth in which case a very small oxidation pattern can be applied at the most acoustically selective regions which would shift the optical wavelength negligibly. However, even in this rare situation, one should target for a slightly lower wavelength to account for a possible overshooting. Secondly, in a given set of optical and acoustic resonances, highest wavelength and acoustic frequency do not necessarily belong to the same OMC. Moreover, this is less likely to be the case since OMCs with lower optical wavelengths tend to have higher acoustic frequencies since lower optical wavelength translates into reduced silicon in the mode volume which leads to a lower effective mass hence higher acoustic frequency for the same breathing mode.

For the three OMCs selected for this experiment, target wavelength and frequencies are defined to be $\lambda_{target} = 1553nm$ and $f_{target} = 5.025GHz$. These targets are set only to provide a reference during our tuning process. However, the main goal is tuning all the OMCs at the same optical wavelength and acoustic frequency simultaneously, within their respective linewidths. In a different scenario, targets could be strictly enforced where the target wavelength and frequency requirement is set by a fixed reference, for example, three OMCs tuned to be resonant with a fourth OMC that poses the target. Note that the required tuning ranges are greater than 1nm and 30MHz even though the wavelength and frequency differences between different OMCs are smaller.

Three joint patterns for three OMCs are generated using pattern generation algorithm using

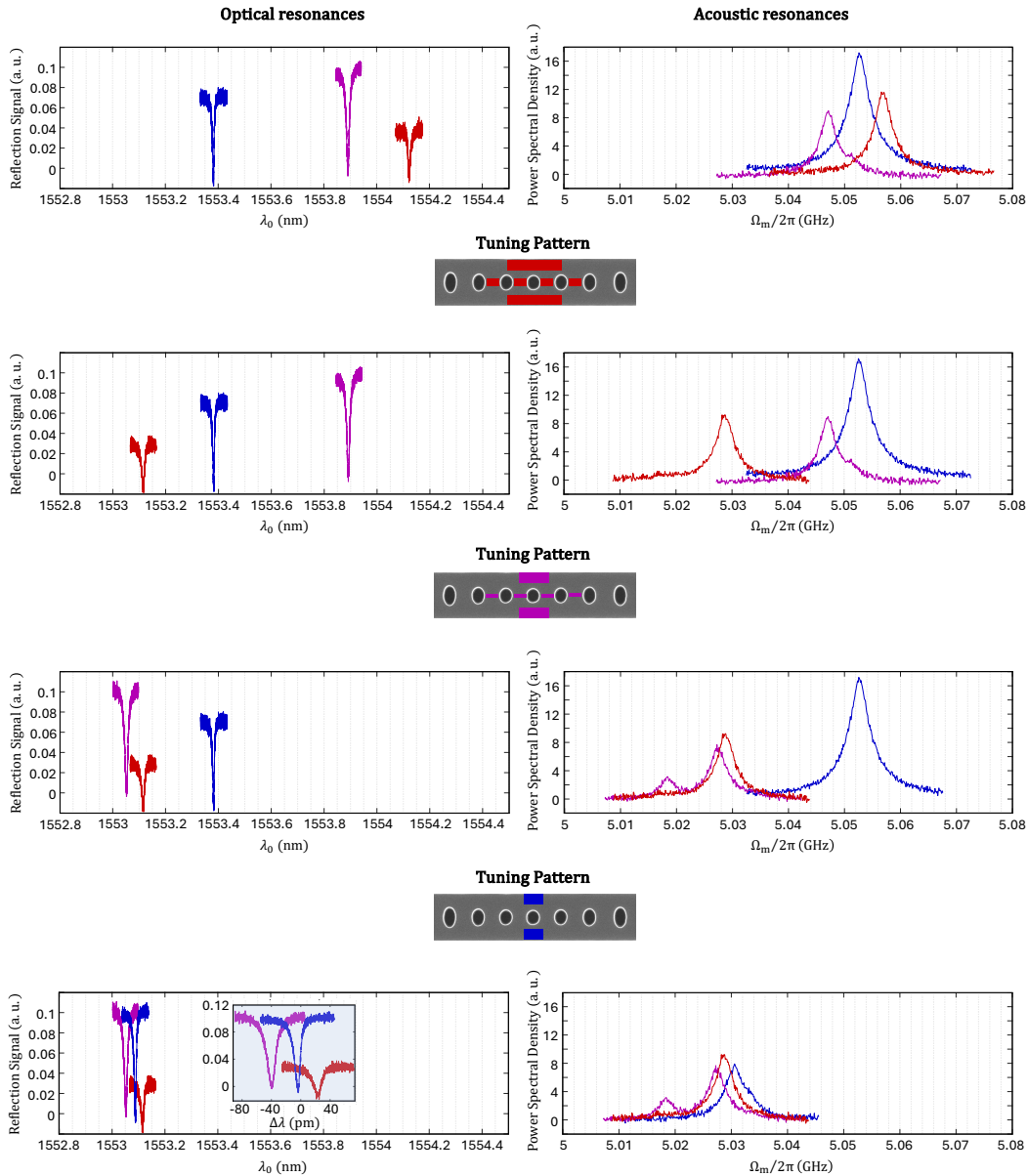


Figure 2.21: **3 Steps of coarse tuning.** Panels show 3 steps of fine tuning from the initial condition (first row) of the selected OMCs. Applied patterns are shown in between steps. Patterns are applied one by one for each OMC. At the final step (last row) coarse alignment within 80nm and 5MHz is achieved.

$$\delta\lambda_{coarse} = \lambda_0 - \lambda_{target} + \delta\lambda_{fine}, \quad (2.6)$$

$$\delta f_{coarse} = f_0 - f_{target} + \delta f_{fine}. \quad (2.7)$$

Since our tuning method is unidirectional, we need to apply some margin to our

coarse tuning. Here we choose $\delta\lambda_{fine} \approx 100pm$ and $\delta f_{fine} \approx 5MHz$ to account for possible uncertainty in the coarse alignment as well as to leave a margin for the fine tuning process. As a result, the algorithm suggests a shift pattern with four independent parameters $\{w, l, M_o, M_a\}$ where w is the optics focusing pattern width (with constant pattern lengths), l is the acoustic focusing pattern length (with constant pattern width), $M_o(M_a)$ is a binary variable which denotes mild or aggressive oxidation mode for optics (acoustic) focused pattern. Generated patterns are applied on the OMCs one by one and final resonance wavelengths and frequencies are measured (see Figure 2.21). It is possible to see that the OMC plotted in magenta (OMC M) and the OMC plotted in red (OMC R) have both optics and acoustic focusing patterns in their respective joint patterns whereas the OMC plotted in blue (OMC B) only needs acoustic focused pattern to tune both optical and acoustic resonances into the target since it has the lowest optical wavelength.

After coarse tuning steps, three optical resonances are tuned within less than 100nm while all three acoustic resonances are successfully tuned within 4MHz to each other. The satellite peak that is around 5.018GHz on OMC M belongs to another OMC that is coupled to the same optical coupler. All the resonances are sufficiently close to each other, and they are close enough to the respective target values.

Real-time fine-tuning of OMCs with pixel-by-pixel oxidation

As opposed to the coarse alignment steps where we use predefined oxidation patterns, in the fine-tuning sequence we apply small perturbations on the strategic locations and we use real-time feedback coming from the in situ optical and acoustic measurements after every oxide pixel applied. This technique helps us to approach towards the desired wavelength and frequency targets incrementally and lowers the chance of overshooting. Fine tuning must be performed starting from the resonance component that is farther from the target, however if the required tuning is comparable, it is wiser to selectively tune acoustic frequency first. This way parasitic tuning of optical resonance can be tolerated or might even be beneficial since the optical wavelength approaches to the target. This is not the case for the selective optical tuning because parasitic tuning of acoustic resonance is negligible thanks to the larger regions of high optical selectivity. Moreover, acoustic resonances are more tolerant to tuning errors since their linewidths are larger compared to optical resonance linewidths weighted by the respective tuning response.

We start with OMC B by tuning the acoustic resonance into 5.027GHz and optical

wavelength is shifted by 50pm after the first manipulation (Figure 2.22 first row). Second fine-tuning step is applied to the OMC R, shifting its acoustic frequency to 5.0261GHz and optical wavelength ended up being 1553.031nm (Figure 2.22 second row). We overshoot slightly on both resonances. In the third fine-tuning step, OMC M acoustic frequency is tuned into 5.0266GHz while optical wavelength is tuned to 1553.029nm (Figure 2.22 third row).

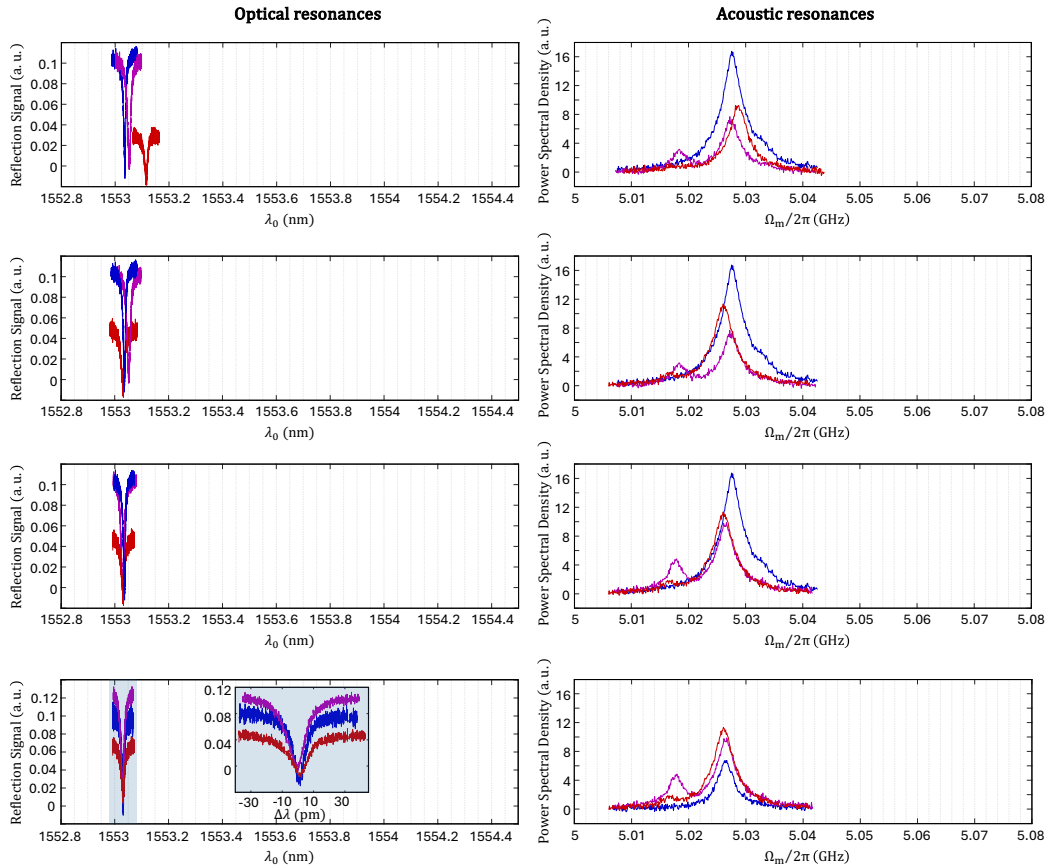


Figure 2.22: **4 Steps of fine tuning.** Panels show 4 steps of fine tuning starting from the initial condition (Figure 2.21 last panel). Fine tuning patterns with real-time monitoring are applied one by one first on blue OMC, then red and magenta OMC, and finally on blue OMC. At the final step (last row) final alignment within $2pm$ for optical wavelength λ and $150kHz$ for acoustic frequency Ω_m is achieved.

After three steps of fine tuning, alignment of three optical and acoustic resonances are already acceptable since the maximum detuning is smaller than the minimum linewidth in the set. However, one last fine-tuning step can be applied on OMC B since both optical and acoustic resonances are higher compared to other two OMCs.

Fourth fine tuning step is applied to OMC B which tunes the optical wavelength and acoustic frequency to 1553.031nm and 5.0264GHz. After the final step of fine-tuning, we aligned optical resonance wavelengths of three OMCs within 2pm while acoustic frequencies are tuned within 500kHz (Figure 2.22 fourth row). Final, fine tuned optical mode wavelengths and acoustic mode frequencies of the three OMCs are given below.

$$\lambda_R = 1553.031nm, \quad \lambda_B = 1553.031nm, \quad \lambda_M = 1553.029nm$$

$$\Omega_{m,R}/2\pi = 5.0261GHz, \quad \Omega_{m,B}/2\pi = 5.0264GHz, \quad \Omega_{m,M}/2\pi = 5.0266GHz$$

2.12 Conclusion

In this chapter we demonstrated simultaneous, real-time tuning of both optical and acoustic resonances in optomechanical crystal cavities using AFM-based nano-oxidation. The technique enabled tuning ranges exceeding 2 nm in optical wavelength and 60 MHz in acoustic frequency. These ranges can be further extended by forming thicker oxide layers through contact-mode AFM operation as discussed in the next chapter. In the context of OMC-based microwave-optical quantum transducers, this post-fabrication tuning method enables frequency alignment across multiple nodes of a quantum network. Furthermore, the technique is compatible with alternative material platforms such as silicon nitride [62], where post-fabrication tuning may also be critical [63].

In Chapter 3, we will explore the use of contact mode nano-oxidation for higher range, selective optical mode tuning for wavelength alignment at cryogenic conditions.

TUNING OMCS FOR CRYOGENIC OPERATIONS

So far, we have introduced the AFM nano-oxidation technique and demonstrated simultaneous, in situ tuning of optical and acoustic modes in optomechanical crystals using this method. Hybrid optomechanical crystal-based microwave-optical transducers are designed to operate at cryogenic temperatures, enabling single-photon-level interactions in the optomechanical and piezo-acoustic domains. These transducers serve as intermediaries between superconducting qubits and terahertz-frequency optical photons, which are inherently robust against thermal noise at room temperature. However, the optical and acoustic mode frequencies of hybrid optomechanical crystals shift upon cooling due to changes in the material properties of silicon and the introduction of thermal stress hence, a more comprehensive strategy is required to achieve precise mode alignment for cryogenic operation.

In this chapter, we present a selective, high-range optical mode tuning method based on contact-mode AFM nano-oxidation. Moreover, we investigate the key factors influencing optical mode shifts in optomechanical crystals, aiming to develop a systematic methodology for the alignment of the optical mode wavelengths at cryogenic temperatures.

3.1 Modified AFM nano-oxidation setup

In Chapter 2, we introduced the modified atomic force microscope (AFM) integrated with an optical probing setup used in the in situ tuning experiments. In this configuration, optical probing is performed using a dimpled fiber taper, as described in Section 2.6. This method is advantageous for rapid OMC prototyping, as it requires no additional fabrication steps beyond the standard silicon etching process used to define the OMCs. While this approach offers speed and simplicity at room temperature, its relatively low coupling efficiency, complicated alignment procedure and larger footprint render it suboptimal for cryogenic applications.

The state-of-the-art technique for flexible and efficient optical coupling into optomechanical crystals (OMCs) at cryogenic temperatures is the end-fire fiber coupling method. In this approach, a lensed optical fiber is used to focus the Gaussian mode of a single-mode fiber to a beam waist of approximately $2.5\mu\text{m}$, located around

14 μm from the fiber tip. Coupling is achieved by aligning the lensed fiber with an on-chip end-fire coupler. Precise alignment can be done with the feedback coming from the reflected optical signal, which allows alignment in the dilution refrigerator without a camera setup. This method enables high-efficiency optical access, with coupling efficiencies reaching up to $\sim 70\%$ [64].

To adapt the AFM nano-oxidation setup for compatibility with the cryogenic measurement platforms in our laboratory, the optical probing module integrated with the AFM was modified to incorporate an end-fire coupling scheme. A four-axis electromechanical manipulator was implemented to enable precise in situ alignment of the lensed fiber with the on-chip coupler.

3.2 Contact mode AFM nano-oxidation for optical mode tuning

In the simultaneous in situ tuning experiments, our objective was to align both the optical and acoustic resonances of an individual optomechanical crystal (OMC) to predefined target values. Achieving this required exceptionally high spatial resolution to address mode shapes and selectively tune the desired resonance frequencies by oxidizing regions with high modal selectivity—often confined to areas no larger than tens of nanometers. In this chapter, we primarily focus on optical wavelength tuning, while taking care to minimize parasitic shifts in the acoustic mode. This allows us to utilize contact-mode AFM oxidation, which is more aggressive and less spatially precise than tapping mode, enables the formation of thicker oxide layers. Expanding the accessible tuning range is essential, as transducer fabrication involves multiple steps that introduce disorder across the chip, manifesting as optical resonance wavelength variation among devices.

Based on the oxidation characterization presented in Chapter 2, we chose to utilize a different set of simplified parameter space for our tuning characterization study with contact mode.

In the case of tapping mode oxidation, bias voltage was fixed to the maximum available voltage value of 10V throughout the experiment. The reason behind this choice is the brief interaction duration between the AFM tip and the silicon surface during tapping mode operation. In the contact mode, tip-surface interaction is considerably higher given that the tip is constantly in contact with the surface. As a consequence, lower voltage values can trigger the oxidation reaction by surpassing the electric field threshold required for nano-oxidation. This emerges as a great control knob for the oxidation depth/thickness because our ability to predictably and

stably control the bias voltage is greater compared to other oxidation parameters.

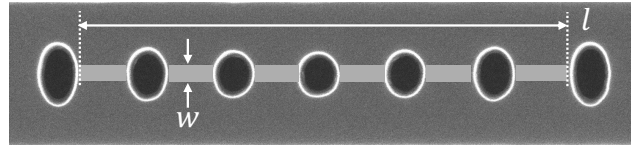


Figure 3.1: **Contact mode oxidation isolated optics tuning pattern.** The pattern proposed for selective optical mode tuning passing through the longitudinal axis of the nanobeam, spanning from ellipse L3 (third ellipse to the left from the center) to R3 (third ellipse to the right from the center). Width w of the pattern is fixed at 2 pixels which takes different values ranging between 90 – 110nm based on the the utilized tip bias voltage.

In this study, we keep the optics targeting pattern length and width fixed. Moreover, instead of using a set of 4 patterns, we use 6 rectangular patterns that extend from the ellipse L3 to R3, centered around the center ellipse (see Figure 3.1). In principle, similarly to the in situ simultaneous tuning experiments, the number of rectangular patterns as well as their widths can be altered to adjust the resulting tuning. However, keeping the pattern width as small as possible and increasing the oxide thickness is a more conservative approach since this way the pattern is confined within the high optical selectivity regions and expected to shift acoustic frequency minimally. Pattern width is fixed to 2 pixels around the longitudinal line with a pitch of 13nm which results in a pattern width w that ranges between 90nm-110nm depending on the bias voltage.

Figure 3.2 shows the bias voltage dependent nano-oxidation tuning results on OMCs, where 3 OMCs are oxidized and probed for each data point. Oxidation starts to take place at 5V and resulting tuning increases with the increasing bias voltage. Maximum wavelength shift is demonstrated at a bias voltage of 9V where we observe ~ 6nm wavelength tuning. Achieved wavelength tuning shows nearly 5 fold improvement over the most aggressive optical wavelength tuning results presented in Chapter 2. On the other hand, parasitic acoustic mode tuning is less than 50MHz throughout the range which is within the acceptable limits. Internal voltage source of the AFM used in this experiment can go up to 10V, which can result in wavelength shifts exceeding 11nm, however this much perturbation introduced on the OMC surface distorts the acoustic mode and presumably the optomechanical coupling to the point the acoustic mode becomes undetectable through optomechanical probing.

Figure 3.3 shows the change in intrinsic optical quality factor between different

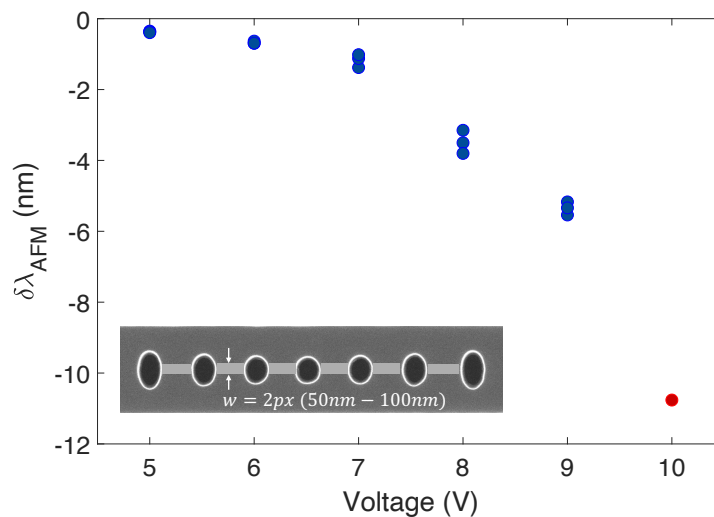


Figure 3.2: **Optical wavelength shift with respect to the tip bias voltage.** Optical wavelength shift after contact-mode oxidation, measured for different tip bias voltages ranging from 5 V to 10 V. Three OMCs were measured for each voltage from 5 V to 9 V. The red data point corresponding to a 10 V bias was obtained from a single OMC. The inset shows the dimensions of the applied oxidation pattern.

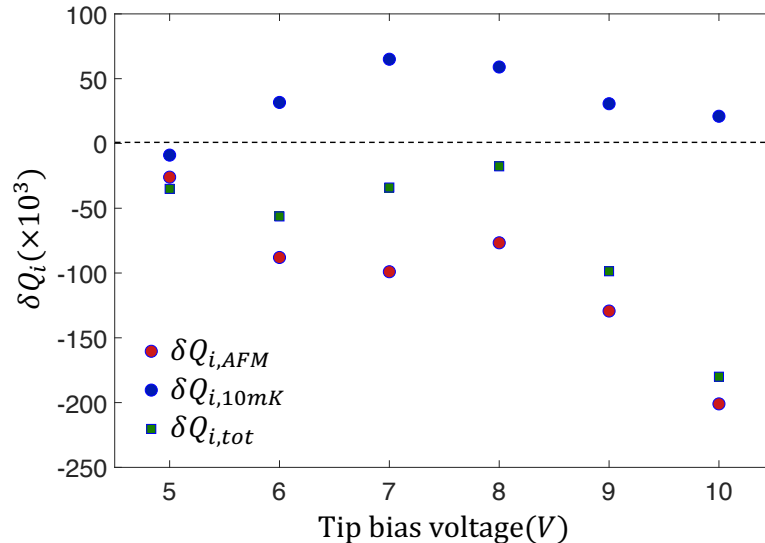


Figure 3.3: **Change in optical intrinsic quality factor.** Average change in intrinsic quality factor Q_i after the AFM nano-oxidation tuning (red points), between AFM nano-oxidation tuning and chip cool down to 10mK (blue points) and between the initial Q_i and Q_i at 10mK (green squares).

stages of the measurements. A decrease in the optical quality factor is observed after AFM nano-oxidation tuning, which is expected as the oxide layer created introduces scattering sites and imperfections on and under the surface of the OMC. Although, a slight increase in optical quality factors is observed when the OMCs are cooled down to cryogenic temperatures, the final optical quality factors are measured to be lower than initial values which are measured right before the tuning process. Degradation in optical quality factors remain lower than 100×10^3 until 9V tip bias voltage. For higher voltages, the increase in optical intrinsic scattering rate approaches to the tolerable limits, which makes higher range oxidation tuning unpractical.

3.3 Wavelength change due to native oxidation in room temperature

From the moment OMCs are exposed to atmosphere for the first time after HF vapor release, a layer of silicon oxide compound starts to form on the surface due to spontaneous oxidation driven by the ambient humidity. The refractive index of the oxidized silicon layer is smaller than that of the pure crystalline silicon thereby the optical resonance of the OMC undergoes a continuous blue shift as the surface oxidizes. It is very important to keep track of this drift as it will contribute to the tuning of the OMCs.

To quantify the effect of the native oxidation on the optical resonance wavelength, we set an experiment where we constantly probe an OMC that sits in atmosphere right after the release process. Data taken over the course of 10 hours with a rate of 1 data point per minute, results are shown in Figure 3.4. It is possible to see that native oxidation promotes an approximately linear decay in the optical resonance wavelength during the first ~ 5 hours and the decay slope decreases over time. Standard duration is 3 to 5 hours for a transducer cooldown preparation that includes preparing the sample package with wire bonding for signal lines and ground plane, preliminary optical and acoustic mode measurements, required tuning process, loading onto the cryogenic testing platform and starting the cooldown process. This means we can approximate the decay due to native oxidation with a linear relation with a rate of 2.5pm/min. This rate is used to determine the optimal oxidation parameters and to estimate the exact time to start the sample cooldown to obtain the desired wavelengths at cryogenic temperatures.

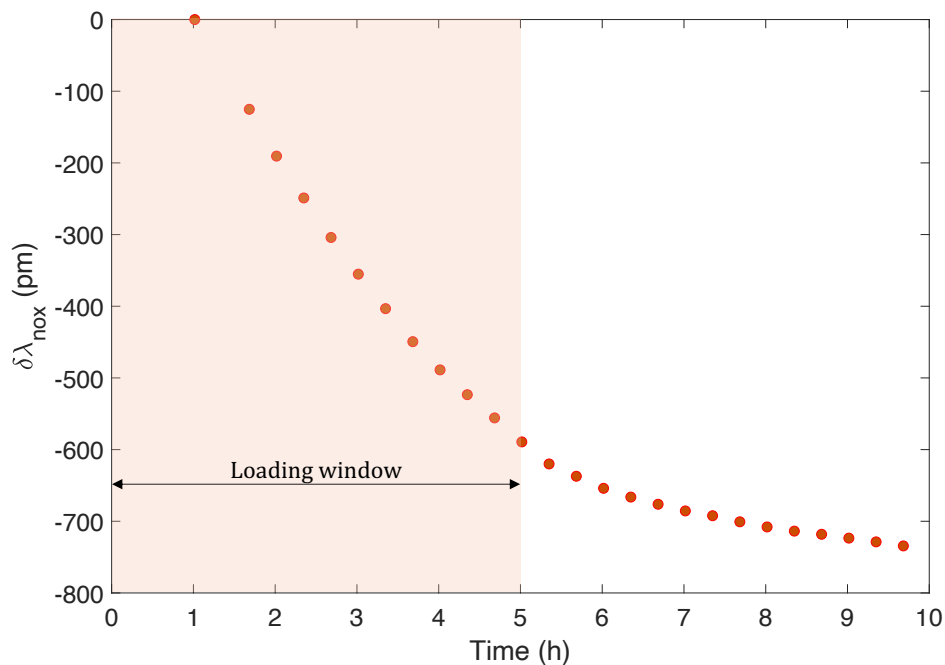


Figure 3.4: **Wavelength drift due to native oxidation.** Wavelength shift of an OMC due to native oxide formation on the surface. OMC under test is probed continuously during 10 hours starting from the vapor HF release process which passivates the silicon surface. Shaded region shows the duration of air exposure during the sample loading process.

3.4 Temperature dependent wavelength shifts of OMCs at 10mK

Optomechanical crystals confine light within their cross section thanks to the material permittivity contrast between the OMC medium (in our case silicon) and surrounding medium (in many cases air or vacuum). Introduction of the periodically patterned holes creates a photonic band gap by periodically modulating the permittivity within a unit cell hence prohibits the longitudinal light propagation. Adiabatic shrinkage of the patterned holes towards the center of the OMC gives rise to confinement of light (and acoustic vibrations) in the center of the nanobeam while suppressing unwanted out of plane scattering. The frequency of the confined light is specific to the dimensions of the critical features, namely the beam cross section, cavity hole dimensions and periodicity, and the permittivity contrast between the OMC medium and the surrounding. Any effect that can alter these parameters can effectively change the frequency of the supported modes in the cavity.

Change in temperature can influence all critical parameters. In this subsection, we will focus on the temperature change from ambient (room temperature or 293K) to

cryogenic (10mK at the mixing plate of the dilution refrigerator) temperatures.

Change in volume and stress

Most solids experience contraction when cooled down due to the reduced mobility of the atoms. Temperature dependent coefficient of thermal expansion (CTE) of the material dictates the amount of the change in the volume per unit temperature change. For silicon, thermal expansion coefficient $\alpha = 2.55 \times 10^{-6}$ at $T = 293K$ and it decreases with decreasing temperature from room temperature to 125K and becomes negative from $\sim 125K$ to $\sim 8K$ where it settles at negligible values ($\sim 10^{-9}$) [65]. The total thermal strain from 293K to 10mK is estimated as $\varepsilon = -2.15 \times 10^{-4}$, obtained by integrating the empirical temperature-dependent thermal expansion coefficient $\alpha(T)$ data presented in Figure 3.5.

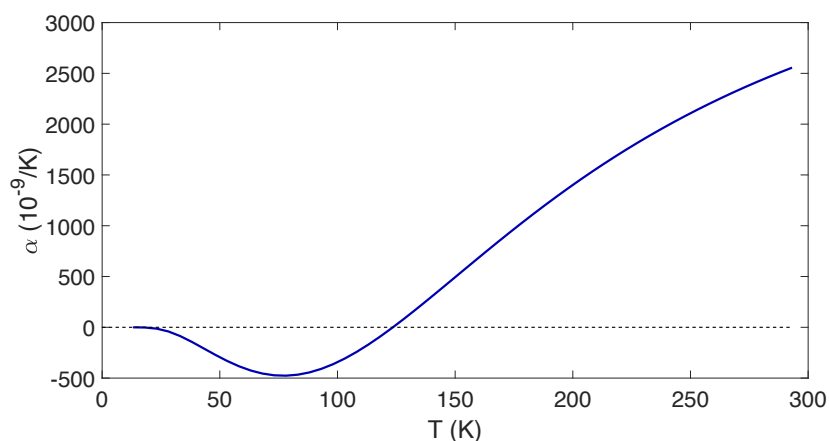


Figure 3.5: **Temperature versus coefficient of thermal expansion of silicon.** Change of the coefficient of thermal expansion with respect to temperature from 293K to 8K. Plot generated based on the data presented in Ref [65].

We estimate the volume and stress change using the obtained thermal strain. Results suggest that the change in the pattern dimensions is negligible ($\ll 1nm$) while the resulting tensile stress (tens of MPa) contributes to the mechanical frequency shift. This is an important factor for the acoustic mode since the decreasing compressive stress on the device layer silicon shifts the frequencies up however, optical mode is affected minimally.

Change in the refractive index

Thermo-optic effect is a phenomenon in which a material's refractive index changes in response to temperature variations following the thermo-optic coefficient dn/dT .

For silicon, this effect originates from the changing energy band gap and carrier charge density. At room temperature, thermo-optic coefficient of silicon is reported to be $2 \times 10^{-4} K^{-1}$ [66]. When cooled down, silicon experiences a reduction in the refractive index according to the thermo-optic coefficient. Komma et. al [66] reported that thermo-optic coefficient of silicon drops drastically after 50K and reaches values on the order of 10^{-8} close to 10mK. Nevertheless, from room temperature to 150K, the thermo-optic coefficient of silicon stays on the order of $4 \times 10^{-4} K^{-1}$ which leads to a substantial drop in refractive index up to 1% ($\sim 1.7\%$ in relative permittivity).

A typical OMC designed for a room temperature optical resonance wavelength of 1550nm is simulated using various relative permittivity values and different scale factors to study the effect of the change in refractive index on the optical resonance wavelengths. Scale value was swept between 98% to 102% while the relative permittivity is swept from the room temperature (reference case) value of $\epsilon_r = 11.7$ to the estimated value of $\epsilon_r = 11.5$ that corresponds to 10mK, results are plotted in Figure 3.6.

Simulation results show that the 1% change in refractive index can shift the optical mode drastically, by more than 12nm around $\lambda_0 = 1550nm$. This demonstrates that the thermo-optic effect is the dominant cause of optical mode shift from room to cryogenic temperatures. Simulated data shows a linear relation between the change in refractive index and the room temperature resonance wavelength. This is due to the change in the mode volume for different scaling factors which influences the effective change in the mode volume due to the changing refractive index values.

To study thermal effects in the range from room temperature to 10mK, the test sample previously used for contact mode oxidation studies is cooled down. The sample contains total of 15 OMCs that was oxidized using AFM nano-oxidation with different bias voltage values between 5-9V as well as 8 non-oxidized OMCs. Within 15 OMCs that was oxidized in AFM nano-oxidation setup, 7 OMCs had an initial resonance wavelength of $\lambda_{0,avg} = 1564.5nm$ while 8 OMCs had an initial resonance wavelength of $\lambda_{0,avg} = 1554.5nm$. All 23 OMCs under consideration were probed optically and acoustically at 10mK.

As a result of the cryogenic measurements, we made two major observations that correlate room temperature properties/operations of the OMCs to their optical and acoustic properties at cryogenic temperatures. Figure 3.7a shows the thermal wavelength shifts of 8 OMCs with respect to their respective initial wavelengths measured

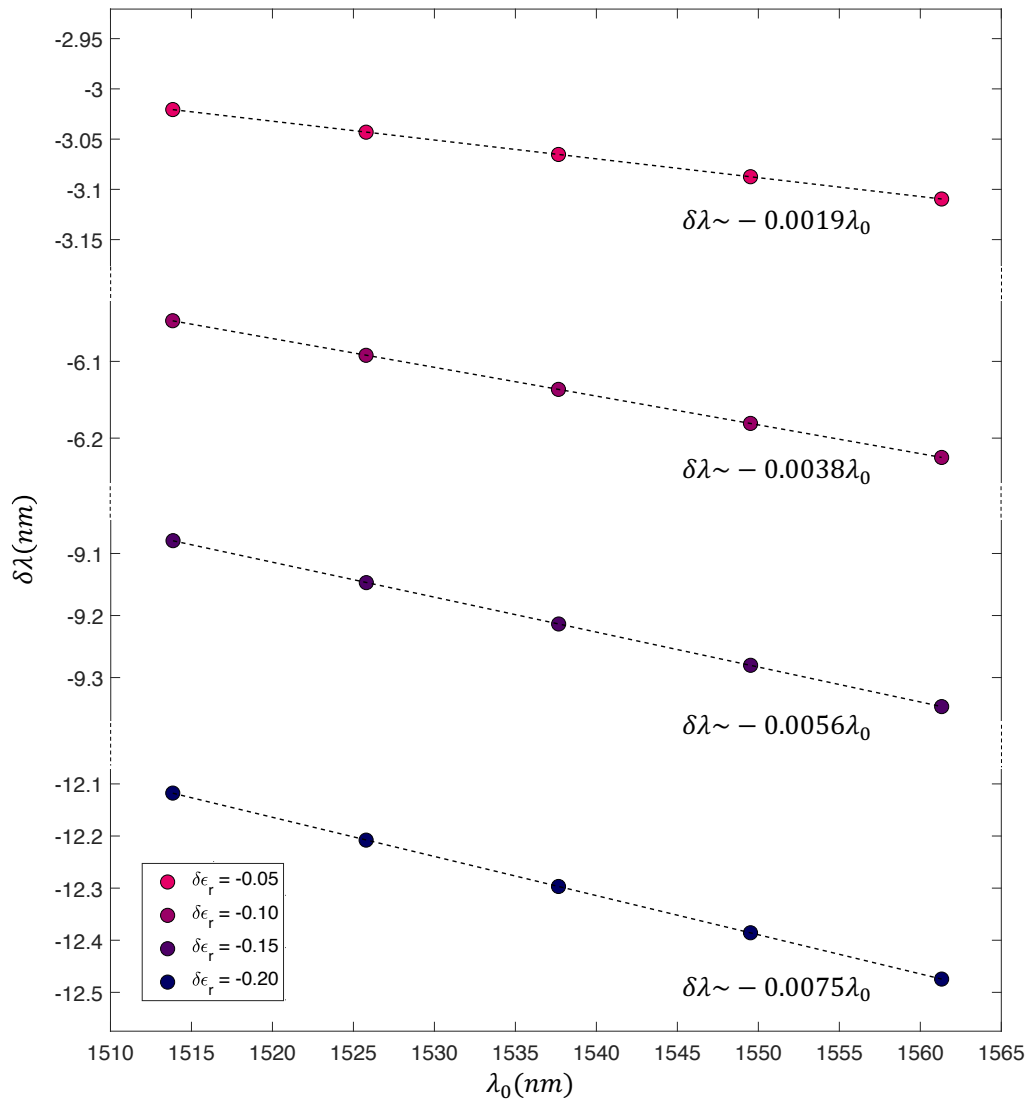


Figure 3.6: **Optical wavelength shift due to changing permittivity** Simulated optical wavelength shift of OMCs with different base optical mode wavelengths (assuming a reference relative permittivity of $\epsilon_r = 11.7$) as a function of varying relative permittivity values. Dashed lines represent linear fits, highlighting the dependence of the optical wavelength shift on the base wavelength due to changes in permittivity.

at room temperature. There is a linear relation between the room temperature resonance wavelength and wavelength change at cryogenic temperatures that has a linear coefficient of $\sim 1\%$. This slope is larger compared to the simulated linear relation presented earlier in this chapter. The possible sources of discrepancy could be the different factors contributing the change in the initial wavelengths, such as random

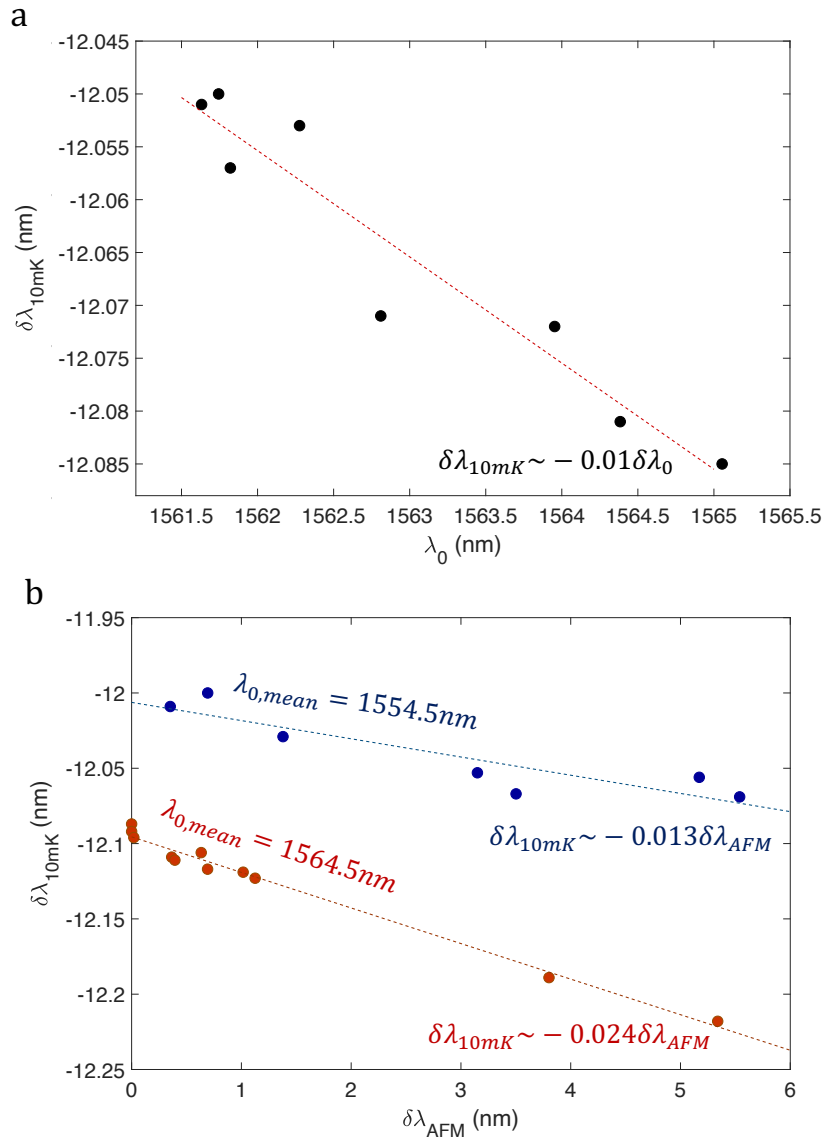


Figure 3.7: **Thermally induced optical wavelength shift.** **a)** Optical wavelength shift of unoxidized OMCs measured at 10 mK. The dashed line represents a linear fit that captures the room-temperature wavelength dependence of the cryogenic wavelength shifts. **b)** Thermally induced optical wavelength shift as a function of AFM nano-oxidation tuning applied to two sets of OMCs with different base optical wavelengths (blue and red data points). The dashed lines indicate a linear relationship between the applied tuning and the resulting thermally induced optical wavelength shift.

errors and native oxidation, and disregarded contributions coming from the volume change due to thermal contraction.

Second important observation that was revealed from the cryogenic measurements

was the correlations between the AFM nano-oxidation tuning and the thermal wavelength shifts observed at 10mK. According to the data shown in Figure 3.7b, there is a linear relation between the wavelength shift due to AFM nano-oxidation and the thermal wavelength shift at 10mK. Thermo-optic coefficient of silicon dioxide is reported to be lower than that of silicon in room temperature $dn_{SiO_2}/dT \approx 8.5 \times 10^{-6}$ [66] however below 30K, thermo-optic constant of silicon drops sharply below the silica value which explains the higher shift observed for oxide rich OMCs. While the relation stays linear within the two sets of OMCs with different initial resonance wavelengths, the linear coefficient or slope is observed to change with respect to the average initial wavelength. At the zero-tuning point where the extrapolated fitting lines cross the $\delta\lambda_{AFM} = 0$, it is possible to see a difference of $\sim 100pm$ in thermal shift between two sets of OMCs with $\lambda_{0,avg} = 1564.5nm$ and the extrapolated values of the second set with $\lambda_{0,avg} = 1554.5nm$ that follows the previously revealed relation.

3.5 Tuning protocol for cryogenic wavelength alignment

In the previous sections, we explored the mechanisms that govern the post fabrication optical wavelength shifts until we reach a stable resonance wavelength at 10mK. We have three major mechanisms that must be taken into account during the tuning sequence.

AFM nano-oxidation: A selective ‘tuning knob’ which depends on the applied tip voltage. By interpolating the characterized $V - \delta\lambda$ relation, we can estimate the required amount of oxidation for the desired optical wavelength shift. Voltage range is set to 5-9V where we observe predictable optical tuning with increments of 10mV which ensures <500pm tuning accuracy over tuning range of 0-6nm. Wavelengths must be fine-tuned using previously discussed fine-tuning techniques after the coarse alignment guided by the $V - \delta\lambda$ curve. Depending on the required tuning, either tapping mode or contact mode can be used at this stage.

Native oxidation: A self-limiting time dependent global blue drift that take effect after the hydrofluoric acid release process. During and after the AFM nano-oxidation process where the sample is exposed to ambient conditions, every OMC experiences blue drift with an approximately constant rate of 2.5pm/min for the first 5 hours. Oxidation slows down and eventually self-saturates as

the oxide layer building up on the surface inhibits the oxidation reaction by limiting the air exposure of the silicon.

Thermo-optic shift: A temperature dependent blue shift due to changing refractive index of the silicon from room temperature to 10mK. OMCs experience a blue shift that depends on their respective unperturbed wavelengths and the oxide volume built up due to previous processes. Both dependencies can be represented with a linear relation. Moreover, linear rate that relates AFM nano-oxidation to the thermo-optic shift is a function of the initial wavelength of the OMC.

After individually identifying the contributing factors, we came up with an expression that relates the initial wavelength to the final wavelength at 10mK.

$$\lambda_{10mK} = \lambda_0 + \delta\lambda_{nox}(t) + \delta\lambda_{AFM}(V) + \delta\lambda_{th}(\delta\lambda_{nox}(t), \delta\lambda_{AFM}(V), \lambda_0) \quad (3.1)$$

Following is the protocol that is executed starting from the recovery of the samples from the hydrofluoric acid release process.

1. Packaging: Sample packaging including placement of the sample into the sample holder and required wire bonding for transducer applications.
2. Pre-mapping in N2 environment: OMCs are measured in an enclosed N2 chamber to map the existing resonance values while minimizing native oxidation. OMCs with suitable properties are selected for AFM nano-oxidation tuning process.
3. AFM nano-oxidation: Selected OMCs are measured in the optical setup embedded in the AFM enclosure. Initial wavelength, measured wavelength in AFM setup, target wavelength at 10mk and foreseen pumpdown time is fed to the algorithm. The algorithm, based on the relation derived in the previous section, suggests a target wavelength to be tuned in the AFM setup and a target wavelength at which the pumpdown must be started. Assumed tuning duration is 10min per OMC which is utilized to correct for the 25pm native oxidation shift that takes place in the meanwhile. If the tuning process takes more time to execute, tuning must be offset by the rate of 2.5pm/min.

An example case is given to demonstrate the algorithm working principle. Let us assume that OMCX was measured in the mapping stage and its wavelength is recorded to be $\lambda_0 = 1560\text{nm}$. At 3:00pm, OMCX is loaded into AFM setup and the wavelength measured was $\lambda_{AFM} = 1559.9\text{nm}$. The target wavelength at 10mK is determined to be $\lambda_{target} = 1543\text{nm}$ and the foreseen pump down time is 5:00pm hence time to pumpdown is 120 minutes. Based on the data and targets fed into the algorithm, output values are as follows.

$$\delta\lambda_{AFM} = 4.352\text{nm}, \quad \lambda_{target,AFM} = 1555.623\text{nm}$$

$$V_{tip} = 8.2\text{V}, \quad \lambda_{pd} = 1555.235\text{nm}$$

Where $\delta\lambda_{AFM}$ is the amount of tuning needed, $\lambda_{target,AFM}$ is the target wavelength to be reached at the end of nano-oxidation tuning, V_{tip} is the suggested tuning voltage and λ_{pd} is the target wavelength at the moment of the pump-down.

4. Pumpdown: Selected OMCs are probed while loaded in the dilution refrigerator prior to the pump down. This step is crucial since the target wavelength can be reached at 10mK only by starting the pumpdown at a specific wavelength value since the shift in between is fixed. At this stage, sample must be exposed to air and resonance wavelength must be monitored closely until it reaches the target pumpdown wavelength. Each OMC has a different target pumpdown wavelength since the thermal shift depends on the initial OMC properties and tuning applied during the AFM nano-oxidation process however, ideally, every OMC must reach their respective target pumpdown wavelengths at the same time, hence it suffices to probe a single OMC to precisely timing the pumpdown process.

3.6 Tuning multiple OMCs for wavelength alignment at 10mK

After characterizing various mechanisms leading substantial variations in the expected wavelength shift at cryogenic conditions, findings were used to develop a tuning method as presented in the previous sections. Established tuning method was used to tune randomly selected 5 OMCs to achieve wavelength alignment at 10mK (see Figure 3.8). Optical resonance wavelengths of the selected OMCs are tabulated below, OMCs are color coded. Optical modes of the selected OMCs have a standard deviation of $\sigma_\lambda = 694\text{pm}$. Wavelength target at 10mK is set to be 1546.626nm ¹.

¹'626' being the area code of Pasadena, CA, a *very* specific number to shoot for.

$$\lambda_B = 1561.451nm, \lambda_M = 1561.858nm, \lambda_G = 1562.132nm$$

$$\lambda_Y = 1562.322nm, \lambda_R = 1563.310nm$$

OMCs were tuned using the AFM nano-oxidation method with shift amounts predicted by the tuning algorithm presented in the previous sections. The integrated optical fiber in the dilution refrigerator setup is parked on OMC R (OMC shown in red in Figure 3.8) before the pump down started. Pump down started when the target pump down wavelength $\lambda_{pd,OMCR} = 1558.724nm$ is reached. Measured optical wavelengths at 10mK (see Figure 3.8b) are given below. Optical mode wavelegnth of the selected OMCs have a standard deviation of $\sigma_\lambda = 32pm$.

$$\lambda_B = 1546.572nm, \lambda_M = 1546.488nm, \lambda_G = 1546.546nm$$

$$\lambda_Y = 1546.516nm, \lambda_R = 1546.550nm$$

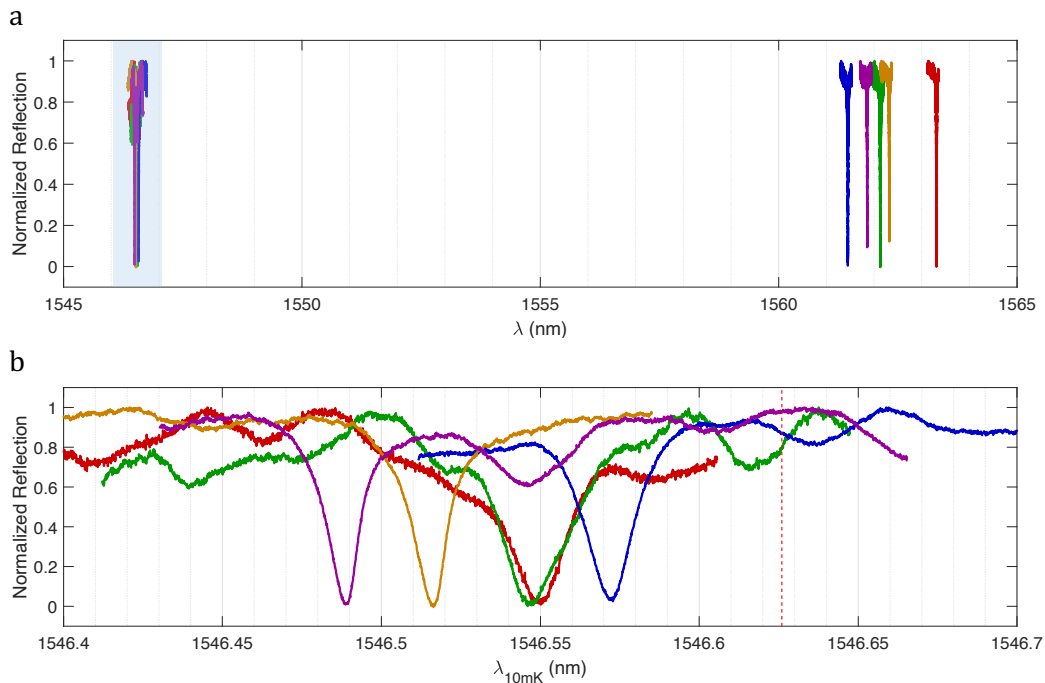


Figure 3.8: Tuning of 5 OMCs for alignment at 10mK. a) Initial room temperature (right) and final cryogenic (left) wavelength distribution of 5 OMCs after AFM nano-oxidation tuning. **b)** Close up of the blue shaded region on the panel **a** showing resonance wavelength of the OMCs under test at 10mK. Red dashed line indicates the target wavelength.

Resulting wavelength alignment suggest > 20 fold improvement over the initial variance of the selected OMCs. A global wavelength shift can be observed from the designated target wavelength by 92pm. A reduction of the intrinsic optical quality factors by $\sim 15\%$ is observed due to the extra scattering sites introduced by AFM nano-oxidation however, quality factors improve after OMCs are cooled down to 10mK. The average intrinsic optical quality factors of the tested OMCs exhibited negligible degradation, less than 5%, corresponding to an additional intrinsic loss rate of ~ 45 MHz.

3.7 Discussion

In this chapter, we presented a comprehensive strategy for aligning the optical resonances of optomechanical crystals for operation at cryogenic temperatures. By combining contact-mode AFM nano-oxidation, which expands the tuning range by a factor of five compared to the tapping-mode technique, with careful management of native oxidation and a quantitative understanding of thermo-optic shifts, we achieved alignment of multiple OMCs at 10mK. Our results demonstrate that AFM nano-oxidation is an effective, high-resolution post-fabrication tuning technique for OMC-based microwave-optical transduction platforms operating under cryogenic conditions.

Tuning accuracy can be further improved through better temperature regulation across measurement platforms and careful humidity control during the oxidation process. Multiple optical probing setups are employed from the initial characterization of the OMCs to the final measurement in the dilution refrigerator prior to cooldown. Variations in ambient and surface temperatures between these setups can introduce measurement inconsistencies by shifting the optical resonance wavelengths, due to the relatively high thermal expansion coefficient and thermo-optic response of silicon at room temperature. An ideal approach would involve implementing active temperature control at each probing station to ensure stable and consistent conditions throughout the tuning sequence.

Chapter 4

OTHER AVENUES USING BIASED TIP AFM

So far, we have demonstrated in situ, simultaneous tuning of optical and mechanical resonances in optomechanical crystals, as well as high-range, selective optical tuning for cryogenic applications using the AFM nano-oxidation technique. In this chapter, we explore additional capabilities of biased-tip AFM, including its potential for advanced control in silicon optomechanical systems and its applicability to emerging material platforms such as lithium niobate ($LiNbO_3$).

4.1 Post-fabrication band tuning with nano-oxidation

Localized oxidation provides a powerful means to tune the optical and mechanical resonances of optomechanical crystals by leveraging the material contrast between silicon and silicon oxide. The nano-oxidation process induces a localized refractive index change and modifies the elastic properties of the structure due to the increased density and stiffness of the resulting silicon oxide. These localized perturbations predictably shift the eigenfrequencies of the confined optical and acoustic modes, enabling fine control over the resonances. The same mechanism can be employed to alter the bandgap properties of the periodic mirror cells in an optomechanical crystal or the elements of a phononic shield, allowing for selective modification of the mass and refractive index distribution on the structures. Furthermore, in hybridized systems where mechanical modes span multiple substructures connected via phonon waveguides, nano-oxidation can enable spatial control over mode participation by locally perturbing the waveguide geometry, thus tailoring the hybridization strength and spatial distribution of mechanical mode energy.

Hybrid electromechanical systems use piezoelectric materials to enable strong coupling between gigahertz-frequency mechanical modes and external microwave circuits. While these platforms offer high electromechanical coupling rates, they often introduce additional mechanical loss due to their complex crystal structures, which host two-level systems and other impurities as well as due to the metallization used for the electrical connections that participates the mechanical mode. To mitigate this, a common approach is to hybridize a piezo-acoustic cavity with a high-quality silicon phononic crystal resonator via a phonon waveguide. Precise control over the mechanical hybridization is essential for implementing phonon-based quantum

memories within superconducting microwave circuits. AFM nano-oxidation is a valuable technique for fine-tuning the geometry and material composition of silicon phononic waveguides, thereby adjusting the mode participation in the hybrid structure. This process, similarly to what we demonstrated in Chapter 2, can be conducted in situ and real-time using the AFM nano-oxidation technique, which relaxes the strict fabrication requirements to achieve desired electromechanical coupling rates without sacrificing the high quality phonon mode.

4.2 Quality enhancement with selective oxidation

In Section 2.1, we examined how imperfections arising from the nanofabrication process affect the optical and mechanical mode resonances of optomechanical crystals. Similarly, nanofabrication induced imperfections and additional roughness on the silicon surface can severely degrade the optical quality factors. Selective oxidation of strategic locations on the OMC surface, followed by a vapor HF flash that removes the resulting silicon oxide layer, can enhance optical quality factors by reconfiguring the electric field distribution confined within the silicon. This process can be combined with real-time feedback from a non-invasive, non-contact mode AFM surface scan of the optomechanical crystal which informs the oxidation process. Furthermore, inclusion of inverse design techniques that are widely used in the field of optical metasurfaces and metamaterials [67, 68] can enhance the effectiveness of the technique as a freeform post fabrication trimming technique.

4.3 AFM poling of lithium niobate

Thin film lithium niobate (LiNbO_3) is emerged as one of the most promising materials in the field of photonics and nanomechanics with applications ranging from electro/acousto-optic modulators to ultra sensitive high frequency NEMS resonators [69, 70]. Various hybrid optomechanical and electromechanical platforms, as well as nonlinear optical platforms are demonstrated using thin film lithium niobate [71, 72]. Among its useful properties, wide range optical transparency, high piezoelectric, electro-optic, acousto-optic and pyroelectric coefficients stand out [73].

For certain applications where material platforms like lithium niobate on SOI is used, fabrication of the nanoscale features while keeping the underneath silicon surface clean and undamaged is a challenge since the widely used lithium niobate etching techniques are abrasive for silicon. On the other hand, less abrasive techniques are available, like proton exchange and hydrofluoric acid wet etching but they require tedious wet chemistry methods often not compatible with other processes or

components of the fabrication process. A promising method is electrically poling thin film lithium niobate followed by a wet hydrofluoric acid etch. Although this is a strong technique, it relies on very high voltages and smallest feature size achievable with this technique is limited and reliable fabrication of certain features is highly challenging.

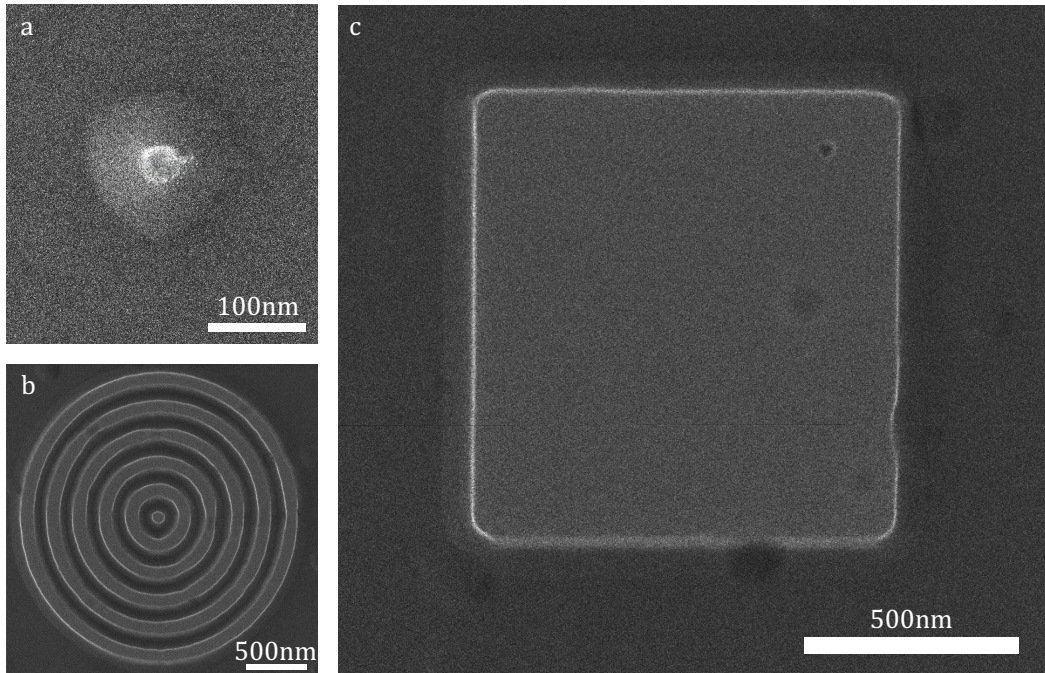


Figure 4.1: SEM image of the lithium niobate features patterned with AFM. a) A single lithium niobate pixel with a diameter of 25nm poled with conductive AFM technique and etched wet HF etch. **b)** Concentric circles with a pitch of $\sim 100\text{nm}$ poled with conductive AFM and etched with hydrofluoric acid. **c)** A lithium niobate piezo-box poled with conductive AFM and etched with hydrofluoric acid.

Conductive AFM technique promises creation of electric fields on the order of few kV/mm per V , focused on tens of nanometers. This means $\sim 10V$ applied on the tip is enough to surpass the poling threshold of $\sim 22kV/mm$ on z-cut lithium niobate thin films on silicon ($\leq 500\text{nm}$) when the device layer underneath is grounded. Using an AFM cantilever with a tip radius of 25nm , we demonstrated poling with smallest feature sizes on the order of tens of nanometers, as shown in Figure 4.1. Unpoled (+z) lithium niobate can be etched using hydrofluoric acid. This simple technique is promising for fabricating nanoscale features on lithium niobate on silicon without compromising the silicon underneath, an important requirement for lithium niobate based hybrid optomechanical crystal transducers. Moreover, features

that are not possible to realize with conventional poling techniques, like concentric circles as shown in Figure 4.1b can be easily fabricated using the proposed local poling technique.

Part II

Next-Generation Hybrid Optomechanical Crystal Microwave-Optical Transducers

OMCs in one-dimensional silicon nanobeams have been used to demonstrate MHz-scale interaction rates between single photons and phonons confined in telecom-wavelength optical and GHz-frequency acoustic modes, respectively [74]. In recent years, these devices have enabled advances in quantum acoustics [20, 75], and microwave-optical quantum transduction [27, 76–78]. In these applications, OMCs are operated at temperatures ≤ 0.1 K to ensure negligible thermal occupation in GHz frequency acoustic modes. However, optical excitation of OMCs in this temperature regime is accompanied by local heating due to weak parasitic absorption of laser light. This effect results in elevated thermal occupation and reduced coherence of the acoustic mode [20, 79], and limits the performance of OMCs as quantum memories and transducers. For instance, in the context of microwave-optical quantum transduction, operation of OMCs in the quantum coherent regime is currently possible in pulsed mode with reduced laser power, albeit at the expense of reduced efficiency for the optomechanical scattering process, and ultimately, a reduced entanglement generation rate for quantum networking applications [27, 76].

Two-dimensional (2D) device geometries [80–84] which offer increased thermal contact with the substrate are a promising approach to mitigate the detrimental effects of optical absorption-induced heating in OMCs at millikelvin temperatures. These structures rely on a phononic bandgap to protect the acoustic mode of interest from clamping losses while leveraging a larger density of states at frequencies above the gap to allow high frequency thermal phonons to escape out of the OMC cavity. However, a large thermal contact area can also lead to a significant influx of thermal phonons from sites of optical absorption external to the cavity. Such a phenomenon was noted in our prior work on 2D OMCs in Ref. [81], where optical absorption in the coupling waveguide was found to be the dominant source of thermal noise in the acoustic mode. In principle, thermal isolation of the OMC cavity from the coupling optical waveguide could be achieved through mechanical detachment of both structures from one another while maintaining evanescent optical coupling. However, these requirements are challenging to engineer in a 2D geometry since abrupt termination of the OMC can result in significantly increased optical loss via parasitic edge modes.

In Part II, we first present a 2D OMC with a side-coupled waveguide design and demonstrate a significant improvement in phonon-to-photon conversion performance over previous state-of-the-art [81]. In the last chapter, we present the design, fabrication and preliminary characterization of a 2D microwave-optical transducer.

HIGH EFFICIENCY LOW NOISE PHONON-PHOTON TRANSDUCERS

5.1 Side coupled 2D optomechanical crystal

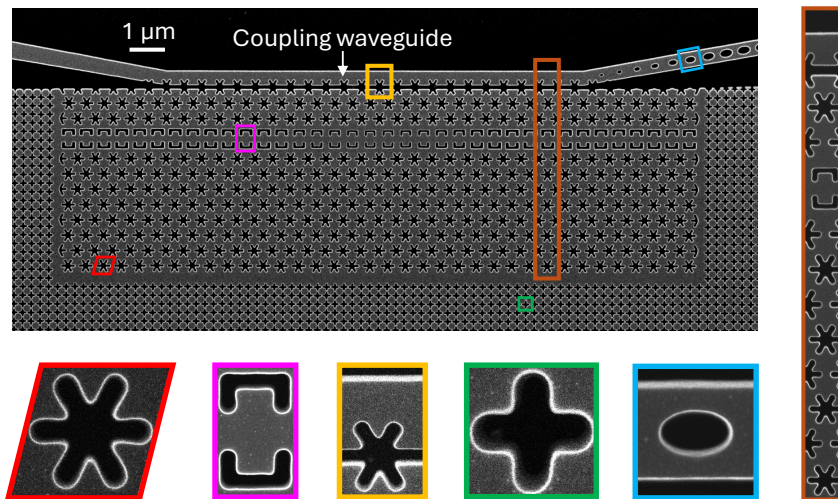


Figure 5.1: **Side-coupled 2D optomechanical crystal (OMC) cavity.** Helium-ion microscope image of a representative device with insets indicating salient features from left to right: unit cells of the 2D snowflake lattice, central fish-bone waveguide, optical coupling waveguide, and the optical waveguide mirror. The orange inset on the right shows the supercell of the geometry used to simulate optical and acoustic bandstructures.

The OMC cavity in this work is designed on a 220 nm thick silicon device layer of a silicon-on-insulator (SOI) substrate. Figure 5.1 shows a helium ion microscope image of a fabricated device. The insets show (from left to right) unitcells of snowflake, fish-bone waveguide, coupling waveguide, and the photonic crystal mirror. The snowflake crystal provides a pseudo-bandgap for TE-like optical guided waves and a full bandgap for all acoustic mode polarizations, whereas the fish-bone structure is engineered to maximize the combined photoelastic and moving boundary contributions to the optomechanical coupling. The coupling waveguide is designed with a half-snowflake unitcell to evanescently couple to the optical mode of the OMC cavity. The gap between the two structures can be controlled to set the external coupling rate of the optical cavity. To facilitate measurements of the OMC

in reflection, the coupling waveguide is terminated with a photonic crystal mirror. The orange inset on the right shows the supercell for the combined setup with the cavity and coupling waveguide. The corresponding optical bandstructure is shown in Figure 5.2a. The shaded region represents the relevant optical bandgap. The cavity (waveguide) band of interest is shown in solid red (blue). The corresponding electric field profile for cavity (waveguide) mode is shown on the right labeled 1 (2).

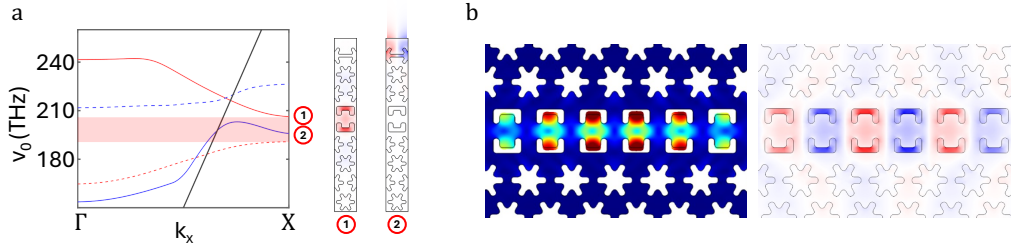


Figure 5.2: **Optical band diagram and modes of the side coupled 2D OMC.** **a**, Simulated optical bandstructure of the supercell. The solid red (blue) band has energy predominantly in the cavity (coupling waveguide). Transverse electric field profiles of these optical modes at the X-point are shown on the right. Dashed lines in the bandstructure indicate other guided modes. **b**, FEM simulations of the acoustic (left; total displacement) and optical (right; transverse electric field) modes of the 2D OMC cavity with acoustic resonance frequency, $\Omega_m/2\pi = 10.3$ GHz and optical resonance wavelength, $\lambda = 1550$ nm, respectively.

Figure 5.2b illustrates the simulated acoustic breathing mode with a frequency of 10.3 GHz, and the transverse electric field distribution of the fundamental optical mode with a wavelength of 1550 nm. The energy of the optical mode is predominantly localized in the air gaps of the fish-bone structure to enhance optomechanical coupling due to the moving boundaries. For an air gap size of 70 nm, this design provides a vacuum optomechanical coupling rate, $g_{OM}/2\pi = 1.1$ MHz in simulation. In principle, fabrication of smaller gaps (e.g. 20 nm) can allow for $g_{OM}/2\pi$ up to 2.5 MHz.

The devices are patterned using electron beam lithography and reactive ion etching, and are suspended by etching the underlying buried oxide layer with hydrofluoric acid etch. We present here the characterization of two devices, which we refer to as device I and II in our discussion. All measurements are performed in a dilution refrigerator, with the samples mounted to the mixing chamber plate at a temperature of $T_f \approx 10$ mK. The optical and acoustic mode parameters of both devices are tabulated.

Parameter	Device I	Device II
λ_0 (nm)	1553.4	1568.3
$\kappa_i/2\pi$ (MHz)	706	595
$\kappa_e/2\pi$ (MHz)	444	295
$\Omega_m/2\pi$ (GHz)	10.44	10.29
$\gamma_0/2\pi$ (kHz)	21.46	0.97
$g_{OM}/2\pi$ (kHz)	919	742

Table 5.1: **Device parameters**

The primary difference between the two devices is their coupling to the external chip environment. For device I, the intrinsic acoustic damping rate, $\gamma_0/2\pi$, is measured to be 21.46 kHz, whereas device II is better isolated from the chip environment with a $\gamma_0/2\pi = 0.97$ kHz. We attribute the difference in $\gamma_0/2\pi$ between the two devices to a difference in the as-fabricated feature sizes. The effectiveness of the snowflake acoustic bandgap region in suppressing acoustic radiation from the central cavity region, depends on the frequency alignment of the localized mode and the acoustic bandgap, and is highly sensitive to the feature size and shape. A scanning electron microscope image of device I indicates that the patterned features are slightly more rounded and extended than the ideal design, whereas device II replicates the design more faithfully. Although unintentional, these as-fabricated differences in the two devices provides further information about how they thermalize with their environment.

5.2 Measurement setup

The measurement setup used for the cryogenic measurements is shown in Figure 5.3. A fiber-coupled, wavelength-tunable external cavity diode laser is used as the pump for all measurements. A small percentage of the laser output is sent to a wavemeter (λ -meter) for wavelength stabilization. The laser is then amplified with an EDFA and then passed through a 50 MHz-bandwidth tunable fiber Fabry-Pérot filter (Micron Optics FFP-TF2) to suppress broadband spontaneous emission noise. An electro-optic phase modulator (ϕ) in the bypass path is used to generate a sideband on the laser during the locking sequence for the sideband filters on the detection path. The pre-filtered pump laser could be switched between (i) a continuous-wave measurement path, and (ii) a pulsed measurement path. On the latter path, we used two acousto-optic modulators (AOMs, G&H Photonics) in series to create optical pulses with extinction >120 dB on the pump laser. A digital delay

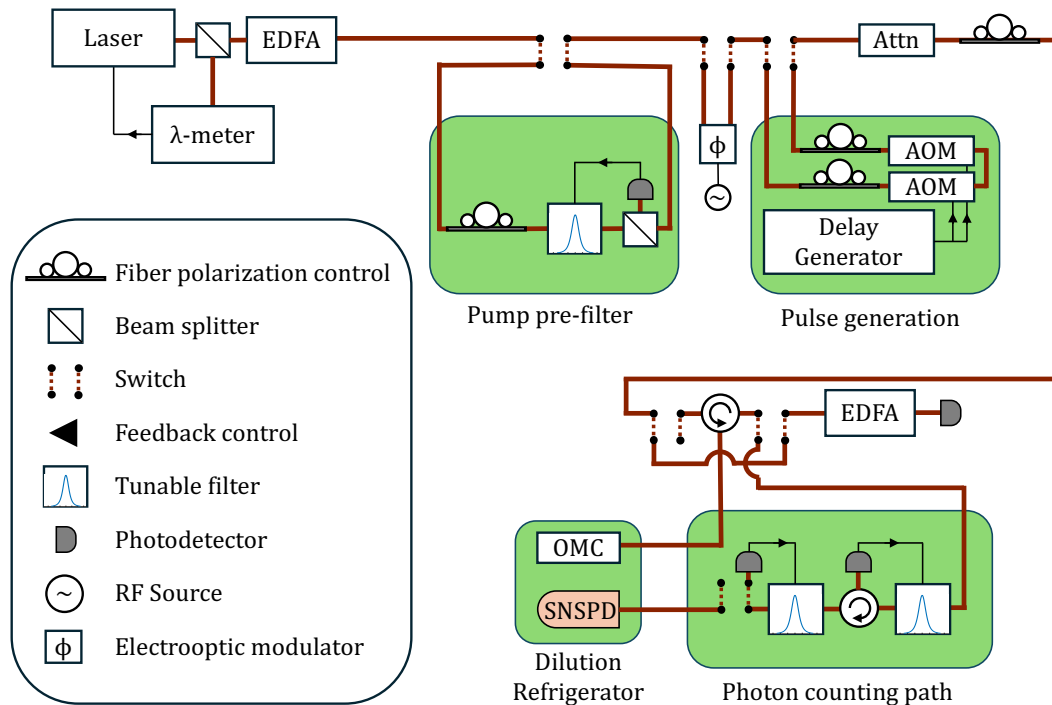


Figure 5.3: **Experimental setup:** An external cavity diode laser is used to generate the optical pump signal. A small percentage of laser power is used for wavelength locking using a wavemeter (λ -meter). The laser is then passed through an Erbium Doped Fiber Amplifier (EDFA) to amplify the power, followed by a 50 MHz-bandwidth filter. It then can be switched through an Electro-optic phase modulator (ϕ) which is used during the locking sequence of the filter-bank in the photon counting path. The laser can then be switched between two different paths: (i) Continuous wave measurements (ii) a pulsed measurements. In the pulsed measurements path, two acousto-optic modulators (AOM) in series are used for generating high-extinction optical pulses which are triggered by a delay generator. Before sending to the device in the dilution refrigerator (DF), the laser is passed through a variable optical attenuator (Attn) to adjust the optical power. Upon reflection, a circulator routes the reflected laser light to either: (i) spectroscopy photo-detectors which are used for measurements of optical and acoustic spectrum, or (ii) a photon counting path consisting of two cascaded Fabry-Pérot filters and a SPD operated at 800 mK.

generator (Stanford Research Systems DG645) is used to synchronize AOM drive pulses and trigger signals for the time-correlated single photon counting module (TCSPC, Swabian Time Tagger X).

Pump laser light is then routed via a variable optical attenuator (Attn) and a circulator into the dilution refrigerator where the sample test assembly is mounted to the mixing

chamber plate cooled down to a base temperature of 10mK. A lensed optical fiber is used to couple light into the device under test. The fiber is mounted to a three-axis nanopositioner stack (Attocube Systems) which allows for in situ alignment with respect to the optical coupler on the device. The reflected pump and signal from the device can be directed via the circulator to (i) a room-temperature photodetection path with a slow detector and a fast detector (New Focus 1554B) for optical and mechanical spectroscopy, or (ii) the single-photon counting path. On the single-photon counting path, the light is passed through two tunable, fiber-coupled Fabry-Pérot cavities (Stable Laser Systems) to suppress pump light reflected from the device. The filters have a bandwidth of 3.6 MHz, a free-spectral range of 15 GHz, and are connected in series with a fiber-optic circulator in between them. This setup provides approximately 100 dB of extinction for the pump light detuned by ~ 10 GHz from the resonance frequency.

During measurements, a locking routine is periodically used to verify that the filters are on resonance with the signal frequency. During the locking routine, we bypass the device path and generate sidebands on the pump laser by driving the EOM (ϕ) with a microwave tone at the mechanical resonance frequency of the device under test. To re-lock the filters, a sinusoidal voltage was used to dither each filter while monitoring its transmission on a slow detector. The DC offsets of the dithering signal are then changed while reducing the voltage amplitude to align the filters to the expected signal frequency from the device. After re-locking, a new round of measurements can be performed.

For single-photon counting, we used a NbN superconducting nanowire single-photon detector developed by the Jet Propulsion Laboratory (JPL). The SPD is mounted on the still plate of the dilution refrigerator at ~ 800 mK. The electrical output of the SPD is amplified by a room temperature amplifier circuit [85] and read out by a triggered single photon counting module (Swabian Time Tagger X). To minimize the dark counts on the SPD, we filter out long wavelength infrared spectrum noise by creating fiber loops before SPD with a diameter of 1.5 inches. We observed dark count rates as low as ~ 4 (c.p.s.) and a SPD quantum efficiency $\eta_{\text{SPD}} \simeq 75\%$ in our setup.

5.3 Optical absorption-induced hot bath

Previous measurements on OMC devices in the dilution refrigerator have shown that the acoustic mode thermalizes to temperatures well below 100 mK [20]. In our

study, we model this connection to the cold substrate by a coupling to a cold bath with occupancy n_f ($< 10^{-3}$), at an intrinsic acoustic damping rate, γ_0 , as shown in Figure 5.4a. Under excitation with laser fields, optical absorption-induced heating from the optical cavity and coupling waveguide are modeled by considering a hot bath at a thermal occupation, n_p (corresponding to a bath temperature, T_p), coupled to the acoustic mode at a rate γ_p . The acoustic resonator experiences optomechanical backaction at a rate, γ_{OM} . We operate our devices in a low-power optical regime where radiation pressure shot noise is negligible. When the laser is tuned to the red motional sideband of the optical cavity ($\Delta = \Omega_m$), a parametric beamsplitter interaction allows us to operate the device as a linear, bi-directional converter between quantum states in the acoustic and optical modes at a rate, $\gamma_{OM} = 4g_{OM}^2 n_c / \kappa_t$ where n_c is the intracavity photon occupation and κ_t is the total linewidth of the optical resonance [86].

As a first step towards characterizing the optical absorption-induced hot bath we operate the laser on resonance with the optical cavity ($\Delta = 0$). Under this detuning condition the electric field amplitude in the waveguide is negligible compared to the cavity, and the optomechanical backaction rate is zero. This enables us to isolate optical absorption within the cavity alone without the effects of heating due to optical absorption in the waveguide or cooling due to optomechanical backaction. We measure the heating dynamics of the acoustic mode by detecting optical photons scattered from the laser field onto a motional sideband of the optomechanical cavity. In steady state, the occupation of the acoustic mode, n_m is expected to be an average of the thermal occupations of the hot and the cold baths, weighted by the coupling rates of the acoustic mode to the respective baths, as given by the relation,

$$n_m = \frac{\gamma_p n_p + \gamma_0 n_f}{\gamma_p + \gamma_0}. \quad (5.1)$$

Figure 5.4b shows the schematic of the measurement setup for n_m . We send laser pulses with pulse duration, $\tau_d = 50 \mu\text{s}$ at a repetition rate, $R = 1 \text{ kHz}$, to the device in the dilution refrigerator via a circulator. The optical signal reflected from the device is directed to a Fabry-Pérot filter setup which suppresses the pump pulses and transmits photons generated on the motional sideband of the optomechanical cavity to a superconducting nanowire single photon detector. Figure 5.5a shows the time-dependent occupation of the acoustic mode measured from heating induced by a square laser pulse with a peak power corresponding to $n_c = 385$. The rate of increase in the occupation is used to infer $\gamma_p + \gamma_0$, whereas the steady state

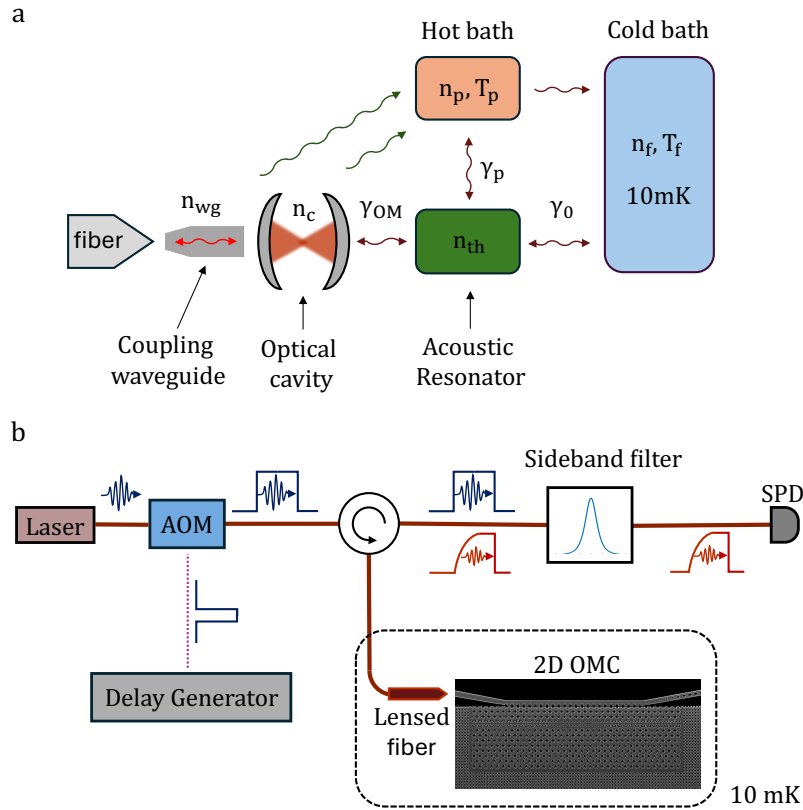


Figure 5.4: **Model and measurement scheme for optical absorption-induced hot bath.** **a)** Schematic showing interactions of the acoustic resonator with various baths considered in our heating model. **b)** Schematic of measurement setup for time-resolved measurements of the hot bath using single-photon counting on the optical sideband generated by thermal motion of the acoustic resonator.

occupation is used to infer n_m . Finally, the value of γ_0 is measured independently from ringdown measurements [20], thereby allowing us to extract the parameters, γ_p and n_p of the hot bath from Equation 5.1.

Figure 5.5b shows n_p as a function of n_c for devices I and II along with results from similar measurements performed previously on 1D OMCs [20], and butt-coupled 2D OMCs [81]. The vertical axis on the right represents the corresponding bath temperature T_p . The solid lines around the experimental data points for devices I and II are fits to the power law, $n_p = An_c^k$. We find that the fits to the hot bath occupancies for device I and II are $2.2 \times n_c^{0.31}$ and $2.9 \times n_c^{0.21}$, respectively. For comparison, we have also shown the fits to $n_p(n_c)$ for previously measured butt-coupled 2D OMC (purple solid line) and 1D OMC (green solid line) devices, corresponding to

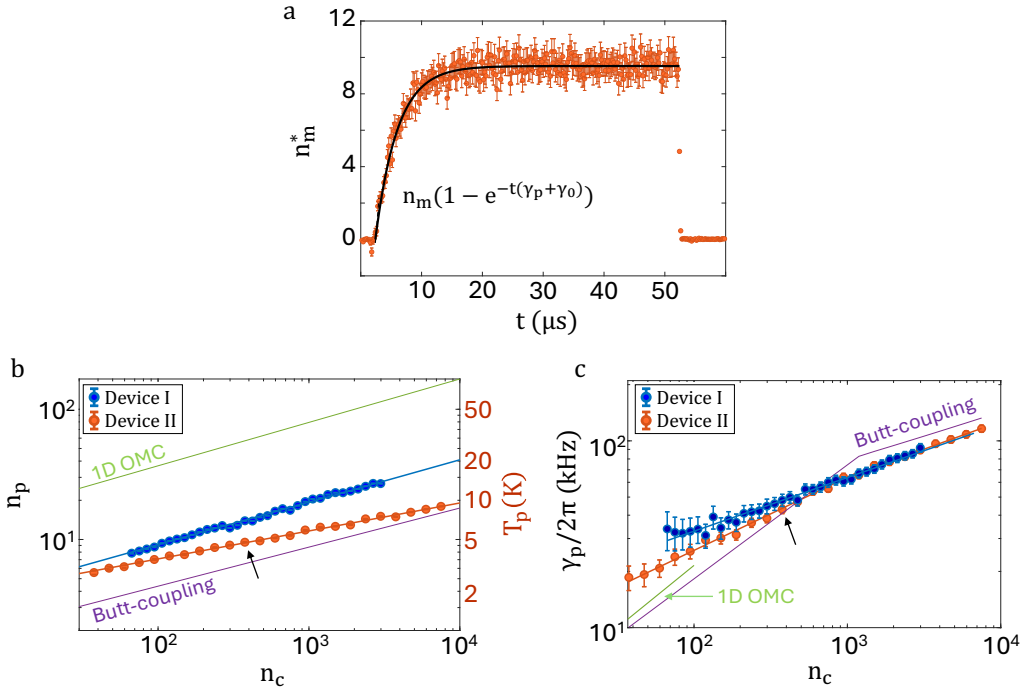


Figure 5.5: Characterization of optical absorption-induced hot bath. **a)** Measurement of the transient thermal occupation of the acoustic resonator, n_m^* in response to a rectangular optical pulses on resonance with the optical cavity (pulse duration $\tau_d = 50 \mu\text{s}$, repetition rate, $R = 1 \text{ kHz}$, and peak intracavity photon occupation, $n_c = 385$). The black line represents an exponential fit to the observed data with the characteristic rate, $\gamma_p + \gamma_0$, and steady-state thermal occupation, n_m . Here γ_0 is the intrinsic damping rate of the acoustic resonator and γ_p is the coupling rate to the optical-absorption-induced hot bath. **b)** Thermal occupation of the hot bath, n_p estimated from measurements of n_m performed at varying optical power, shown on the x-axis in units of peak intra-cavity photon occupation, n_c . For comparison, n_p curves for 1D-OMC [20], butt-coupled 2D OMC [81] are shown. **c)** Variation of $\gamma_p/2\pi$ with n_c . The data point marked with an arrow in panels (b) and (c) corresponds to the data in panel (a) for $n_c = 385$.

$1.1 \times n_c^{0.3}$ and $7.94 \times n_c^{0.33}$, respectively. As expected, the thermal conductance seems to be highest for the butt-coupled 2D OMC, slightly lower for the side-coupled 2D OMC devices that are restricted to approximately the half-plane, and lowest for the 1D OMCs. Of note, the power law of the side-coupled device II of this work ($k = 0.21$), deviates from other measured 1D and 2D OMCs, and does not seem to follow from the simple phonon-bottleneck model of Ref. [20]. This suggests there may be more to the underlying conductance of heat from these structures. While a systematic study of this effect is beyond the scope of this article, we note that

previous studies on phononic crystal structures have observed varying power laws for thermal conductance [87], and disorder dependent thermal conductance [88, 89], which may offer insights into the observed n_p power laws in this work.

Figure 5.5c shows the variation of γ_p with n_c . For device II, we find the power-law, $\gamma_p/2\pi = 4.3 \text{ (kHz)} \times n_c^{0.39}$ when $n_c < 1000$ and $\gamma_p/2\pi = 8.25 \text{ (kHz)} \times n_c^{0.29}$ when $n_c > 1000$. The power-law exponent of 0.39 in the regime of low optical power is significantly different from 0.6 and 0.66 observed previously for butt-coupled 2D OMC and 1D-OMC devices, respectively. This reduction can be explained by the reduced n_p power exponent of 0.21, together with a two-dimensional phonon bath.

For device I, in the regime of high optical power with $n_c > 1000$, $\gamma_p/2\pi = 8.7 \text{ (kHz)} \times n_c^{0.29}$. For $n_c < 1000$, the measurement error on γ_p for device I is larger due to a higher intrinsic damping rate, γ_0 , thereby reducing the reliability of a fit in this regime. We observe that the power-law exponent for γ_p in the regime of high optical power is identical for devices I and II in this study, and also in close agreement with the butt-coupling geometry.

5.4 Continuous wave phonon-photon transduction

After characterizing the optical-absorption-induced hot bath, we test the device with the laser tuned to the red motional sideband of the optical cavity ($\Delta = \Omega_m$), relevant for phonon-photon transduction. The thermal occupation of the acoustic mode, n_{th} , due to optical-absorption-induced heating adds finite noise to any transduced signal. Other performance metrics of interest for such a transducer are the conversion efficiency, η_{OM} , and bandwidth, γ_m . In continuous-wave operation, the conversion efficiency is given by $\eta_{OM} = \frac{\gamma_{OM}}{\gamma_{OM} + \gamma_0 + \gamma_p}$. We calibrate γ_{OM} for different n_c using electromagnetically induced transparency [3]. Due to the low γ_0 in our devices, we expect high conversion efficiency for modest values of n_c . Specifically, operation at $n_c \approx 13$ and 3 is expected to yield $\eta_{OM} \approx 50\%$ in devices I and II, respectively. The bandwidth of the transducer is limited by the total acoustic linewidth, which is dominated by the optomechanical backaction $\gamma_m \approx \gamma_{OM}$ in the regime of high conversion efficiency.

To characterize the transducer-added noise under continuous-wave laser excitation, we use the measurement setup shown schematically in Figure 5.6a, where we perform single-photon counting at the optical cavity resonance frequency. The data in Figure 5.7 show n_{th} measured with varying n_c for devices I and II, respectively. In the high power regime, specifically for $n_c > 500$, the n_{th} data has been corrected for the

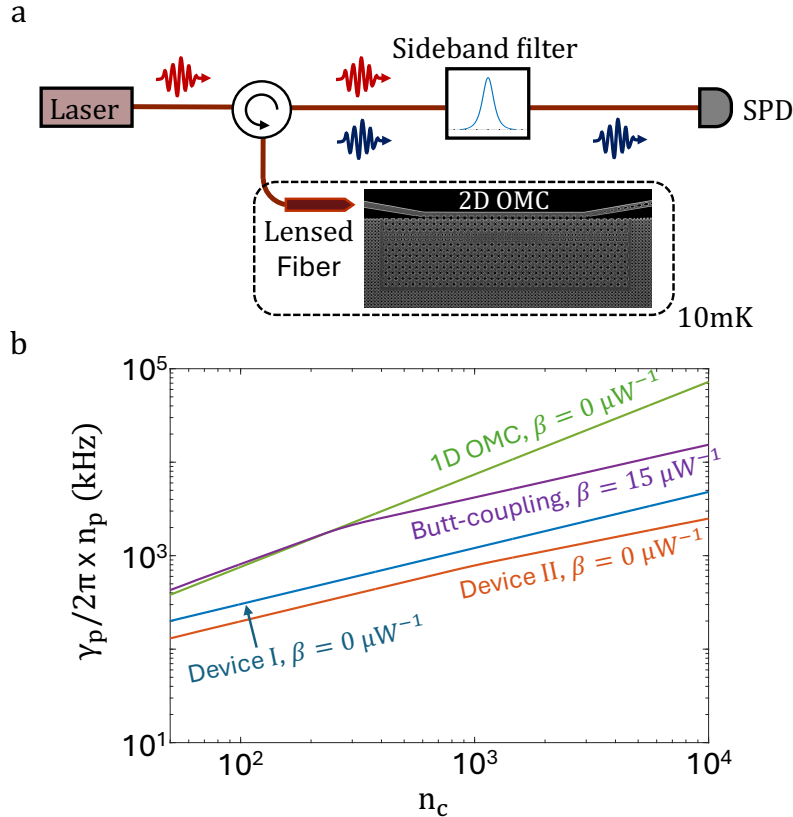


Figure 5.6: **Phonon-to-photon transduction under continuous-wave excitation.** **a)** Schematic of measurement setup showing single-photon counting of up-converted photons at the optical resonance frequency with the OMC pumped continuously on the red-detuned sideband ($\Delta = \Omega_m$) of the optical resonance. **b)** Estimated heating rate of the acoustic resonator $\gamma_p n_p / 2\pi$ as a function of n_c under $\Delta = \Omega_m$ for different devices plotted for their measured value of β .

limited bandwidth of the sideband filter when the acoustic bandwidth γ_m starts to approach the sideband filter linewidth (see Appendix B for details). The top x-axis displays the corresponding γ_{OM} for side-coupled devices. The green and purple curves in these panels show results from similar measurements of thermal occupancy of the acoustic mode performed previously on 1D OMCs [20] and butt-coupled 2D OMCs [81]. We observe that side-coupled 2D OMCs allow for lower thermal noise across a wide range of input optical powers. A minimum n_{th} of 0.28 ± 0.01 is achieved for device I at $n_c = 2030$, corresponding to an optomechanical transduction efficiency of $98.6 \pm 0.2\%$, and a bandwidth of $\gamma_{OM}/2\pi \approx 6$ MHz.

We model the thermal occupancy n_{th} using the heating model introduced in the

previous section. However, in contrast with the measurements with $\Delta = 0$ in the previous section, the majority of the incident power is reflected under detuned operation with $\Delta = \Omega_m$, and parasitic optical absorption in the coupling waveguide can contribute substantially to the hot bath. To include this effect in our heating model, we define an effective photon occupation associated with coupling waveguide, n_{wg} , varying linearly with the input power as $n_{\text{wg}} = \beta P_{\text{in}}$ for some fixed constant, β and the input power, P_{in} . We then add the contributions from both cavity and waveguide components and define the parameters of the modified hot bath as $n_p[n_c, \beta] \rightarrow n_p[n_c + \beta P_{\text{in}}]$, and similarly for γ_p . The thermal occupation of the acoustic mode is then given by

$$n_{\text{th}} = \frac{\gamma_p[n_c, \beta]n_p[n_c, \beta] + \gamma_0 n_f}{\gamma_p[n_c, \beta] + \gamma_0 + \gamma_{\text{OM}}[n_c]}. \quad (5.2)$$

For small n_c , Equation 5.2 is dominated by heating from the hot bath $\gamma_p n_p$ and exhibits an increase in n_{th} with increasing n_c . Conversely for large n_c , n_{th} decreases with increasing n_c as a consequence of backaction cooling γ_{OM} . The turnaround point between these two regimes is influenced by parasitic optical absorption in the coupling waveguide. For example, the solid blue and orange curves in Figures 5.6b and c show the predicted thermal phonon occupancy if the waveguide-heating contribution, β were set to zero. We see that the experimental data from both devices I and II is in reasonable agreement with the $\beta = 0$ curves. This indicates that waveguide-related heating is negligible in side-coupled 2D-OMC geometry. In comparison, for the butt-coupled 2D OMCs, β was measured to be $15 \mu\text{W}^{-1}$ [81].

While n_{th} in Equation 5.2 depends on the optomechanical device parameters γ_0 and γ_{OM} , improvements purely based on geometric modifications of the device platform under detuned operation $\Delta = -\Omega_m$ can be studied using the heating rate, $\gamma_p n_p / 2\pi [n_c, \beta]$, and is plotted in Figure 5.7 for various devices.

For 1D-OMC, the heating rate scales linearly ($\gamma_p n_p \propto n_c$), similarly to the cooling rate ($\gamma_{\text{OM}} \propto n_c$), which results in the saturation of n_{th} to a few phonon levels as n_c increases. 2D geometries are expected to have lower magnitude of the heating rate due to larger thermal contact with the cold bath. However, due to a large $\beta = 15 \mu\text{W}^{-1}$, the butt-coupling design exhibits almost identical heating performance ($\gamma_p n_p \propto n_c^{0.9}$) to that of 1D-OMC for $n_c < 300$, and only becomes sublinear for $n_c > 300$ ($\gamma_p n_p \propto n_c^{0.6}$). In contrast, for side-coupled geometries, the heating rate scales sub-linearly ($\gamma_p n_p \propto n_c^{0.6}$) for all n_c range measured and has a lower

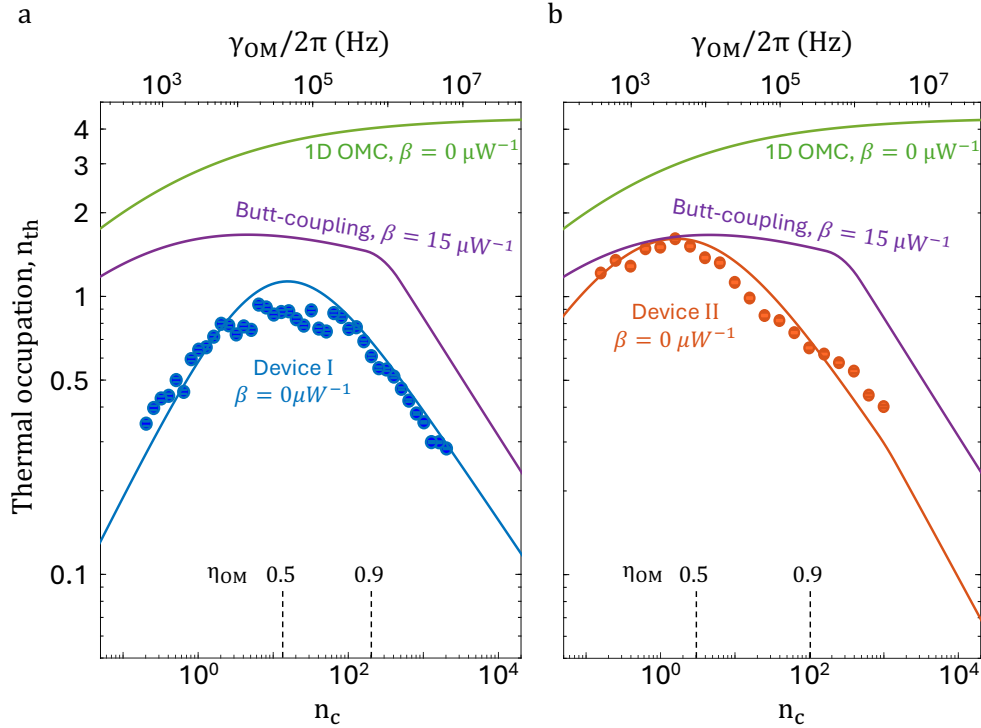


Figure 5.7: n_c vs n_{th} . Measured thermal phonon occupancy, n_{th} with varying optical power, shown on the bottom x-axis in units of intra-cavity photon occupation, n_c , and on the top-axis in units of optomechanical transduction rate, γ_{OM} . Results are shown on separate charts for **a)** device I, and **b)** device II. Filled circles are data points whereas the solid line indicated with $\beta = 0 \mu W^{-1}$ is the modeled n_{th} dependence using Equation 5.2. For comparison, model curves are shown for a butt-coupled 2D-OMC ($\beta = 15 \mu W^{-1}$) [81], and 1D-OMC [20]. Dashed lines indicate the n_c value for optomechanical transduction efficiency $\eta_{OM} = 50\%$ and 90% . For $n_c = 1$, on chip input power for device I and II are $P_{in} = 0.20 \mu W$, and $0.28 \mu W$, respectively.

magnitude. Specifically, for device II, the heating rate is reduced by approximately six-fold compared to the butt-coupling design for $n_c > 300$.

5.5 Pulsed phonon-photon transduction

Pulsed transduction schemes are often preferred due to the delayed heating response of the acoustic resonator [79], which allows for the initialization of the optomechanical transduction pulse prior to the onset of heating. We characterize the performance of side coupled 2D-OMC as a transducer in pulsed mode by sending short rectangular pulses on red sideband. A pulse duration of $\tau_d = 500$ ns is selected to account for the finite rise time of the sideband filters (≈ 200 ns). The transduction efficiency

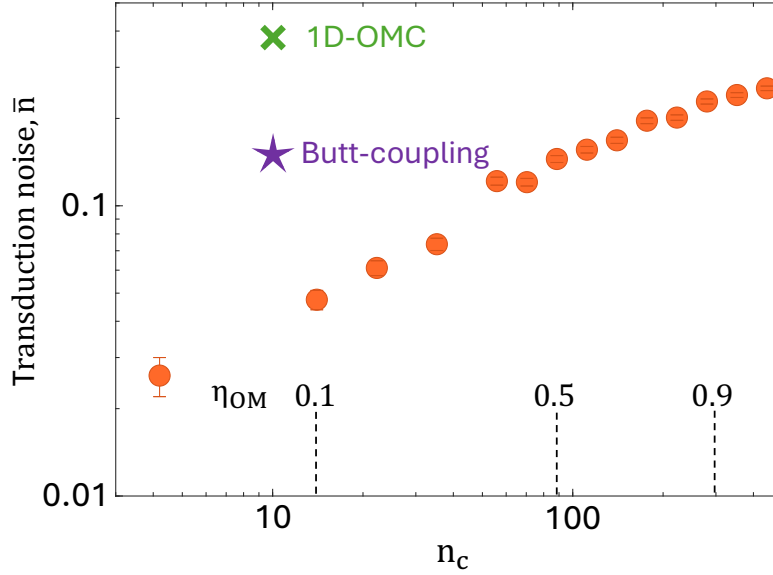


Figure 5.8: **Phonon-to-photon transduction under pulsed laser excitation.** Internal added noise, \bar{n} (red data points) as a function of the peak intra-cavity pump photon number, n_c . All noise measurements are performed on device II with rectangular optical pump pulses with a pulse width of 500 ns at a repetition rate of 250 Hz. For comparison, \bar{n} is shown for Butt-coupling design [81], and 1D-OMC [20]. Dashed lines indicate the n_c value for transduction efficiency $\eta_{OM} = 10\%$, 50% , and 90% for device II. For $n_c = 1$, on chip input power is $P_{in} = 0.28 \mu\text{W}$.

in the pulsed mode is given by

$$\eta_{OM} = \frac{\gamma_{OM}}{\gamma_{OM} + \gamma_0 + \gamma_p} \left(1 - e^{-(\gamma_0 + \gamma_p + \gamma_{OM})\tau_d} \right), \quad (5.3)$$

Figure 5.8 shows the internal transduction noise \bar{n} for device II in pulsed scheme along with similar measurements performed previously on 1D-OMC [20] and butt-coupling design [81] at $n_c = 10$. The n_c value corresponding to the optomechanical conversion efficiency $\eta_{OM} = 10\%$, 50% , and 90% for device II are indicated with dashed lines. Given the low intrinsic linewidth of the acoustic resonator for this device ($\gamma_0/2\pi = 0.97$ kHz), we used a repetition rate of 250 Hz to allow the acoustic mode to sufficiently thermalize to the cold bath between successive optical pulses. For the highest optical power we could send to the device ($n_c = 444$), we measured $\bar{n} = 0.25 \pm 0.01$ which corresponds to a transduction efficiency of $\eta_{OM} = 93.1 \pm 0.8\%$. This constitutes a significant enhancement across transduction metrics over 1D-OMC with $(n_c, \bar{n}, \eta_{OM}) \simeq (10, 0.4, 4\%)$ [20].

5.6 Discussion

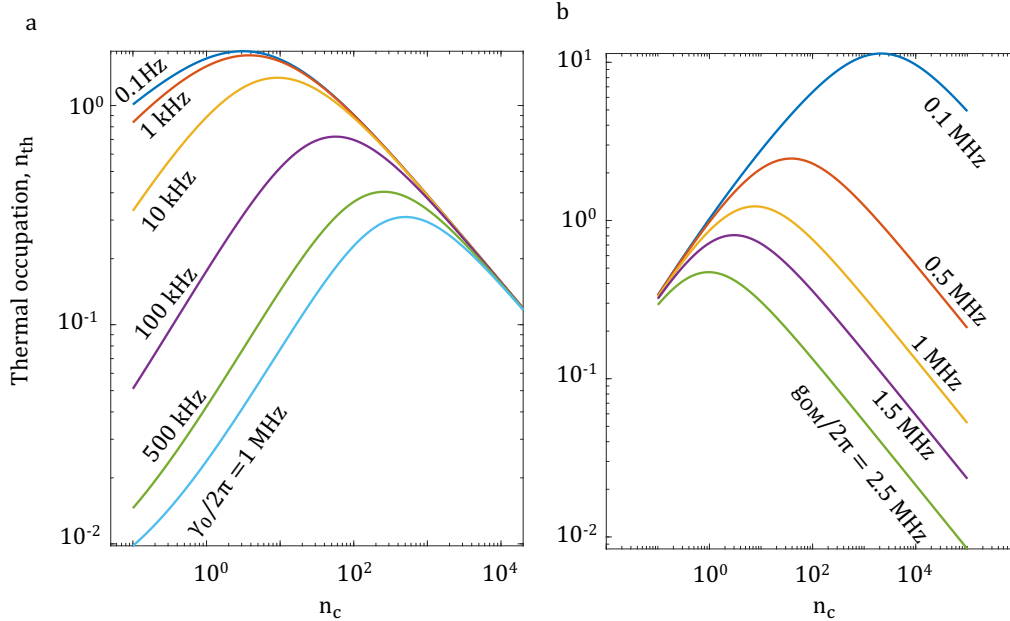


Figure 5.9: **Thermal occupation for various device parameters.** **a)** n_{th} as a function of n_c for various $\gamma_0/2\pi$. Increasing $\gamma_0/2\pi$ improves thermalization of the breathing mode to the cold bath (10 mK) dictated by Equation 5.2, which leads to reduction in n_{th} . **b)** n_{th} as a function of n_c for various $g_{OM}/2\pi$. The ‘turnaround’ point shifts to lower n_c with increasing g_{OM} . For both (a) and (b), device parameters are assumed to be same as that for device I.

We extend our model for thermal occupation n_{th} governed by Equation 5.2 for various device parameters. Figure 5.9a shows n_{th} vs n_c plot for various intrinsic linewidth of mechanics $\gamma_0/2\pi$. With increasing linewidth, the breathing mode thermalizes better with 10 mK bath temperature with occupancy $n_f < 10^{-3}$, thereby reducing n_{th} in the low n_c regime. Figure 5.9b shows n_{th} vs n_c plot for various $g_{OM}/2\pi$. In the low power regime ($n_c < 1$), n_{th} does not show significant difference. However, the ‘turnaround’ point above which the backaction becomes dominant, shifts to lower n_c values with increasing $g_{OM}/2\pi$. In the high n_c regime, the n_{th} shows a significant reduction in amplitude with increasing $g_{OM}/2\pi$. The parameters ($\kappa_i, \kappa_e, n_p, \gamma_p$) in both Figure 5.9a and b are taken from device I. In this analysis, we assume that the optical absorption-induced hot bath will remain independent of the smallest gap size, $h_0 - h_i$, hence $g_{OM}/2\pi$. This is because the optical mode of interest is an ‘air-mode’, where a large fraction of the optical energy is localized within the air holes of the C-shape structure. Reducing the gap size will increase the energy

concentration within the air gaps but is not expected to substantially alter the optical absorption in silicon. For instance, FEM simulations show that when $h_0 - h_i = 60$ nm, the participation of the optical energy within silicon is approximately 13%. In contrast, for $h_0 - h_i = 20$ nm, the participation increases only slightly to 17%.

Parameter	1D-OMC [20]	2D-OMC (device II)
n_c	10	443
η_{OM}	4%	93%
\bar{n}	~ 0.4	0.25
peak $\gamma_{OM}/2\pi$	13 kHz	1.1 MHz
Single photon heralding rate ($R=10$ kHz, $\eta_{ext} = 5\%$)	20 Hz	465 Hz
Photon coincidence rate	0.04 Hz	21 Hz

Table 5.2: **Comparison of figures of merit for pulsed transduction:** η_{OM} is the phonon-to-photon transduction efficiency. \bar{n} is the measured noise in the transduction process. Single photon heralding rate is estimated for repetition rate $R=10$ kHz and detection efficiency $\eta_{ext} = 5\%$. The coincidence rate is the estimated for a two-node remote entanglement scheme.

Parameter	1D-OMC [20]	2D-OMC (device II)
n_c	569	641
η_{OM}	$\approx 93\%$	$\approx 97\%$
n_{th}	4.2	0.42
$\gamma_{OM}/2\pi$	1 MHz	1.6 MHz

Table 5.3: **Comparison of figures of merit for continuous-wave transduction**

Table 5.2 shows a comparative analysis between 1D-OMC (device A in [20]) and 2D-OMC (device II in this work) for phonon-photon pulsed transduction. For both measurements, the repetition rate is much smaller than the intrinsic decay rate of the acoustic resonator ($R \ll \gamma_0$) which allows for thermalization with the fridge environment between subsequent optical pulses. For a fair comparison of the single photon heralding rate, we assume a common repetition rate $R=10$ kHz and total detection efficiency $\eta_{ext} = 5\%$ for both 1D-OMC and 2D-OMC. The resulting single photon heralding rate for 1D-OMC is $R \times \eta_{ext} \times \eta_{OM} = 20$ Hz with an added noise of $\bar{n} \sim 0.4$. For 2D-OMC, the single photon heralding rate is 465 Hz with an added noise of 0.25. The photon coincidence rate for a remote entanglement experiment involves two nodes and will scale as square of the detection efficiency. For 1D-OMC, this rate is significantly smaller ($R \times \eta_{ext}^2 \times \eta_{OM}^2 = 0.04$ Hz); whereas

the photon coincidence rate for 2D-OMC in this work is 21 Hz, which constitutes a ~ 500 -fold improvement along with lower added noise.

In case of continuous wave transduction, the figures of merit for different devices are shown in Table 5.3. The data for 1D-OMC is taken for device I in [20]. The transduction efficiency η_{OM} in continuous wave is given by $\gamma_{\text{OM}}/(\gamma_{\text{OM}} + \gamma_0 + \gamma_p)$ which remains greater than 90% for $\gamma_{\text{OM}} \gg \gamma_0$. The thermal occupation of the acoustic resonator shows an order of magnitude improvement for device II in this work ($n_{\text{th}} = 0.42$), compared to 1D-OMC ($n_{\text{th}} = 4.2$) at similar n_c levels.

The side-coupled 2D-OMC design presented here reduces optical absorption-induced thermal noise in OMCs, a major obstacle in quantum application requiring operation at millikelvin temperatures. We anticipate that further reduction in thermal noise can be achieved through surface passivation techniques [90], potentially minimizing optical absorption via surface defect reduction.

This result unlocks new possibilities for more quantum-coherent applications using OMCs. The compact form factor and long-lived acoustic mode of such devices are attractive for applications such as quantum memory for telecom photons [75]. While we achieved a low intrinsic decay rate of 0.97 kHz for the acoustic resonator, we anticipate that embedding the 2D-OMC in a cross phononic shield may lead to drastically lower intrinsic decay rates [20, 81]. The low thermal occupation of the acoustic resonator presents an opportunity to investigate two-level systems (TLS) in amorphous solids [20, 91, 92], further expanding the potential of OMCs in quantum technologies.

The improved performance of our side-coupled 2D-OMC design in pulsed operation promises significant advancements in single-photon heralding and remote entanglement generation. For a realistic pulse repetition rate of 10 kHz and a total detection efficiency of 5%, we estimate a single-photon heralding rate of 465 Hz, a substantial increase compared to the 20 Hz achievable with 1D-OMCs. Furthermore, in a two-node remote entanglement experiment, we project a photon coincidence rate of 21 Hz, representing a ~ 500 -fold enhancement over the 0.04 Hz rate achievable with 1D-OMCs.

In the context of microwave-optical quantum transduction, side-coupled 2D-OMC could be integrated into piezo-optomechanical transducers by designing a piezo-acoustic cavity that couples the electrical circuit to the optomechanical circuit through a phononic waveguide [93]. Such transducers offer the potential for large-

bandwidth, low-noise, and near-unity efficiency conversion between microwave and optical signals. While this study has focused on improved thermal handling in silicon-based devices, piezo-optomechanical transducers utilize heterogeneously integrated platforms with optically robust microwave resonators [27, 77, 78], potentially involving distinct heating mechanisms. Nevertheless, our findings establish a performance benchmark for microwave-optical transduction. By connecting such a transducer to an off-chip qubit module [63, 94, 95], high optical powers can be employed without compromising superconducting qubit coherence. Additionally, using the AFM nano-oxidation tuning technique we introduce in Part I can be used to precisely match frequencies between remote piezo-optomechanical systems, paving the way for optically mediated remote entanglement of superconducting qubit nodes.

Chapter 6

HYBRID 2D OMCS FOR MICROWAVE-OPTICAL TRANSDUCTION

In the previous chapter, high-efficiency, low-noise photon–phonon transduction using side-coupled 2D optomechanical crystals was presented. These engineered nanostructures enable strong interactions between localized optical and mechanical modes, while minimizing heating through the optical coupler and ensuring strong thermalization to the thermal bath. Together, these features allow operation at high intracavity optical photon numbers, enabling photon–phonon conversion with high efficiency while maintaining thermal phonon occupation well below unity, effectively breaking the conventional efficiency-noise trade-off. These advantages make side-coupled 2D OMC-based transducers strong candidates for realizing the next generation of efficient microwave-optical transducers for quantum networks.

In this chapter, the design, fabrication, and preliminary testing of a side-coupled hybrid 2D optomechanical crystal-based microwave-optical transducer will be presented.

6.1 Design of the hybrid 2D OMC transducer

Our microwave-optical transducer follows the basic hybrid optomechanical transducer scheme discussed in Chapter 1, that accommodates an optical cavity and a microwave resonator interfaced with a mechanical mode coupled to each cavity. In the case of 2D OMC transducer, cavity \hat{a} is the silicon optical crystal while the superconductive microwave resonator is denoted as \hat{c} and finally \hat{b} denotes the mechanical mode. Our design, much like previous examples of piezo acoustic OMC based microwave-optical transducers, leverages a mechanical mode hybridized between the optomechanical crystal and the piezo-acoustic resonator of the hybrid transducer to mediate the transduction. This way, the superconductive resonator can be spatially separated from the optical crystal and optical modes with high quality factors can be maintained while the participation of the mechanical mode into each cavity can be fine tuned.

In the following subsections, we introduce the three main components of the 2D OMC transducer: the side-coupled 2D optomechanical crystal, aluminum nitrate

on silicon piezo-acoustic cavity, and light robust niobium nitrate superconducting microwave resonator.

Side-coupled 2D optomechanical crystal with phonon waveguide

Side coupled 2D optomechanical crystal, as we studied in Chapter 5, is the element where the conversion between optical photons and microwave frequency phonons takes place. In the pure 2D OMC case, ‘C shape’ region encapsulating the mode volume is designed to have band gaps¹ for both optical and mechanical modes. In the case of 2D OMC transducer however, we need the mechanical mode to be ‘leaky’ to enable mechanically hybridized optomechanical and piezo-acoustic cavity phonon modes, hence the implementation of the previously designed pure optomechanical geometry into the transducer design requires certain modifications.

The modified 2D OMC consists of three regions: the mirror, defect, and phonon waveguide regions (see Figure 6.1a). The mirror region provides simultaneous optical and mechanical band gaps while the defect region is formed by the adiabatic change in the *C shape* dimensions of the fish bone region that is responsible for the localization of the modes. The phonon waveguide allows for the propagation of the breathing-like phonon mode of interest while still providing an optical bandgap. *C shape* dimensions adiabatically shrank/enlarged after the cavity region to create a phonon waveguide while keeping the same silicon/vacuum ratio to achieve optical band gap. Since the optical modes are more sensitive to the effective refractive index of the combined medium rather than the shape, different forms of vacuum pockets can be used to achieve similar effective refractive index within unit cells dictated by the volume ratio of the contributing media and still preserve the band gap.

The phonon waveguide designed for the leaky optomechanical crystal experiences unwanted losses due to the emergence of out-of-plane mechanical modes that couple to the mode of interest. To address this issue, we increased the dimension w_o , outer width of the *C shape*, that eliminates the thin tethers connecting the phonon waveguide to the snowflake region (see Figure 6.1b). The resulting standalone one-dimensional phonon waveguide section acts as a filter for out-of-plane symmetry modes, thereby reducing the associated losses. Mechanical mode spectrum of the designed structure is shown in Figure 6.1e. The mechanical mode exhibiting the highest optomechanical coupling rate with $g_{OM}/2\pi \sim 950kHz$ is highlighted with red and normalized displacement is shown in Figure 6.1d.

¹Pseudo band gap for the mechanical mode since certain symmetry axes have modes in the bandgap [81].

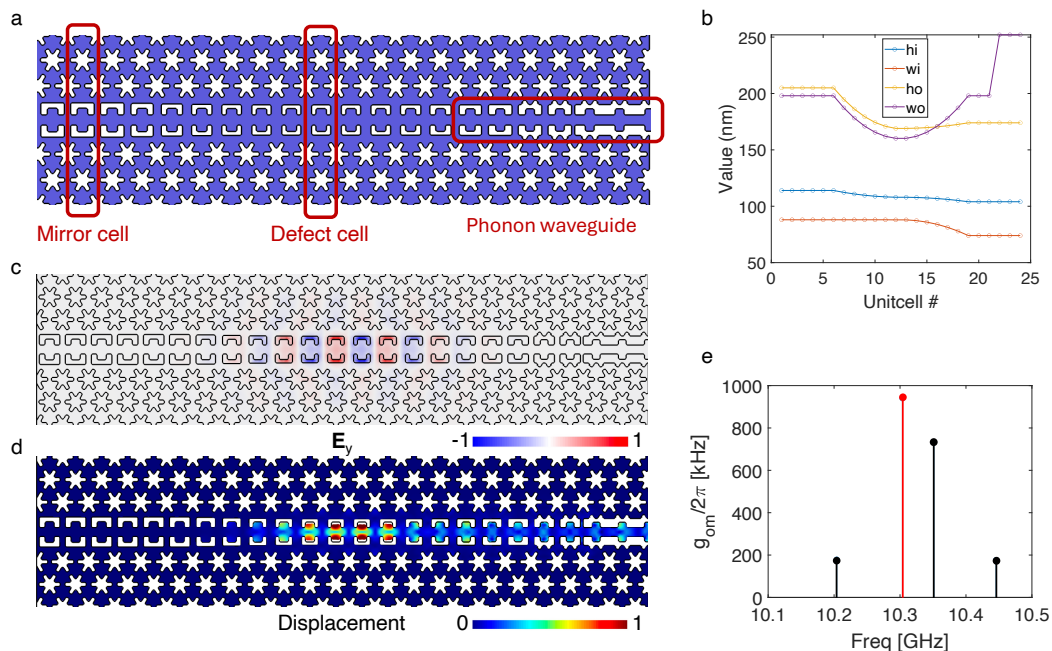


Figure 6.1: **Side-coupled 2D OMC with phonon waveguide.** **a)** Design of the asymmetric 2D OMC with photon/phonon mirror on the left side and photon mirror/phonon waveguide on the right side. **b)** Critical dimensions of the unit cells of the 2D OMC with phonon waveguide. **c)** Electric field distribution of the optical mode of interest at around 1550nm. **d)** Normalized displacement of the mechanical mode of interest with high single photon optomechanical coupling rate $g_{OM}/2\pi$. **e)** Single photon optomechanical coupling rate $g_{OM}/2\pi$ for the modes around 10.3 GHz. Mode of interest with highest $g_{OM}/2\pi$ is shown with red.

Light is coupled into the hybrid optomechanical crystal using a lensed fiber and an end-fire coupler. The end-fire coupler is connected to a millimeter-long waveguide, allowing us to position the transducer away from the lensed fiber. This separation helps protect the sensitive superconducting resonator from stray light fields.

Aluminum nitride on silicon piezo-acoustic cavity

Piezoelectricity is a phenomenon that arises from the lack of centrosymmetry in a crystal's unit cell. Due to the absence of inversion symmetry in their crystal lattice, piezoelectric crystals generate electric charge in response to mechanical strain, or undergo deformation when an electric potential is applied. In our design, we utilize aluminum nitride (AlN)—a strongly piezoelectric material that can be relatively easily fabricated as a thin film—to enable conversion between microwave phonons and microwave photons.

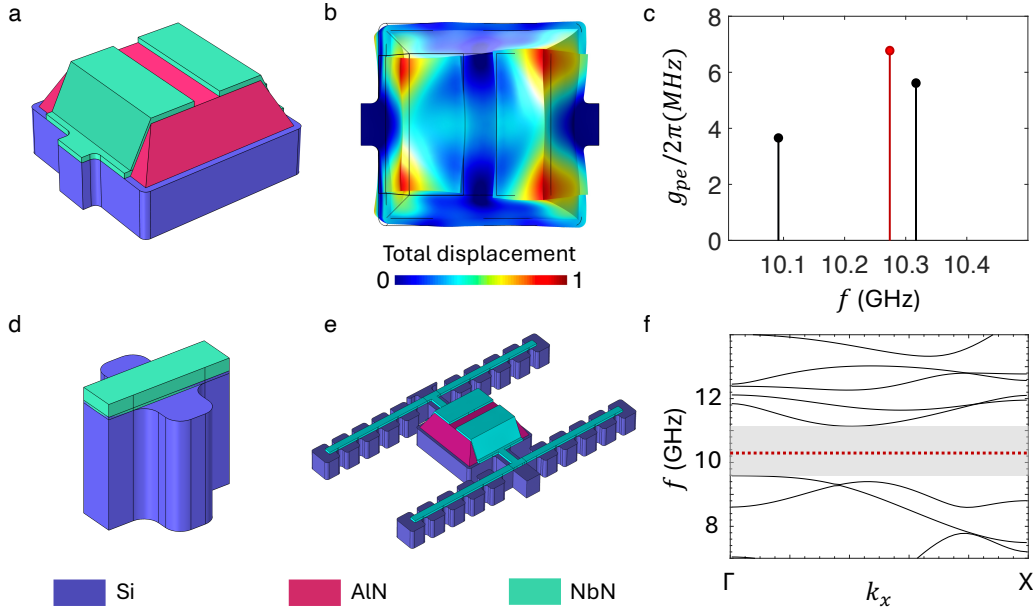


Figure 6.2: **Piezoacoustic cavity with phononic shield.** **a)** AlN piezo-box over the silicon base shown with the NbN electrodes deposited on top. **b)** Total displacement profile of the piezo-box mode of interest. **c)** High piezo electric coupling modes of the shown piezo-box design. Mode of interest is shown in red. **d)** A unit cell of phononic shield optimized to have a bandgap around 10.3GHz. **e)** Full piezoacoustic cavity geometry including the 5 periods of phononic shield. **f)** Band diagram of the designed phononic shield showing a bandgap of ~ 1.5 GHz centered around 10.3 GHz. Frequency of the mode of interest is indicated with the red dashed line.

Piezo-acoustic cavity consisting of a 200nm thick *c*-cut AlN *piezo-box* over 220nm silicon device layer is shown in Figure 6.2. The stack is connected to the bulk by a pair of 5 period long one dimensional phononic shield that exhibit a band gap around 10.3GHz to achieve high mechanical quality factor phonon modes (see Figure 6.2e,f). AlN-Si stack is metallized with a 25nm thick niobium nitride (NbN) thin film layer that is connected to the bulk over the phononic shield. Niobium nitride over the AlN piezo-box is patterned to form a pair of electrodes designed to overlap the applied electric field and the mechanical strain distribution of the mechanical mode of interest of the AlN-Si stack which is crucial to maximize the piezoelectric coupling g_{pe} . Piezoelectric coupling is given by

$$g_{pe} = \frac{\omega_m}{4\sqrt{2U_m U_q}} \int \mathbf{D}_m \cdot \mathbf{E}_q dV \quad (6.1)$$

Where ω_m is the mechanical frequency, U_m and U_q are the total mechanical and electrostatic energies, respectively. The dot product in the integral accounts for the overlap between the mechanically induced electric displacement field \mathbf{D}_m and single photon electric field \mathbf{E}_q generated across the NbN electrodes. U_q is calculated, using total capacitance C_{tot} that comes from electrode capacitance C_e and the microwave circuit capacitance C_c .

$$U_q = \frac{1}{2}(C_c + C_e)V_0^2 \quad (6.2)$$

Typically, C_{tot} is dominated by C_c thanks to the small footprint of the electrodes. This will be discussed more in the next subsection.

Figure 6.2a,b shows our piezo-acoustic cavity design that supports a second order hybrid breathing-like mode which hybridizes with the mechanical mode of the optomechanical crystal while providing overlap with the electric field induced by the NbN electrodes. piezo-box and electrode dimensions are optimized for highest piezoelectric coupling using Nelder-Mead optimization method. Resulting design with $w_x = w_y = 760nm$ with a box thickness of $t = 200nm$ gives $g_{pe}/2\pi = 7MHz$ at $w_p/2\pi = 10.27GHz$. Mode isolation for this mode is 50MHz (considering the closest high g_{pe} mode in Figure 6.2c).

Design of the optomechanical cavity with a phonon waveguide combined with the phononically shielded piezoacoustic cavity is shown in Figure 6.3 along with the coupling schematic between different parts of the microwave-optical transducer. Here the mechanical mode \hat{b} is hybridized between the optomechanical and piezoacoustic cavities. This gives rise to the simultaneous optomechanical (shown as G_{OM}) and piezoelectric (shown as g_{pe}) coupling of the same mechanical mode. Coupling rates for the hybrid modes around 10.35GHz are shown in Figure 6.3c,d. The mode of interest, that is also shown in Figure 6.3b is highlighted with red. Other than the highlighted mode, there are other modes in the spectrum that can be used for microwave-optical transduction given their high piezoelectric coupling rates, to the expense of lower optomechanical coupling on the order of $\sim 500kHz$.

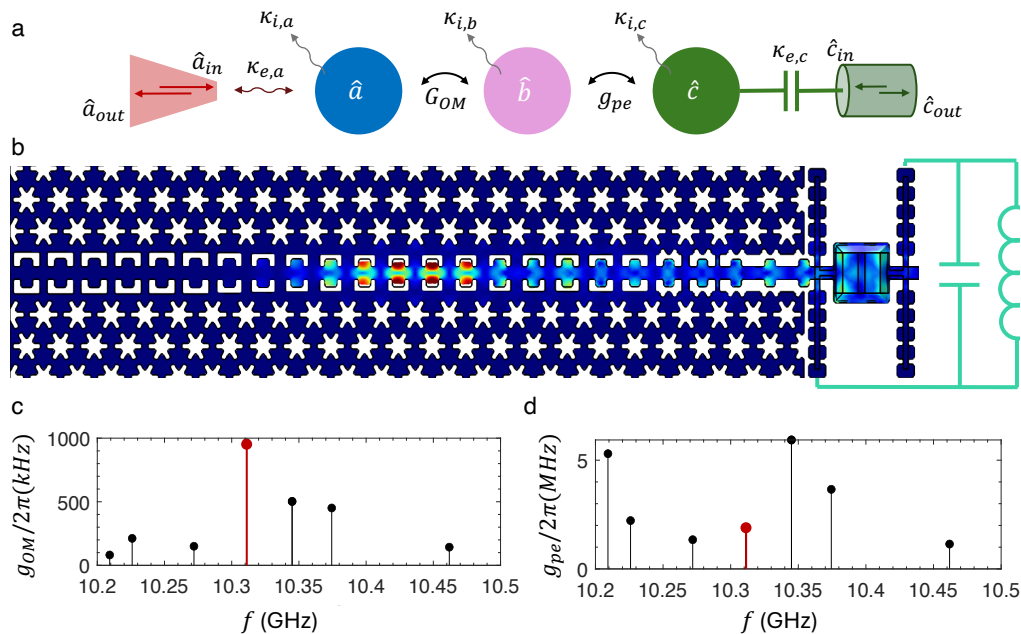


Figure 6.3: **2D optical-microwave transducer.** **a)** Piezo-optomechanical optical to microwave transduction mode schematic. **b)** Displacement field of the hybridized mechanical mode of interest. **c)** Single photon optomechanical coupling rate $g_{OM}/2\pi$ for the mechanical modes centered around 10.35 GHz. Mode of interest is colored in red. **d)** Piezoelectric coupling rate $g_{pe}/2\pi$ for the mechanical modes centered around 10.35 GHz. Mode of interest is colored in red.

Light robust NbN superconducting microwave resonator

We use superconducting kinetic inductance resonators, fabricated from niobium nitride (NbN) thin films, as the microwave resonators integrated into our microwave-optical transducer design. The NbN resonators are capacitively coupled to a 50Ω feedline via a coupler composed of interdigitated fingers, which is used to tune the extrinsic coupling of the kinetic inductance resonator to the feedline. The resonator loop is terminated on the piezo-box using NbN electrodes (see Figure 6.4).

Kinetic inductance resonators have two types of contributing inductance. Geometric inductance arises from the magnetic field generated by the resonator's physical layout, while kinetic inductance originates from the inertia of Cooper pairs due to the current flowing through the resonator. In this work, we employ a ladder-like resonator design consisting of local loops engineered to generate a current in response to an applied external magnetic field. The resulting direct current in the resonator tunes the kinetic inductance, and consequently, the resonance frequency.

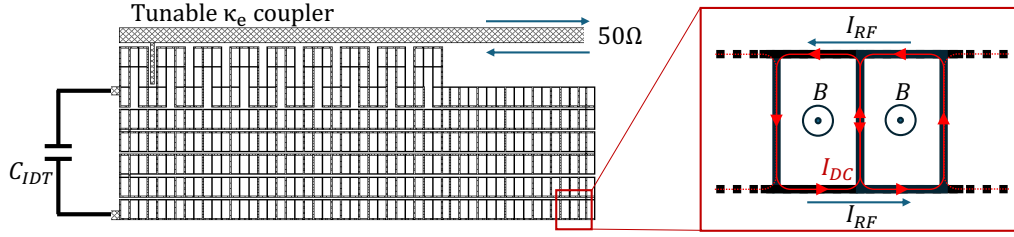


Figure 6.4: **Tunable kinetic inductance resonator.** Meandered, electromagnetically tunable kinetic inductance resonator made out of superconductive loops. Resonator is coupled to a 50Ω feedline via a tunable κ_e coupler. Coupling strength can be tuned by changing number of coupler fingers. A schematic of the tuning mechanism is given on the right panel, showing RF current I_{RF} and the externally induced tuning current I_{DC} .

The relationship between the induced current and the resonator's kinetic inductance is given by the following expression. [96]

$$L_k(I_{sc}) \approx L_k(0) \left[1 + \left(\frac{I_{DC}}{I^*} \right)^2 \right] \quad (6.3)$$

Where I_{DC} is the induced current and it is related to the applied magnetic field and the loop dimensions as follows.

$$I_{DC} \approx B_{ext} \frac{d}{\mathcal{L}_{sc}} \quad (6.4)$$

Where d is the width of the unit loop and \mathcal{L}_{sc} is the effective geometric inductance per unit length. According to the Equation 6.3, a quadratic inductance and frequency tuning relation is expected for a linearly changing tuning coil current.

When the superconducting resonator is illuminated with laser pulses, photons with energies exceeding the superconducting bandgap generate quasiparticles in the thin film. The sensitivity of the film to high-energy photons, along with the associated quasiparticle relaxation times, must be considered when selecting materials—especially since the optomechanical crystals are integrated on the same chip as the superconducting microwave resonators. The choice of NbN for the microwave resonators is motivated by its short quasiparticle relaxation time, on the order of nanoseconds, which is several orders of magnitude faster than that of aluminum (\sim ms), a commonly used superconductor in microwave resonators and Josephson junctions.

Superconducting kinetic inductance resonators used in this work made out of $25nm$ NbN typically have a sheet inductance of $23\Omega/sq$. The circuit capacitance is $7fF$, dominated by the self capacitance of the resonator with a small contribution from the terminating electrodes that is on the order of tens of aF . A detailed analysis regarding kinetic inductance resonators used in this work can be found in Ref [97, 98].

6.2 Fabrication of the hybrid 2D OMC transducer

Previously developed metalized phononic shield designs in the Painter Lab utilize a $\sim 100nm$ thick aluminum metallization layer with a $220nm$ silicon device layer, which provides a large enough band gap around $5GHz$ [27, 76, 99]. However, due to limitations in nanofabrication techniques, designing a one-dimensional phononic shield with a thick metallization layer ($> 80nm$) has remained challenging for band gaps centered above $10GHz$. This limitation led us to adopt a $25nm$ sputtered NbN thin film for both the electrodes and shield metallization layer in the 2D transducer fabrication flow. Implementing this change required modifications to certain steps in the traditional transducer fabrication process, ultimately resulting in a simpler and faster fabrication flow. These modifications will be further discussed in the coming subsection. All the technical details including the tools used in each process step are given in the Appendix A.

Fabrication process starts with an SOI wafer with $725\mu m$ handle silicon (Si), $3\mu m$ buried silicon dioxide layer (BOX) and a $220nm$ device silicon layer with resistivity $\rho \sim 3k\Omega.cm$. SOI wafer is sputtered with $300nm$ c-cut Aluminum Nitrate (AlN) and diced into $10mm$ by $10mm$ dies for further processing. After this step, dies are processed individually.

Process proceeds with thinning down the AlN thin film using inductively coupled plasma reactive ion etching (ICP-RIE) with Argone/Chlorine (Ar/Cl_2) gasses. Initial AlN thin film thickness is $300nm$ and for our design, we etch $100nm$ AlN at this step to get $200nm$ final film thickness. $85nm$ thick Chrome/Gold (Cr/Au) alignment markers are deposited in the next step, using electron beam deposition for the alignment of subsequent layers (see Figure 6.5).

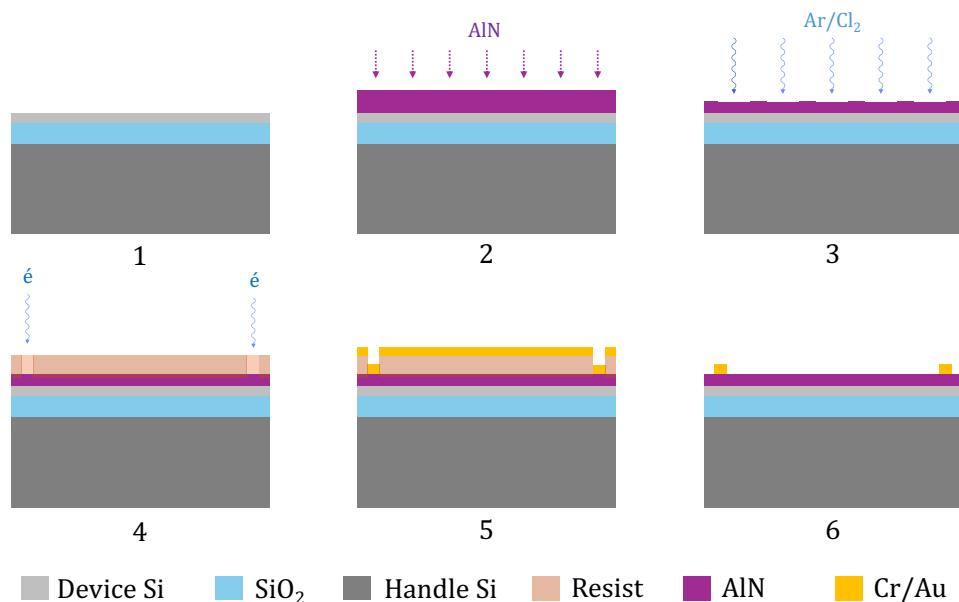


Figure 6.5: **AlN and marker deposition.** Fabrication flow of the AlN sputtering followed by Cr/Au marker deposition and liftoff.

AlN piezo-box

AlN piezo-box fabrication starts with the definition of the etch mask on a spin-coated ZEP-520A resist layer using electron beam lithography (EBL). A 100nm silicon dioxide (SiO_2) etch mask is deposited using electron beam evaporation in 3 consecutive steps with varying deposition rates to prevent pinhole formation on the mask. Using the created SiO_2 mask, the AlN thin film is partially etched in ICP-RIE with Ar/Cl_2 chemistry. It is crucial to stop the plasma etch before reaching the Si device layer, since the aggressive Ar/Cl_2 plasma damages the Si device layer surface, introducing undesired thinning and surface roughness.

After the partial dry etch, the remaining 10 – 30nm AlN is etched in 25% aqueous Tetramethylammonium Hydroxide (TMAH) solution at room temperature. Finally, the SiO_2 mask used in the etch process is removed using 1:10 Hydrofluoric acid (HF) Ammonium fluoride (NH_4F) buffered oxide etchant (BOE) (see Figure 6.6).

The traditional AlN piezo-box fabrication process used in earlier transducer works relied on dry etching for full piezo-box definition, followed by an aggressive, high-temperature Phosphoric acid etch to clean the remaining AlN on the chip. This process has two drawbacks: first, the uneven sidewall angle, which becomes very steep toward the top of the piezo-box. This steep sidewall makes it harder to achieve

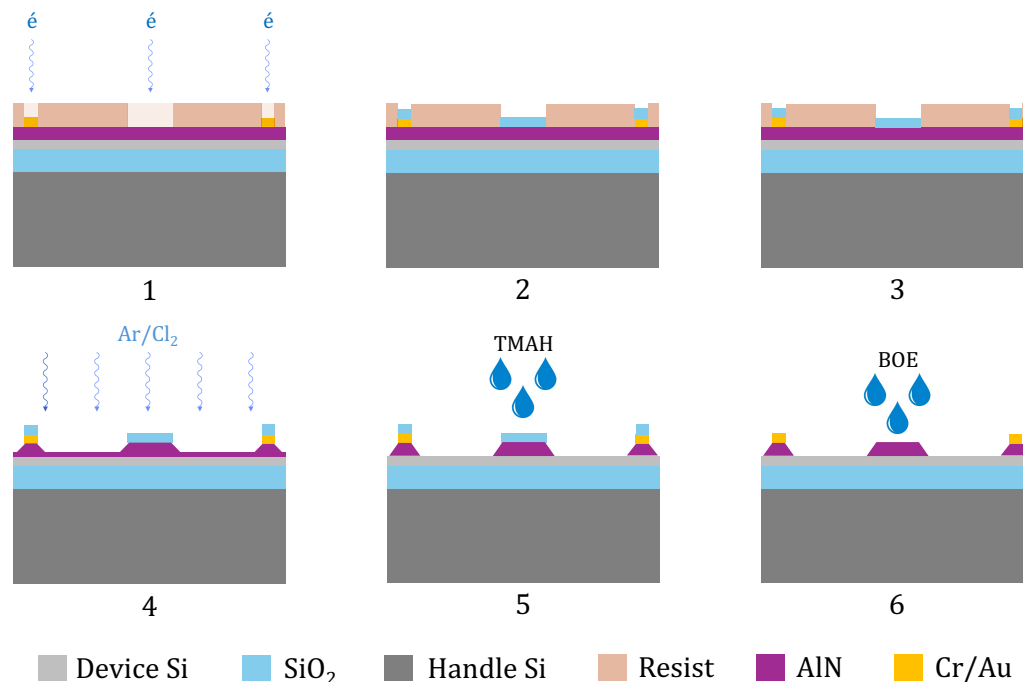


Figure 6.6: AlN piezo-box fabrication. Fabrication flow of the AlN piezo-box, from SiO₂ mask liftoff to the wet etching of AlN. Finally mask removal with buffered oxide etchant (BOE).

a galvanically continuous metallization layer from the silicon surface to the top of the piezo-box. Secondly, during the dry etch process, a thin trench is etched into the silicon device layer around the piezo-box, which also introduces a challenge for the metallization layer to climb over to reach the box from the shield area (see Figure 6.7a). To overcome these problems, angled deposition of a 100nm thick Aluminum (Al) metallization layer was used. However, as discussed earlier in this section, using such a thick metal layer on the phononic shield is not an option for the 2D OMC transducer due to the difficulty in achieving large enough bandgaps around 10.3GHz.

The new AlN piezo-box fabrication technique presented in this section can create smooth, $\sim 57^\circ$ angled sidewalls thanks to the TMAH wet etch step that selectively etches the AlN along the 57° crystal boundary [100]. Moreover, the partial dry etch leaves the silicon untouched, resulting in a clean Si device layer around the piezo-box as shown in Figure 6.7b,c. These two advances are imperative for the use of 25nm NbN metallization layer for electrode fabrication.

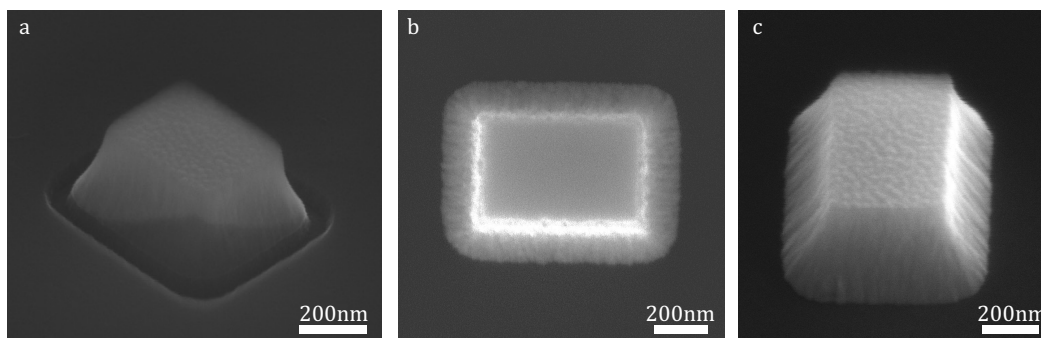


Figure 6.7: **SEM of the AlN piezo-box.** **a)** An AlN piezo-box fabricated with the 'traditional' methods. Trench around the piezo-box and the steep sidewall angle is visible. **b)** An AlN piezo-box fabricated with the new 2-step dry/wet etching presented here. Surrounding silicon surface kept undamaged. **c)** Angled view of the AlN piezo-box fabricated with the new 2-step dry/wet etching. Sidewall angle appears to be more uniform compared to the piezo-box on the panel **a**.

NbN resonators and electrodes

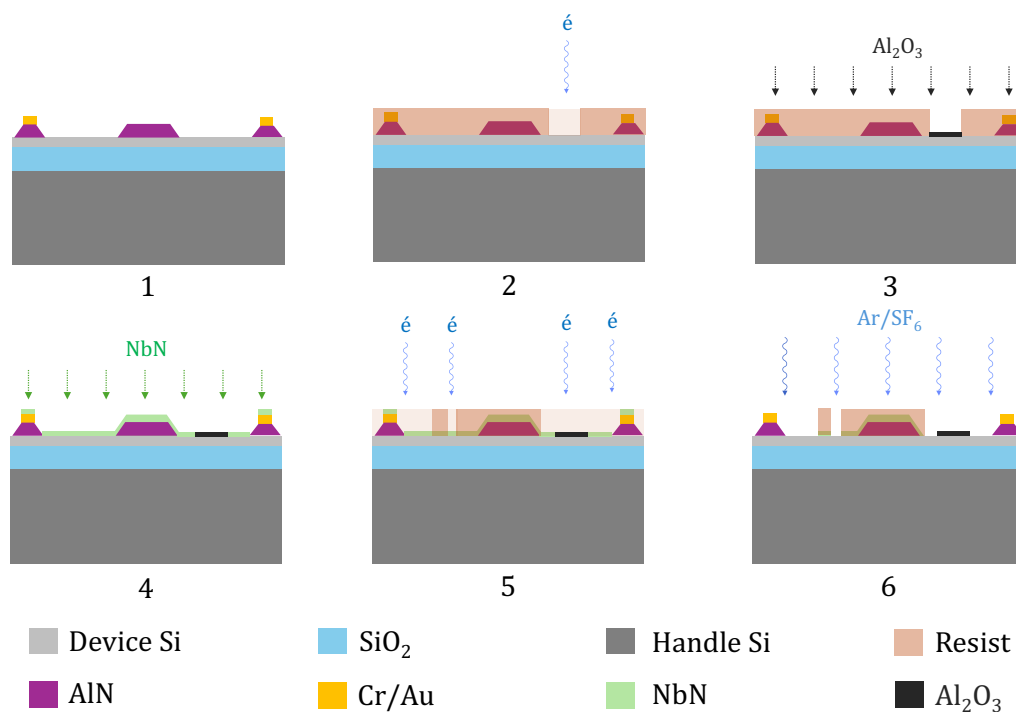


Figure 6.8: **NbN layer fabrication.** Fabrication flow of NbN layer starting from the protection layer deposition followed by the ICP-RIE etch of the NbN thin film.

Similarly to Ar/Cl_2 plasma, SF_6/Ar chemistry used for the NbN layer etching attacks the Si device layer, therefore a protection layer that covers the surfaces where the optomechanical crystal is patterned must be deposited. This protection is provided with a 100nm Aluminum oxide (Al_2O_3) layer deposited with electron beam deposition prior to the NbN sputtering process. Following the protection layer deposition, the sample is sputtered with a 25nm NbN thin film (see Figure 6.8). Critical temperature T_c of the sputtered NbN thin film is measured to be $\sim 9K$ while the sheet inductance is $23pH/sq$.

NbN resonators and the electrodes are patterned on $\sim 240nm$ thick ZEP 520A and etched using ICP-RIE with SF_6/Ar chemistry.

2D OMC with phonon waveguide

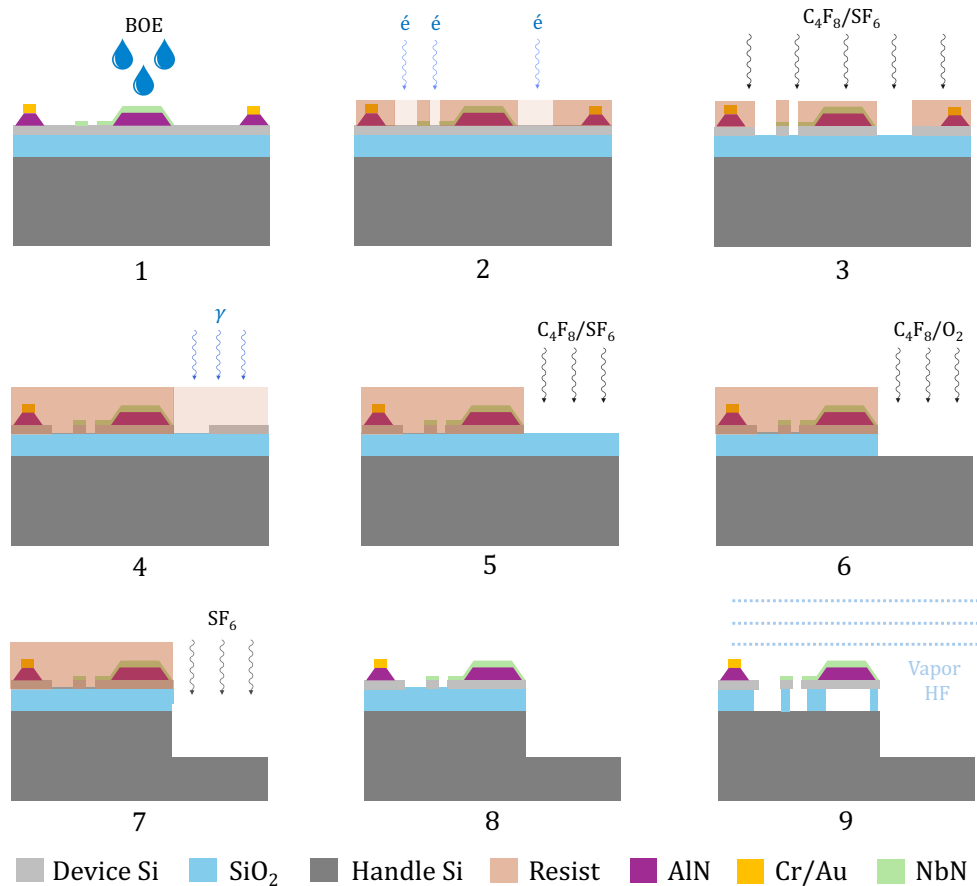


Figure 6.9: **Silicon layer fabrication.** Fabrication flow of silicon OMC including the deep silicon etch step that creates the *cliff* at the edge of the sample for end fire coupling.

The final stage of the 2D OMC transducer fabrication starts with the removal of the protection layer in 1:10 BOE, followed by the patterning of the OMC structures on $\sim 240\text{nm}$ thick ZEP 520A. The silicon device layer is then etched using ICP-RIE with Pseudo Bosch etch (C_4F_8/SF_6).

In the next step, a $\sim 120\mu\text{m}$ deep cliff-like opening is created by deep etching to facilitate the endfire coupling to the OMCs. To create the cliff, Si device layer, BOX layer and $\sim 120\mu\text{m}$ handle Si are etched with deep reactive ion etching (DRIE) using C_4F_8/SF_6 , C_4F_8/O_2 and SF_6 chemistry, respectively. SPR 220-7 photoresist is used for masking the aggressive deep etch.

Finally, transducers and the NbN resonators are suspended using anhydrous hydrofluoric acid vapor etching by removing the BOX layer (see Figure 6.9).

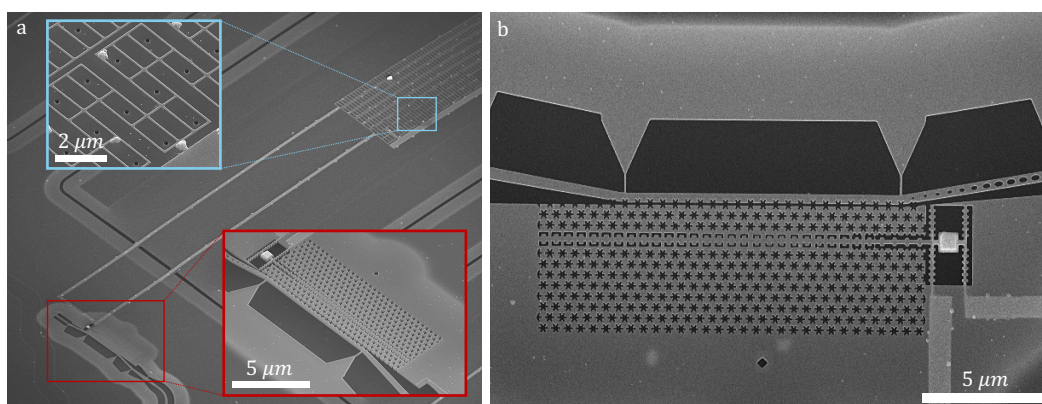


Figure 6.10: **SEM image of the 2D transducer.** **a)** Hybrid side coupled 2D OMC based optical to microwave transducer and light robust superconductive NbN microwave resonators. Blue inset shows the unit cell loops of the NbN resonators. Red inset shows the hybrid 2D OMC with the piezoacoustic cavity. **b)** A close up SEM of the 2D OMC transducer.

Figure 6.10 shows the Scanning Electron Microscope images of a fabricated microwave-optical transducer. Insets in Figure 6.10 show the unit cell loops of the superconductive resonator (blue) and hybrid side-coupled 2D optomechanical crystal cavity (red).

6.3 Measurement setup

The cryogenic measurement setup used in our characterization experiments is largely similar to the setup presented in Chapter 5, with several additions to accommodate the microwave resonators (see Figure 6.11). The first major modification is the

integration of four microwave lines on the device package, which are addressable via a cryogenic microwave switch. The reflected signal passes through a microwave circulator and a high-electron-mobility transistor (HEMT) amplifier before exiting the dilution refrigerator. The second key addition is a superconductive tuning coil made out of NbTi, driven by an external current source, placed directly above the sample to tune the superconducting kinetic inductance resonators. The coil is designed to create a magnetic field of $\sim 0.6mT$ for an applied current of 400mA.

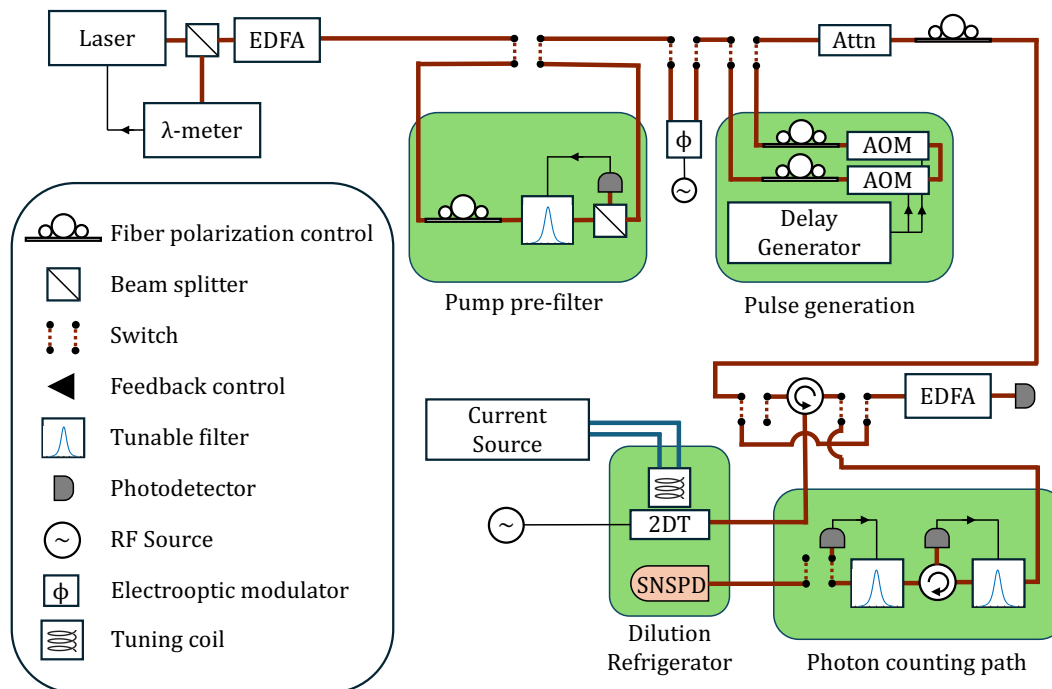


Figure 6.11: **Experimental setup.** A tuning coil placed above the sample is used to create a magnetic field to tune NbN resonators. A signal generator is used to drive NbN resonators. Rest of the setup is identical to Figure 5.3.

6.4 Room temperature characterization

Room temperature measurements of the microwave-optical transducer consists of characterization of the optical and mechanical spectrum as well as the direct microwave-optical transduction using a coherent microwave drive in the absence of the NbN resonators.

Measured devices have optical wavelengths of 1550nm and quality factors on the order of 200×10^3 . Mechanical spectrum have three major mechanical modes with high optomechanical coupling around 10.35GHz as design suggests.

The sample under investigation is specifically designed for room-temperature testing, utilizing a continuous microwave drive instead of a microwave resonator. The transducer features NbN electrodes patterned on the piezo-box region; however, these electrodes are not connected to a kinetic inductance resonator but are instead terminated with a microwave launcher designed for operation with a microwave probe. During testing, a microwave drive is applied through the NbN launchers using a microwave probe, while the transducer is simultaneously probed optically. After characterizing the optical and mechanical spectra, a single microwave tone at the mechanical resonance frequency is applied, and the mechanical mode of the optomechanical crystal is probed with a blue-detuned ($\Delta = -\omega_m$) optical pulse. The resulting mechanical spectrum includes a broad thermal peak and a sharp peak at the microwave drive frequency (see Figure 6.12), providing a clear signature of microwave-optical transduction.

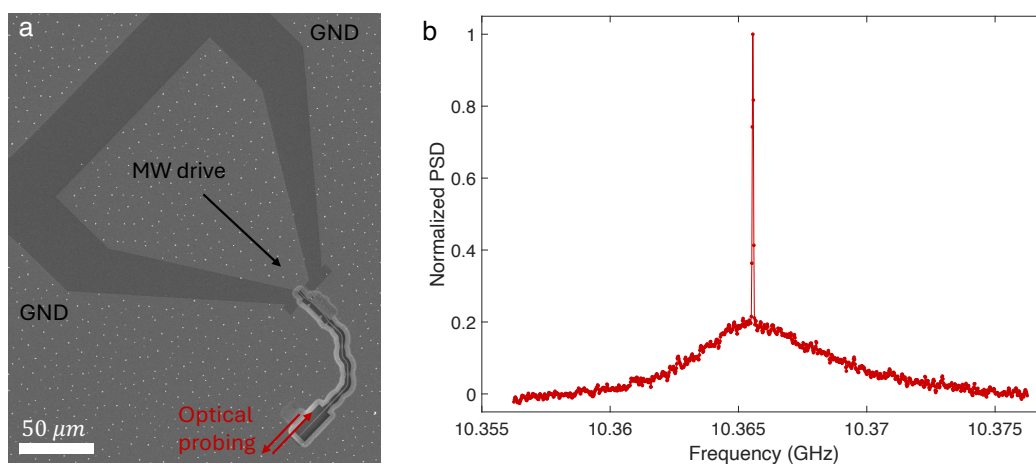


Figure 6.12: **Mechanical mode spectrum with a coherent microwave drive at 300K.** **a)** SEM image of the device under test. Microwave drive is applied to the piezoacoustic section of the device through the NbN launcher. OMC is probed using a dimpled fiber. **b)** Mechanical mode spectrum showing thermal background and the sharp coherent tone applied through the microwave probe.

The microwave-to-mechanical conversion efficiency is estimated to be $\eta_{\mu \rightarrow m} \sim 10^{-10}$, primarily limited by the impedance mismatch between the 50 Ω microwave probe and the NbN metallization layer—caused by the film’s high room-temperature resistivity—that drastically reduces the achievable conversion efficiency.

6.5 Preliminary cryogenic characterizations

Cryogenic characterization of the microwave-optical transducer is performed in a dilution refrigerator equipped with integrated optical and microwave probing capabilities. The transducer chip, comprising 16 individual transducers fed by four microwave ports, is mounted on a thermally conductive stage. A NbTi superconductive electromagnet is placed over the sample to facilitate the in situ tuning of NbN microwave resonators. A three-axis Attocube nanopositioner is used to precisely align a lensed optical fiber with the end-fire couplers attached to the transducers for optical probing. The sample is cooled down to a base temperature of 10mK.

This test consists of three major steps. The first step involves optical and mechanical characterization of the hybrid optomechanical cavity. The second step focuses on evaluating the performance and tunability of the NbN resonators, which can only be tested at 10mK—well below the critical temperature of the NbN thin film ($T_c \approx 9, \text{K}$). Finally, resonant microwave-optical transduction is demonstrated by tuning the microwave resonators into resonance with the mechanical mode of the transducer and probing the input microwave signal via the optical reflection spectrum.

Figure 6.13a shows the mechanical spectra of a hybrid optomechanical crystal. Optical mode wavelength is at 1561.9nm, close to designed value. Mechanical spectrum has three peaks centered around 10.3GHz with high optomechanical coupling rates which closely match the designed mechanical spectrum for the piezobox size of 770nm by 770nm, shown in Figure 6.13b.

Microwave resonator is tuned using coil currents up to 250mA which results in a quadratic tuning of the resonance by more than 700MHz at the highest tuning point. Higher tuning currents lead to flux trapping in the resonator due to excessive DC loading hence this can be considered as the maximum achievable tuning range. For the presented transducer, the microwave resonator can be tuned into the mechanical frequency using reasonable tuning currents.

In the final test we tune the NbN kinetic inductance resonator into mechanical frequency using the NbTi tuning coil to minimize the detuning. Then, similarly to the room temperature transduction characterization, we drive our microwave resonators with a microwave tone at the mechanical mode frequency. Microwave photons are converted into microwave frequency phonons at the piezo-acoustic cavity. This conversion populates the mechanical mode hybridized between the piezo-acoustic and the optomechanical cavities. At the same time, a blue-detuned ($\Delta = -\omega_m$)

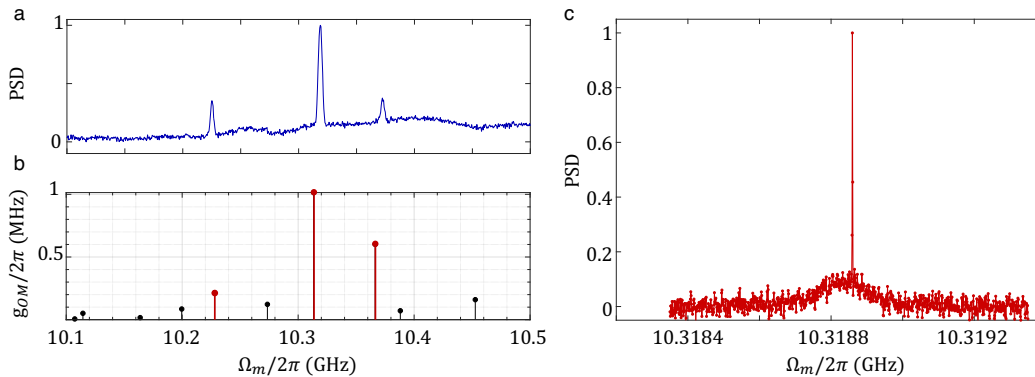


Figure 6.13: **Transduction under cryogenic conditions.** **a)** Mechanical spectrum of the transducer under test. Three peaks correspond to three modes with high g_{OM} . **b)** Simulated mechanical spectrum of the fabricated design for a box size of 770nm by 770nm. Modes highlighted in red, high g_{OM} modes are aligning with the peaks observed in the measured spectrum. **c)** Mechanical spectrum of the middle peak shown in panel **a** with applied microwave drive. The sharp peak on top of the thermal spectrum of the mechanical mode can be attributed to the microwave drive.

continuous laser pump is used to probe the mechanical mode population at the optomechanical cavity. Reflected optical signal is measured using a nanosecond detector and a spectrum analyzer. Results are shown in the Figure 6.13c. Similarly to the room temperature tests, we observe a single, sharp peak at the input microwave signal frequency along with the thermal spectrum of the mechanical mode. Resulting microwave-optical transduction suggests piezo electric coupling of $g_{PE} \approx 400Hz$ which is 3 orders of magnitude smaller than the designed value. This could be related to a number of factors including breaks in the thin NbN connections over the phononic shield and disconnected NbN layer on the piezo-box.

6.6 Outlook

We presented the design and fabrication of a two-dimensional piezo-optomechanical crystal-based microwave-optical transducer. While the preliminary results are promising, further improvements in both device design and fabrication processes are required to achieve and surpass state-of-the-art transduction metrics. A key limitation of the current design is the susceptibility of the targeted mode to fabrication-induced disorder. High piezoelectric coupling rates are achieved only within a narrow parameter window, making the device's performance highly sensitive to dimensional variations.

Another critical improvement involves optimizing the NbN electrodes on the AlN piezo-box to ensure reliable connectivity, while maintaining the NbN metallization layer as thin as possible. Additionally, employing alternative material platforms, particularly for the piezoelectric element in the piezoacoustic cavity, offers significant potential to enhance transduction performance. Among the most promising candidates are lithium niobate (LiNbO_3), barium titanate (BaTiO_3), and strontium titanate (SrTiO_3), owing to their strong piezoelectric properties. However, integrating these materials into device fabrication presents new challenges that must be carefully addressed.

With these design and fabrication improvements, the side-coupled 2D OMC-based microwave-optical transducer presented here could serve as a promising platform for high-efficiency, low-noise microwave-optical transduction. We believe that next generation microwave-optical transducers will implement a similar design technique to overcome fundamental limitations of the one dimensional structures.

Bibliography

- [1] A. H. Safavi-Naeini, T. P. M. Alegre, J. Chan, M. Eichenfield, M. Winger, Q. Lin, J. T. Hill, D. Chang, and O. Painter, “Electromagnetically induced transparency and slow light with optomechanics,” *Nature*, vol. 472, pp. 69–73, 2011.
- [2] A. H. Safavi-Naeini and O. Painter, “Design of optomechanical cavities and waveguides on a simultaneous bandgap phononic-photon crystal slab,” *Optics express*, vol. 18, no. 14, pp. 14926–14943, 2010.
- [3] A. H. Safavi-Naeini, T. M. Alegre, J. Chan, M. Eichenfield, M. Winger, Q. Lin, J. T. Hill, D. E. Chang, and O. Painter, “Electromagnetically induced transparency and slow light with optomechanics,” *Nature*, vol. 472, no. 7341, pp. 69–73, 2011.
- [4] A. H. Safavi-Naeini and O. Painter, “Optomechanical crystal devices,” in *Cavity Optomechanics* (M. Aspelmeyer, T. J. Kippenberg, and F. Marquardt, eds.), Quantum Science and Technology, pp. 195–231, Springer Berlin Heidelberg, 2014.
- [5] A. H. Safavi-Naeini, J. Chan, J. T. Hill, S. Gröblacher, H. Miao, Y. Chen, M. Aspelmeyer, and O. Painter, “Laser noise in cavity-optomechanical cooling and thermometry,” *New J. Phys.*, vol. 15, p. 035007, 2013.
- [6] M. Eichenfield, J. Chan, R. M. Camacho, K. J. Vahala, and O. Painter, “Optomechanical crystals,” *nature*, vol. 462, no. 7269, pp. 78–82, 2009.
- [7] M. Aspelmeyer, T. J. Kippenberg, and F. Marquardt, “Cavity optomechanics,” *Rev. Mod. Phys.*, vol. 86, pp. 1391–1452, Dec 2014.
- [8] F. Marquardt and S. M. Girvin, “Optomechanics (a brief review),” *arXiv preprint arXiv:0905.0566*, 2009.
- [9] A. Abramovici, W. E. Althouse, R. W. Drever, Y. Gürsel, S. Kawamura, F. J. Raab, D. Shoemaker, L. Sievers, R. E. Spero, K. S. Thorne, *et al.*, “Ligo: The laser interferometer gravitational-wave observatory,” *science*, vol. 256, no. 5055, pp. 325–333, 1992.
- [10] T. P. Purdy, D. W. C. Brooks, T. Botter, N. Brahms, Z.-Y. Ma, and D. M. Stamper-Kurn, “Tunable cavity optomechanics with ultracold atoms,” *Phys. Rev. Lett.*, vol. 105, p. 133602, Sep 2010.
- [11] O. Arcizet, P.-F. Cohadon, T. Briant, M. Pinard, A. Heidmann, J.-M. Mackowski, C. Michel, L. Pinard, O. Français, and L. Rousseau, “High-sensitivity optical monitoring of a micro-mechanical resonator with a quantum-limited optomechanical sensor,” *Phys. Rev. Lett.*, vol. 97, p. 133601, 2006.

- [12] S. Gigan, H. R. Böhm, M. Paternostro, F. Blaser, G. Langer, J. B. Hertzberg, K. C. Schwab, D. Bäuerle, M. Aspelmeyer, and A. Zeilinger, “Self-cooling of a micromirror by radiation pressure,” *Nature*, vol. 444, pp. 67–70, 2006.
- [13] J. D. Thompson, B. M. Zwickl, A. M. Jayich, F. Marquardt, S. M. Girvin, and J. G. E. Harris, “Strong dispersive coupling of a high-finesse cavity to a micromechanical membrane,” *Nature*, vol. 452, pp. 72–75, 2008.
- [14] I. Favero and K. Karrai, “Optomechanics of deformable optical cavities,” *Nature Photon.*, vol. 3, pp. 201–205, 2009.
- [15] D. Armani, T. Kippenberg, S. Spillane, and K. Vahala, “Ultra-high-q toroid microcavity on a chip,” *Nature*, vol. 421, no. 6926, pp. 925–928, 2003.
- [16] C. W. Gardiner and M. J. Collett, “Input and output in damped quantum systems: Quantum stochastic differential equations and the master equation,” *Physical Review A*, vol. 31, no. 6, p. 3761, 1985.
- [17] J. T. Hill, A. H. Safavi-Naeini, J. Chan, and O. Painter, “Coherent optical wavelength conversion via cavity optomechanics,” *Nature Commun.*, vol. 3, p. 1196, 2012.
- [18] H. J. Kimble, “The quantum internet,” *Nature*, vol. 453, pp. 1023–1030, June 2008.
- [19] N. J. Lambert, A. Rueda, F. Sedlmeir, and H. G. Schwefel, “Coherent conversion between microwave and optical photons—an overview of physical implementations,” *Advanced Quantum Technologies*, vol. 3, no. 1, p. 1900077, 2020.
- [20] G. S. MacCabe, H. Ren, J. Luo, J. D. Cohen, H. Zhou, A. Sipahigil, M. Mirhosseini, and O. Painter, “Nano-acoustic resonator with ultralong phonon lifetime,” *Science*, vol. 370, no. 6518, pp. 840–843, 2020.
- [21] A. H. Safavi-Naeini, *Quantum optomechanics with silicon nanostructures*. California Institute of Technology, 2013.
- [22] M. H. Devoret and R. J. Schoelkopf, “Superconducting circuits for quantum information: an outlook,” *Science*, vol. 339, no. 6124, pp. 1169–1174, 2013.
- [23] M. Mirrahimi, Z. Leghtas, V. V. Albert, S. Touzard, R. J. Schoelkopf, L. Jiang, and M. H. Devoret, “Dynamically protected cat-qubits: a new paradigm for universal quantum computation,” *New Journal of Physics*, vol. 16, no. 4, p. 045014, 2014.
- [24] N. Ofek, A. Petrenko, R. Heeres, P. Reinhold, Z. Leghtas, B. Vlastakis, Y. Liu, L. Frunzio, S. M. Girvin, L. Jiang, *et al.*, “Extending the lifetime of a quantum bit with error correction in superconducting circuits,” *Nature*, vol. 536, no. 7617, pp. 441–445, 2016.

- [25] F. Arute, K. Arya, R. Babbush, D. Bacon, J. C. Bardin, R. Barends, R. Biswas, S. Boixo, F. G. Brandao, D. A. Buell, *et al.*, “Quantum supremacy using a programmable superconducting processor,” *Nature*, vol. 574, no. 7779, pp. 505–510, 2019.
- [26] S. Storz, J. Schär, A. Kulikov, P. Magnard, P. Kurpiers, J. Lütolf, T. Walter, A. Copetudo, K. Reuer, A. Akin, *et al.*, “Loophole-free bell inequality violation with superconducting circuits,” *Nature*, vol. 617, no. 7960, pp. 265–270, 2023.
- [27] S. Meesala, S. Wood, D. Lake, P. Chiappina, C. Zhong, A. D. Beyer, M. D. Shaw, L. Jiang, and O. Painter, “Non-classical microwave–optical photon pair generation with a chip-scale transducer,” *Nature Physics*, pp. 1–7, 2024.
- [28] L. M. Duan, M. D. Lukin, J. I. Cirac, and P. Zoller, “Long-distance quantum communication with atomic ensembles and linear optics,” *Nature*, vol. 414, pp. 413–318, 2001.
- [29] S. Mosor, J. Hendrickson, B. Richards, J. Sweet, G. Khitrova, H. Gibbs, T. Yoshie, A. Scherer, O. Shchekin, and D. Deppe, “Scanning a photonic crystal slab nanocavity by condensation of xenon,” *Applied Physics Letters*, vol. 87, no. 14, 2005.
- [30] S. Strauf, M. T. Rakher, I. Carmeli, K. Hennessy, C. Meier, A. Badolato, M. J. DeDood, P. M. Petroff, E. L. Hu, E. Gwinn, *et al.*, “Frequency control of photonic crystal membrane resonators by monolayer deposition,” *Applied Physics Letters*, vol. 88, no. 4, p. 043116, 2006.
- [31] D. Turčinková, M. Ines Amanti, F. Castellano, M. Beck, and J. Faist, “Continuous tuning of terahertz distributed feedback quantum cascade laser by gas condensation and dielectric deposition,” *Applied Physics Letters*, vol. 102, no. 18, 2013.
- [32] C. W. Wong, P. T. Rakich, S. G. Johnson, M. Qi, H. I. Smith, E. P. Ippen, L. C. Kimerling, Y. Jeon, G. Barbastathis, and S.-G. Kim, “Strain-tunable silicon photonic band gap microcavities in optical waveguides,” *Applied physics letters*, vol. 84, no. 8, pp. 1242–1244, 2004.
- [33] I. Luxmoore, E. D. Ahmadi, B. Luxmoore, N. Wasley, A. Tartakovskii, M. Hugues, M. Skolnick, and A. Fox, “Restoring mode degeneracy in h1 photonic crystal cavities by uniaxial strain tuning,” *Applied Physics Letters*, vol. 100, no. 12, p. 121116, 2012.
- [34] J. Martín-Sánchez, R. Trotta, A. Mariscal, R. Serna, G. Piredda, S. Stroj, J. Edlinger, C. Schimpf, J. Aberl, T. Lettner, *et al.*, “Strain-tuning of the optical properties of semiconductor nanomaterials by integration onto piezoelectric actuators,” *Semiconductor Science and Technology*, vol. 33, no. 1, p. 013001, 2018.

- [35] A. Faraon, D. Englund, I. Fushman, J. Vučković, N. Stoltz, and P. Petroff, “Local quantum dot tuning on photonic crystal chips,” *Applied Physics Letters*, vol. 90, no. 21, p. 213110, 2007.
- [36] D. Armani, B. Min, A. Martin, and K. J. Vahala, “Electrical thermo-optic tuning of ultrahigh-q microtoroid resonators,” *Applied physics letters*, vol. 85, no. 22, pp. 5439–5441, 2004.
- [37] M. W. Pruessner, T. H. Stievater, M. S. Ferraro, and W. S. Rabinovich, “Thermo-optic tuning and switching in soi waveguide fabry-perot microcavities,” *Optics Express*, vol. 15, no. 12, pp. 7557–7563, 2007.
- [38] C. L. Panuski, I. Christen, M. Minkov, C. J. Brabec, S. Trajtenberg-Mills, A. D. Griffiths, J. J. McKendry, G. L. Leake, D. J. Coleman, C. Tran, *et al.*, “A full degree-of-freedom spatiotemporal light modulator,” *Nature Photonics*, vol. 16, no. 12, pp. 834–842, 2022.
- [39] H. Lee, S. Kiravittaya, S. Kumar, J. Plumhof, L. Balet, L. H. Li, M. Francardi, A. Gerardino, A. Fiore, A. Rastelli, *et al.*, “Local tuning of photonic crystal nanocavity modes by laser-assisted oxidation,” *Applied Physics Letters*, vol. 95, no. 19, 2009.
- [40] R. Luo, Y. He, H. Liang, M. Li, and Q. Lin, “Highly tunable efficient second-harmonic generation in a lithium niobate nanophotonic waveguide,” *Optica*, vol. 5, no. 8, pp. 1006–1011, 2018.
- [41] K. Hennessy, C. Högerle, E. Hu, A. Badolato, and A. Imamoglu, “Tuning photonic nanocavities by atomic force microscope nano-oxidation,” *Applied physics letters*, vol. 89, no. 4, p. 041118, 2006.
- [42] A. Yokoo, T. Tanabe, E. Kuramochi, and M. Notomi, “Ultrahigh-q nanocavities written with a nanoprobe,” *Nano letters*, vol. 11, no. 9, pp. 3634–3642, 2011.
- [43] Raith Nanofabrication, *EBPG plus dedicated electron beam lithography*, 6 2021. Rev. 3.
- [44] G. Binnig, C. F. Quate, and C. Gerber, “Atomic force microscope,” *Physical review letters*, vol. 56, no. 9, p. 930, 1986.
- [45] F. J. Giessibl, “Advances in atomic force microscopy,” *Reviews of modern physics*, vol. 75, no. 3, p. 949, 2003.
- [46] H.-J. Butt, E. Wolff, S. Gould, B. D. Northern, C. Peterson, and P. Hansma, “Imaging cells with the atomic force microscope,” *Journal of structural biology*, vol. 105, no. 1-3, pp. 54–61, 1990.
- [47] D. Fotiadis, S. Scheuring, S. A. Müller, A. Engel, and D. J. Müller, “Imaging and manipulation of biological structures with the afm,” *Micron*, vol. 33, no. 4, pp. 385–397, 2002.

- [48] A. Vinckier and G. Semenza, “Measuring elasticity of biological materials by atomic force microscopy,” *FEBS letters*, vol. 430, no. 1-2, pp. 12–16, 1998.
- [49] A. M. Baró and R. G. Reifenberger, *Atomic force microscopy in liquid: biological applications*. John Wiley & Sons, 2012.
- [50] S. Rützel, S. I. Lee, and A. Raman, “Nonlinear dynamics of atomic–force–microscope probes driven in lennard–jones potentials,” *Proceedings of the Royal Society of London. Series A: Mathematical, Physical and Engineering Sciences*, vol. 459, no. 2036, pp. 1925–1948, 2003.
- [51] M. Lanza, *Conductive atomic force microscopy: applications in nanomaterials*. John Wiley & Sons, 2017.
- [52] S. Lim, H. Park, G. Yamamoto, C. Lee, and J. W. Suk, “Measurements of the electrical conductivity of monolayer graphene flakes using conductive atomic force microscopy,” *Nanomaterials*, vol. 11, no. 10, p. 2575, 2021.
- [53] W. Frammelsberger, G. Benstetter, J. Kiely, and R. Stamp, “C-afm-based thickness determination of thin and ultra-thin sio₂ films by use of different conductive-coated probe tips,” *Applied Surface Science*, vol. 253, no. 7, pp. 3615–3626, 2007.
- [54] J. Christman, H. Maiwa, S.-H. Kim, A. Kingon, and R. Nemanich, “Piezoelectric measurements with atomic force microscopy,” *MRS Online Proceedings Library (OPL)*, vol. 541, p. 617, 1998.
- [55] D. Stiévenard and B. Legrand, “Silicon surface nano-oxidation using scanning probe microscopy,” *Progress in surface science*, vol. 81, no. 2-3, pp. 112–140, 2006.
- [56] H. Day and D. Allee, “Selective area oxidation of silicon with a scanning force microscope,” *Applied physics letters*, vol. 62, no. 21, pp. 2691–2693, 1993.
- [57] R. Garcia, R. V. Martinez, and J. Martinez, “Nano-chemistry and scanning probe nanolithographies,” *Chemical Society Reviews*, vol. 35, no. 1, pp. 29–38, 2006.
- [58] M. Tello and R. Garcia, “Nano-oxidation of silicon surfaces: Comparison of noncontact and contact atomic-force microscopy methods,” *Applied Physics Letters*, vol. 79, no. 3, pp. 424–426, 2001.
- [59] M. Calleja and R. Garcia, “Nano-oxidation of silicon surfaces by noncontact atomic-force microscopy: size dependence on voltage and pulse duration,” *Applied Physics Letters*, vol. 76, no. 23, pp. 3427–3429, 2000.
- [60] P. E. Barclay, K. Srinivasan, M. Borselli, and O. Painter, “Experimental demonstration of evanescent coupling from optical fibre tapers to photonic crystal waveguides,” *Electronics Letters*, vol. 39, no. 11, pp. 842–844, 2003.

- [61] P. E. Barclay, K. Srinivasan, M. Borselli, and O. Painter, “Efficient input and output fiber coupling to a photonic crystal waveguide,” *Optics letters*, vol. 29, no. 7, pp. 697–699, 2004.
- [62] F.-S. Chien, Y. Chou, T. Chen, W.-F. Hsieh, T.-S. Chao, and S. Gwo, “Nano-oxidation of silicon nitride films with an atomic force microscope: Chemical mapping, kinetics, and applications,” *Journal of Applied Physics*, vol. 89, no. 4, pp. 2465–2472, 2001.
- [63] R. Delaney, M. Urmey, S. Mittal, B. Brubaker, J. Kindem, P. Burns, C. Regal, and K. Lehnert, “Superconducting-qubit readout via low-backaction electro-optic transduction,” *Nature*, vol. 606, no. 7914, pp. 489–493, 2022.
- [64] S. M. Meenehan, *Cavity optomechanics at Millikelvin temperatures*. California Institute of Technology, 2015.
- [65] T. Middelman, A. Walkov, G. Bartl, and R. Schödel, “Thermal expansion coefficient of single-crystal silicon from 7 k to 293 k,” *Physical Review B*, vol. 92, no. 17, p. 174113, 2015.
- [66] J. Komma, C. Schwarz, G. Hofmann, D. Heinert, and R. Nawrodt, “Thermo-optic coefficient of silicon at 1550 nm and cryogenic temperatures,” *Appl. Phys. Lett.*, vol. 101, p. 041905, 2012.
- [67] S. Molesky, Z. Lin, A. Y. Piggott, W. Jin, J. Vucković, and A. W. Rodriguez, “Inverse design in nanophotonics,” *Nature Photonics*, vol. 12, no. 11, pp. 659–670, 2018.
- [68] S. So, T. Badloe, J. Noh, J. Bravo-Abad, and J. Rho, “Deep learning enabled inverse design in nanophotonics,” *Nanophotonics*, vol. 9, no. 5, pp. 1041–1057, 2020.
- [69] D. Zhu, L. Shao, M. Yu, R. Cheng, B. Desiatov, C. Xin, Y. Hu, J. Holzgrafe, S. Ghosh, A. Shams-Ansari, *et al.*, “Integrated photonics on thin-film lithium niobate,” *Advances in Optics and Photonics*, vol. 13, no. 2, pp. 242–352, 2021.
- [70] M. Yuksel, M. Maksymowych, O. Hitchcock, F. Mayor, N. Lee, M. Dykman, A. Safavi-Naeini, and M. Roukes, “Intrinsic phononic dressed states in a nanomechanical system,” *arXiv preprint arXiv:2502.18587*, 2025.
- [71] C. Wang, M. Zhang, X. Chen, M. Bertrand, A. Shams-Ansari, S. Chandrasekhar, P. Winzer, and M. Lončar, “Integrated lithium niobate electro-optic modulators operating at cmos-compatible voltages,” *Nature*, vol. 562, no. 7725, pp. 101–104, 2018.
- [72] W. Jiang, R. N. Patel, F. M. Mayor, T. P. McKenna, P. Arrangoiz-Arriola, C. J. Sarabalis, J. D. Witmer, R. Van Laer, and A. H. Safavi-Naeini, “Lithium

- niobate piezo-optomechanical crystals,” *Optica*, vol. 6, no. 7, pp. 845–853, 2019.
- [73] G. Chen, N. Li, J. D. Ng, H.-L. Lin, Y. Zhou, Y. H. Fu, L. Y. T. Lee, Y. Yu, A.-Q. Liu, and A. J. Danner, “Advances in lithium niobate photonics: development status and perspectives,” *Advanced Photonics*, vol. 4, no. 3, pp. 034003–034003, 2022.
- [74] J. Chan, A. H. Safavi-Naeini, J. T. Hill, S. Meenehan, and O. Painter, “Optimized optomechanical crystal cavity with acoustic radiation shield,” *Applied Physics Letters*, vol. 101, no. 8, 2012.
- [75] A. Wallucks, I. Marinković, B. Hensen, R. Stockill, and S. Gröblacher, “A quantum memory at telecom wavelengths,” *Nature Physics*, vol. 16, no. 7, pp. 772–777, 2020.
- [76] M. Mirhosseini, A. Sipahigil, M. Kalaei, and O. Painter, “Superconducting qubit to optical photon transduction,” *Nature*, vol. 588, no. 7839, pp. 599–603, 2020.
- [77] W. Jiang, F. M. Mayor, S. Malik, R. Van Laer, T. P. McKenna, R. N. Patel, J. D. Witmer, and A. H. Safavi-Naeini, “Optically heralded microwave photon addition,” *Nature Physics*, vol. 19, no. 10, pp. 1423–1428, 2023.
- [78] M. J. Weaver, P. Duivesteyn, A. C. Bernasconi, S. Scharmer, M. Lemang, T. C. v. Thiel, F. Hijazi, B. Hensen, S. Gröblacher, and R. Stockill, “An integrated microwave-to-optics interface for scalable quantum computing,” *Nature Nanotechnology*, pp. 1–7, 2023.
- [79] S. M. Meenehan, J. D. Cohen, G. S. MacCabe, F. Marsili, M. D. Shaw, and O. Painter, “Pulsed excitation dynamics of an optomechanical crystal resonator near its quantum ground state of motion,” *Physical Review X*, vol. 5, no. 4, p. 041002, 2015.
- [80] A. H. Safavi-Naeini, J. T. Hill, S. Meenehan, J. Chan, S. Gröblacher, and O. Painter, “Two-dimensional phononic-photon band gap optomechanical crystal cavity,” *Physical Review Letters*, vol. 112, no. 15, p. 153603, 2014.
- [81] H. Ren, M. H. Matheny, G. S. MacCabe, J. Luo, H. Pfeifer, M. Mirhosseini, and O. Painter, “Two-dimensional optomechanical crystal cavity with high quantum cooperativity,” *Nature communications*, vol. 11, no. 1, pp. 1–10, 2020.
- [82] G. Madiot, M. Albrechtsen, S. Stobbe, C. M. Sotomayor-Torres, and G. Arregui, “Multimode optomechanics with a two-dimensional optomechanical crystal,” *APL Photonics*, vol. 8, no. 11, 2023.

- [83] R. G. Povey, M.-H. Chou, G. Andersson, C. R. Conner, J. Grebel, Y. J. Joshi, J. M. Miller, H. Qiao, X. Wu, H. Yan, *et al.*, “Two-dimensional optomechanical crystal resonator in gallium arsenide,” *Physical Review Applied*, vol. 21, no. 1, p. 014015, 2024.
- [84] F. M. Mayor, S. Malik, A. G. Primo, S. Gyger, W. Jiang, T. P. Alegre, and A. H. Safavi-Naeini, “High photon-phonon pair generation rate in a two-dimensional optomechanical crystal,” *Nature Communications*, vol. 16, no. 1, p. 2576, 2025.
- [85] D. Zhu, M. Colangelo, C. Chen, B. A. Korzh, F. N. Wong, M. D. Shaw, and K. K. Berggren, “Resolving photon numbers using a superconducting nanowire with impedance-matching taper,” *Nano Letters*, vol. 20, no. 5, pp. 3858–3863, 2020.
- [86] A. H. Safavi-Naeini and O. Painter, “Proposal for an optomechanical traveling wave phonon-photon translator,” *New J. Phys.*, vol. 13, p. 013017, 2011.
- [87] N. Zen, T. A. Puurtinen, T. J. Isotalo, S. Chaudhuri, and I. J. Maasilta, “Engineering thermal conductance using a two-dimensional phononic crystal,” *Nature communications*, vol. 5, no. 1, p. 3435, 2014.
- [88] J. Maire, R. Anufriev, R. Yanagisawa, A. Ramiere, S. Volz, and M. Nomura, “Heat conduction tuning by wave nature of phonons,” *Science advances*, vol. 3, no. 8, p. e1700027, 2017.
- [89] M. R. Wagner, B. Graczykowski, J. S. Reparaz, A. El Sachat, M. Sledzinska, F. Alzina, and C. M. Sotomayor Torres, “Two-dimensional phononic crystals: Disorder matters,” *Nano letters*, vol. 16, no. 9, pp. 5661–5668, 2016.
- [90] M. Borselli, T. J. Johnson, and O. Painter, “Measuring the role of surface chemistry in silicon microphotonics,” *Applied Physics Letters*, vol. 88, no. 13, 2006.
- [91] M. Chen, J. C. Owens, H. Putterman, M. Schäfer, and O. Painter, “Phonon engineering of atomic-scale defects in superconducting quantum circuits,” *arXiv preprint arXiv:2310.03929*, 2023.
- [92] A. Y. Cleland, E. A. Wollack, and A. H. Safavi-Naeini, “Studying phonon coherence with a quantum sensor,” *arXiv preprint arXiv:2302.00221*, 2023.
- [93] M. Mirhosseini, A. Sipahigil, M. Kalaei, and O. Painter, “Superconducting qubit to optical photon transduction,” *Nature*, vol. 588, no. 7839, pp. 599–603, 2020.
- [94] T. van Thiel, M. Weaver, F. Berto, P. Duivesteyn, M. Lemang, K. Schuurman, M. Žemlička, F. Hijazi, A. Bernasconi, C. Ferrer, *et al.*, “Optical readout of a superconducting qubit using a piezo-optomechanical transducer,” *Nature Physics*, pp. 1–5, 2025.

- [95] G. Arnold, T. Werner, R. Sahu, L. N. Kapoor, L. Qiu, and J. M. Fink, “All-optical superconducting qubit readout,” *Nature Physics*, pp. 1–8, 2025.
- [96] M. Xu, X. Han, W. Fu, C.-L. Zou, and H. X. Tang, “Frequency-tunable high-q superconducting resonators via wireless control of nonlinear kinetic inductance,” *Applied Physics Letters*, vol. 114, no. 19, 2019.
- [97] J. H. Banker, *Photonic and phononic band gap engineering for circuit quantum electrodynamics and quantum transduction*. California Institute of Technology, 2022.
- [98] S. Wood, *Quantum Microwave to Optical Transduction With Light-Robust Superconducting Circuits*. California Institute of Technology, 2024.
- [99] P. Chiappina, J. Banker, S. Meesala, D. Lake, S. Wood, and O. Painter, “Design of an ultra-low mode volume piezo-optomechanical quantum transducer,” *Optics Express*, vol. 31, no. 14, pp. 22914–22927, 2023.
- [100] K. Airola, S. Mertin, J. Likonen, E. Hartikainen, K. Mizohata, J. Dekker, A. T. Sebastian, and T. Pensala, “High-fidelity patterning of aln and scaln thin films with wet chemical etching,” *Materialia*, vol. 22, p. 101403, 2022.

Appendix A

NANOFABRICATION

A.1 Nanofabrication tools

Nanofabrication processes described in this thesis are performed using following tools.

- **Electron beam lithography:** Raith EBPG 5200 (100 kV)
- **Optical lithography:** Karl Suss MA6 Mask Aligner
- **Spin coating:** Headway Research PWM 32
- **Reactive ion etching:** Oxford Instruments Plasma Technology Plasmalab System 100 ICP-RIE 380
- **Plasma cleaning:** PIE Scientific Targeo Plasma Cleaner
- **Vapor HF etching:** SPTS uEtch HF Vapor Etcher
- **Electron beam deposition:** AJA Orion ATC Series
- **Sputtering:** AJA Orion sputtering system
- **Scanning electron microscopy:** Thermo Fisher Nova 600 NanoLab

A.2 Hybrid 2D transducer fabrication

In this section, details on hybrid 2D transducer fabrication steps are presented. Processes described are performed on a 10mm by 10mm AlN over SOI die comprises of a 300 nm thick c-cut AlN layer, a 220nm Silicon device layer with resistivity $\rho \sim 3k\Omega.cm$, a 3 μm buried oxide layer and a 725 μm handle silicon layer.

Marker deposition

- **Sample pre-cleaning:** Chip cleaning is performed with 5 minutes acetone and isopropyl alcohol soak followed by a direct oxygen plasma cleaning with 20 sccm O_2 for 5 minutes.

- **Patterning:** ZEP-520A spun with 3000rpm for 1 min. Sample is post baked at 180C for 3 minutes. Electron beam lithography is performed using beam current of 1 nA and fracturing resolution of 3 nm with a base dose of $250 \mu C/cm^2$. Resist is developed in ZED N50 for 2 minutes 30 seconds followed by a 30 seconds MIBK rinse.
- **Cr/Au marker deposition:** 5 nm Cr adhesion layer is deposited using electron beam deposition with a rate of 0.5 \AA/s . 80 nm Au marker layer is deposited using electron beam deposition with a rate of 1 \AA/s .
- **Lift-off:** Lift-off is performed in 2 steps of 5 hours long N-methyl-2-pyrrolidone bath at 150 C. Sample soaked into acetone and isopropyl alcohol for 5 minutes followed by a direct oxygen plasma cleaning with 20 sccm O_2 for 5 minutes.

AlN piezo box

- **Sample pre-cleaning:** Chip cleaning is performed with 5 minutes acetone and isopropyl alcohol soak followed by a direct oxygen plasma cleaning with 20 sccm O_2 for 5 minutes.
- **Layer thinning:** Reactive ion etching process is performed using Ar/Cl_2 with 10 sccm Ar flow and 20 sccm Cl_2 flow. 300 W ICP power and 30 W RF power is used. Sample is etched for 1 minute.
- **Patterning:** ZEP-520A spun with 3000rpm for 1 min. Sample is post baked at 180C for 3 minutes. Electron beam lithography is performed using beam current of 1 nA and fracturing resolution of 3 nm with a base dose of $250 \mu C/cm^2$. Resist is developed in ZED N50 for 2 minutes 30 seconds followed by a 30 seconds MIBK rinse.
- **SiO₂ mask deposition:** 100 nm SiO_2 mask is deposited using electron beam deposition in 3 steps. In the first step a 200 \AA thick layer is deposited with a rate of 0.5 \AA/s . Second and third layers are deposited with a rate of 1 \AA/s for a thickness of 600 \AA and 200 \AA respectively.
- **Lift-off:** Lift-off is performed in 2 steps of 5 hours long N-methyl-2-pyrrolidone bath at 150 C. Sample soaked into acetone and isopropyl alcohol for 5 minutes followed by a direct oxygen plasma cleaning with 20 sccm O_2 for 5 minutes.
- **Dry etching:** Reactive ion etching process is performed using Ar/Cl_2 with 10 sccm Ar flow and 20 sccm Cl_2 flow. 300 W ICP power and 30 W RF

power is used. Sample is etched for 2 minutes (or the remaining AlN layer reaches less than 30 nm)

- **Wet etching:** Wet etching process is performed using Tetramethylammonium hydroxide at 25 C for 10 seconds followed by two DI water rinse. Sample is dipped into buffered hydrofluoric acid (10:1) for 2 minutes for mask removal followed by a two step DI water rinse.

Silicon protection

- **Sample pre-cleaning:** Chip cleaning is performed with 5 minutes acetone and isopropyl alcohol soak.
- **Patterning:** ZEP-520A spun with 3000rpm for 1 min. Sample is post baked at 180C for 3 minutes. Electron beam lithography is performed using beam current of 1 nA and fracturing resolution of 3 nm with a base dose of $250 \mu\text{C}/\text{cm}^2$. Resist is developed in ZED N50 for 2 minutes 30 seconds followed by a 30 seconds MIBK rinse.
- **Al₂O₃ protection deposition:** 100 nm Al₂O₃ protection layer is deposited using electron beam deposition in 3 steps. In the first step a 200 Å thick layer is deposited with a rate of 0.5 Å/s. Second and third layers are deposited with a rate of 1 Å/s for a thickness of 600 Å and 200 Å respectively.
- **Lift-off:** Lift-off is performed in 2 steps of 5 hours long N-methyl-2-pyrrolidone bath at 150 C. Sample soaked into acetone and isopropyl alcohol for 5 minutes followed by a direct oxygen plasma cleaning with 20 sccm O₂ for 5 minutes.
- **Sample post-cleaning:** Chip cleaning is performed in 5 hours long N-methyl-2-pyrrolidone bath at 150 C. Sample soaked into acetone and isopropyl alcohol for 5 minutes followed by a direct oxygen plasma cleaning with 20 sccm O₂ for 5 minutes.

NbN resonators and electrodes

- **Sample pre-cleaning:** Chip cleaning is performed with 5 minutes acetone and isopropyl alcohol soak. Sample is dipped into buffered hydrofluoric acid (10:1) for 15 seconds and rinsed with two steps of DI water soak.
- **NbN sputtering:** 25 nm NbN thin film is sputtered in *sputtering tool* with N₂ flow of 5 sccm and RF bias of 50 W.

- **Patterning:** ZEP-520A spun with 8000rpm for 1 min. Sample is post baked at 180C for 3 minutes. Electron beam lithography is performed using beam current of 1 nA and fracturing resolution of 3 nm with a base dose of $250 \mu C/cm^2$. Resist is developed in ZED N50 for 2 minutes 30 seconds followed by a 30 seconds MIBK rinse.
- **Etching:** Reactive ion etching process is performed using SF_6/Ar with 20 sccm SF_6 flow and 10 sccm Ar flow. 300 W ICP power and 30 W RF power is used. Samples are etched for 2 minutes.
- **Sample post-cleaning:** Chip cleaning is performed in 5 hours long N-methyl-2-pyrrolidone bath at 150 C. Sample soaked into acetone and isopropyl alcohol for 5 minutes followed by a direct oxygen plasma cleaning with 20 sccm O_2 for 5 minutes.

Silicon layer

- **Sample pre-cleaning:** Chip cleaning is performed with 5 minutes acetone and isopropyl alcohol soak. Sample is dipped into buffered hydrofluoric acid (10:1) for 1 minute and rinsed with two steps of DI water soak.
- **Patterning:** ZEP-520A spun with 8000rpm for 1 min. Sample is post baked at 180C for 3 minutes. Electron beam lithography is performed using beam current of 150 pA and fracturing resolution of 3 nm with a base dose of $220 \mu C/cm^2$. Resist is developed in ZED N50 for 2 minutes 30 seconds followed by a 30 seconds MIBK rinse.
- **Etching:** Reactive ion etching process is performed using C_4F_8/SF_6 chemistry with 72 sccm C_4F_8 flow and 30 sccm SF_6 flow. 600 W ICP power and 18 W RF power is used while the chamber pressure is held at 10mTorr. Samples are etched for 4 minutes 5 seconds.
- **Sample post-cleaning:** Chip cleaning is performed in 5 hours long N-methyl-2-pyrrolidone bath at 150 C. Sample soaked into acetone and isopropyl alcohol for 5 minutes followed by a direct oxygen plasma cleaning with 20 sccm O_2 for 5 minutes.

Deep etching

- **Sample pre-cleaning:** Chip cleaning is performed with 5 minutes acetone and isopropyl alcohol soak.
- **Patterning:** SPR-220-7 spun with 3000rpm for 1 min, edge beam is removed using Trichloroethylene. Sample is post baked at 90C for 1 minute and post bake is performed at 115C for 5 minutes. Optical lithography is performed using 365 nm UV light i-line exposure for 1 min with 280 W power. Sample rested for 2 hours before development. Following a pre-bake at 115C for 5 minutes, resist is developed in MF CD26 for 2 minutes 30 seconds followed by a 30 seconds DI water rinse.
- **Etching:** Reactive ion etching process is performed in three steps to etch silicon device layer, buried oxide layer and finally the handle silicon layer. Details of the etch parameters are given in Table A.1.

Table A.1: Etch steps used in deep etching

Parameter	Device layer Si	Buried oxide	Handle Si
C ₄ F ₈ flow (sccm)	50	70	0
SF ₆ flow (sccm)	21	0	160
O ₂ flow (sccm)	0	5	0
RF power (W)	15.5	150	0
ICP power (W)	600	2200	2500
DC bias (V)	60	205	20
Chamber pressure (mTorr)	10	8	90
Table temperature (°C)	15	15	15

- **Sample post-cleaning:** Chip cleaning is performed in 10 hours long N-methyl-2-pyrrolidone bath at 150 C. Sample soaked into acetone and isopropyl alcohol for 5 minutes followed by a direct oxygen plasma cleaning with 20 sccm O₂ for 10 minutes.
- **Release:** Silicon features and resonator membranes are released by isotropic etching of the buried oxide layer with hydrofluoric acid vapor.

A.3 1D and 2D OMC fabrication

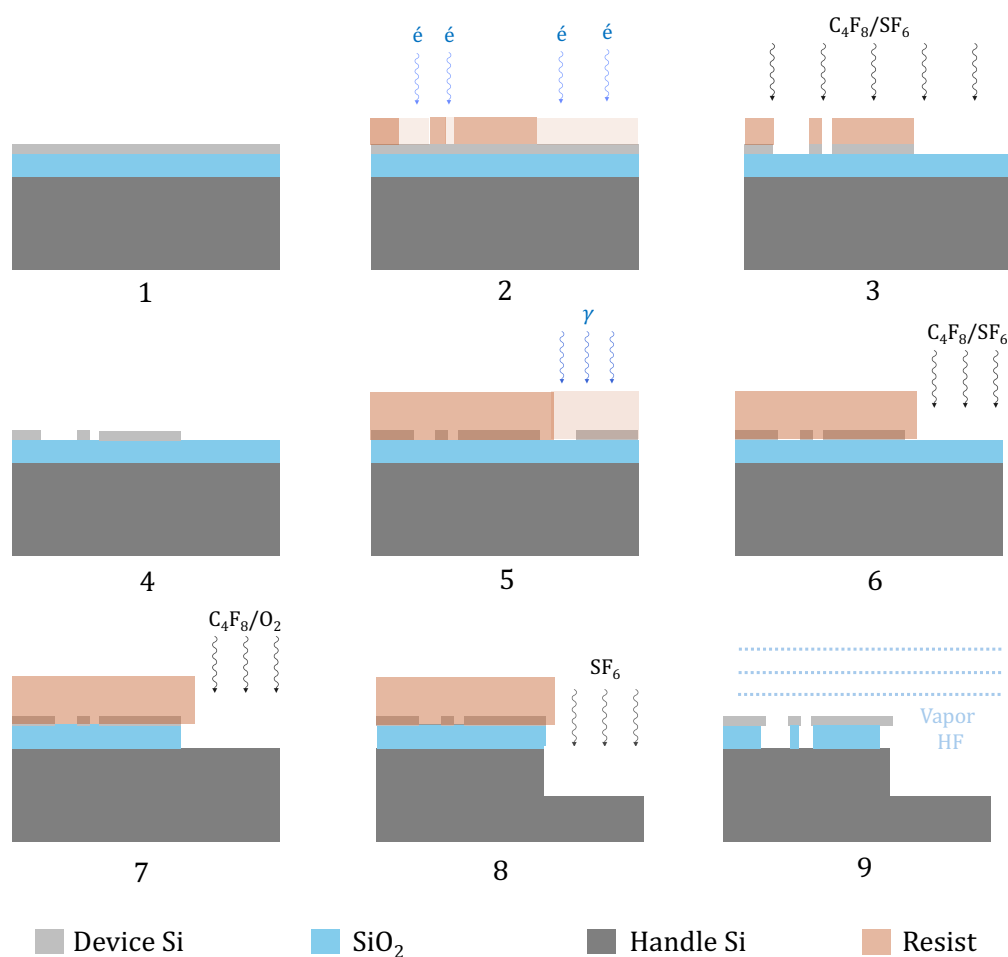


Figure A.1: **Standard nanofabrication flow of 1D and 2D OMCs**

1D and 2D pure optomechanical crystals are fabricated following the last two fabrication steps (silicon layer and deep etching) presented in the Appendix A2. Process is performed on a 10mm by 10mm SOI die comprises of a 220nm Silicon device layer with resistivity $\rho \sim 3k\Omega.cm$, a 3 μm buried oxide layer and a 725 μm handle silicon layer.

Appendix B

MEASUREMENT TECHNIQUES FOR HYBRID OMCS

B.1 Mode occupancy calibration

The cavity photon occupation n_c is calibrated using the input power at the device P_{in} with the following relation:

$$n_c = \frac{P_{\text{in}}}{\hbar\omega_1} \frac{\kappa_e}{\Delta^2 + \kappa_t^2/4}, \quad (\text{B.1})$$

where ω_1 is the pump frequency, κ_e is the coupling rate between optical cavity and the optical coupling waveguide, $\kappa_t = \kappa_i + \kappa_e$ is the measured total linewidth of the optical cavity, and $\Delta = \omega_c - \omega_1$ is the detuning of the laser from the cavity frequency ω_c . To calibrate the acoustic mode phonon occupancy to the measured photon count rate on the single photon detector, we perform sideband asymmetry measurements [79]. The measured count rate for red and blue detuned pump laser are given by

$$\Gamma(\Delta = \pm\Omega_m) = \Gamma_{\text{dark}} + \Gamma_{\text{pump}} + \Gamma_{\text{SB},0} \left(n_{\text{th}} + \frac{1}{2}(1 \pm 1) \right), \quad (\text{B.2})$$

where n_{th} is the occupation of the acoustic resonator. Γ_{dark} is the dark count rate of the SPD, Γ_{pump} is the pump bleedthrough, and $\Gamma_{\text{SB},0}$ is the detected photon scattering rate per phonon. $\Gamma_{\text{SB},0}$ relates to the optomechanical scattering rate $\gamma_{\text{OM}} = 4g_{\text{OM}}^2 n_c / \kappa_t$ through the external detection efficiency, $\Gamma_{\text{SB},0} = \eta_{\text{ext}} \gamma_{\text{OM}}$. We use pulsed laser with repetition rate much smaller than the intrinsic decay rate ($R \ll \gamma_0$) such that the $n_{\text{th}} \ll 1$ at the beginning of each pulse. $\Gamma_{\text{SB},0}$ can then be extracted by taking the difference between the count rate at the beginning of the pulse. For pulsed transduction measurements with short optical pulses shown in Figure 5.8 of the main text, the count rates for the red- and blue-detuned pump laser are averaged over the duration of the optical pulse. This averaging accounts for any finite rise time in the sideband scattering rates.

The hot bath measurements in the main text are performed with laser on cavity resonance $\Delta = 0$. The count rate $\Gamma(\Delta = 0)$ relates to $\Gamma_{\text{SB},0}$ through the sideband resolution factor $(2\Omega_m/\kappa_t)^2$

$$\Gamma(\Delta = 0) = \Gamma_{\text{dark}} + \Gamma_{\text{pump}} + \left(\frac{\kappa_t}{2\Omega_m} \right)^2 \Gamma_{\text{SB},0} n_m, \quad (\text{B.3})$$

where n_m is the measured thermal occupation in the absence of the optomechanical backaction as defined by Equation 5.1 of the main text.

B.2 Filter correction

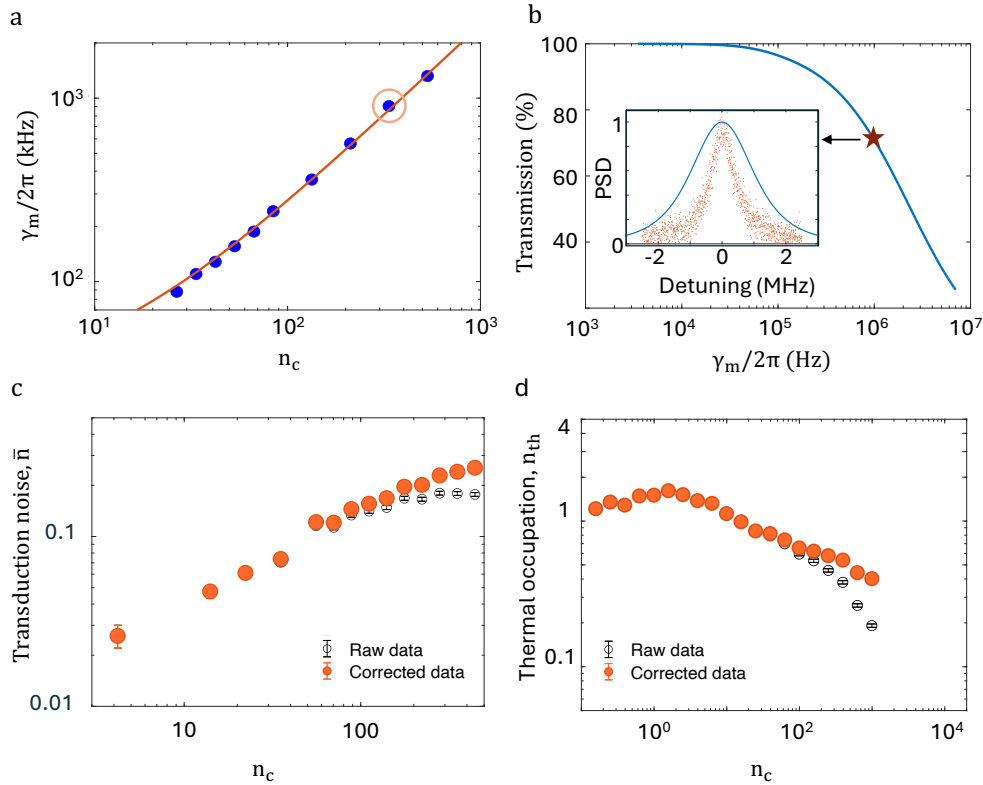


Figure B.1: **Sideband filter chain transmission.** **a)** total acoustic linewidth as a function of n_c measured using Electromagnetically induced transparency method (EIT) [3]. **b)** transmission through the filter chain as a function of the acoustic linewidth. The inset shows the normalized power spectral density of the filter chain (blue) and that for acoustic sideband (red) for data point marked with circle in panel **a** ($n_c = 335$). **c)** phonon occupancy in pulsed mode for device II. The raw data is shown in magenta whereas the corrected data is shown in blue. **d)** phonon occupancy in continuous wave mode for device II. The black circles show the raw measured data whereas the orange circles show the corrected data.

The sideband filter chain is parked at the acoustic sideband of the pump to detect the optomechanically scattered photons, while filtering out the pump. However, at large pump powers, the bandwidth of the optomechanical sideband γ_m approaches

that of the filter (=3.6 MHz). This overlap leads to a reduced measured count rate, resulting in an inaccurate estimation of phonon occupancy. Figure B.1a shows the acoustic linewidth γ_m as a function of n_c . Measurements are performed using Electromagnetically Induced Transparency (EIT) technique where a pump laser is placed on red sideband and a weak probe scans across a few Megahertz bandwidth across the acoustic sideband at the cavity resonance. γ_m is the sum of the optomechanical backaction γ_{OM} , intrinsic linewidth γ_i , coupling rate to the hot bath γ_p , and the pure dephasing rate γ_ϕ . For two bandpass filters in series, the transmission T of a acoustic sideband with lorentzian profile is given by

$$T = \int_{-\infty}^{\infty} H_1(f)H_2(f)\frac{\gamma_m(f)}{2\pi}df \quad (\text{B.4})$$

where $H_{1,2} = (1 + (\frac{f}{\text{FWHM}_{1,2}/2})^2)^{-1}$ is the normalized spectral response of each filter with $\text{FWHM}_{1,2} = 3.6$ MHz. The corrected phonon occupancy n_{th} can then be calculated using measured phonon occupancy n_{th}^* using the relation

$$n_{\text{th}} = n_{\text{th}}^* \times \frac{1}{T} \int_{-\infty}^{\infty} \frac{\gamma_m}{2\pi} df \quad (\text{B.5})$$

Figure B.1b shows the transmission factor T as a function of $\gamma_m/2\pi$. The inset shows the normalized power spectral density of the combined filter chain response (blue), and the acoustic response for $n_c = 335$. Figure B.1c shows the phonon occupancy before (black) and after (orange) correction in pulsed laser mode for device II. Figure B.1d shows the same in continuous wave mode for device II. In the case of γ_p and n_p measurements where the pump is placed at the optical cavity resonance, the linewidth of acoustic sideband is much smaller than the filter linewidth ($\gamma_p + \gamma_0 \ll 2\pi * 3.6$ MHz) for n_c range measured in this study, so a correction factor is not required.